ϕ Meson Production in pp Reactions at 3.5 GeV with HADES Detector

Marek Pałka

Thesis Supervisor

Prof. UJ dr hab. Piotr Salabura

Faculty of Physics, Astronomy and Applied Computer Science

of the Jagiellonian University

Cracow, 2011

Contents

Abstract

The High Acceptance Di-Electron Spectrometer (HADES) working at GSI Darmstadt is an unique apparatus aiming for systematical investigations of dilepton and strangeness production in elementary and heavy ion collisions in 1-4 $AGeV$ energy range. Measurements performed with this spectrometer in heavy ion and proton-nucleus collisions aim in investigation of hadron properties in nuclear matter. In wide scope of the HADES physics program the investigations of hadron production in elementary collisions are also foreseen. In the framework of this dissertation the exclusive ϕ meson production in proton-proton reactions at 3.5 GeV kinetic energy is presented. The ratio ϕ to ω production cross section has been obtained and discussed in connection to the OZI rule violation phenomena.

Description of the analysis methods, which leads to estimation of the $pp \rightarrow pp\phi$ meson production cross sections is presented. This is followed by a comparison of the extracted ϕ meson production characteristics with the simulation of this reaction channel. In the simulation an isotropic ϕ angular distribution in the Center of Mass (CM) frame of colliding nucleons and an uniform phase space population in the proton-meson Dalitz distribution are assumed. A good agreement of the measured angular, momentum and proton-ϕ invariant mass distributions with the simulation have been achieved.

The extracted exclusive ϕ production cross section at 3.5 GeV kinetic energy equals:

$$\sigma_{\phi}^{4\pi} = 1.05[\mu b] \pm 0.2[\mu b](stat.) \pm 0.13[\mu b](syst.)$$

The exclusive ω production cross section obtained in this experiment allows to calculate the ratio of ϕ to ω production cross section which equals:

$$R_{\phi/\omega} = 0.0099 \pm 0.0018(stat.) \pm 0.0012(syst.)$$

The obtained ratio is close to the one measured in pion-nucleon reaction which exceeds by factor $\sim$ 2-3 OZI rule predictions.

In the second part, selected tasks of the HADES data acquisition (DAQ) system upgrade, which were in responsibility of the author of this thesis, are described. They concerned mainly following aspects:

- developing, testing and validating of the central trigger system (CTS),
- developing, testing and validating of the readout electronics for RPC, START, VETO, Forward Wall and TOF detectors.

The newly developed HADES DAQ system, as it is presently used in ongoing Au+Au campaign, with its trigger distribution scheme, front-end boards and readout components are described as well.

Part I

Chapter 1

Introduction and Physics Motivations

1.1 Quark Model

The first elementary particle found in experiment was electron, discovered by J.J.Thompson in 1897. 50 years later, in extended cosmic rays measurements physicists discovered several new particle species. It was also soon noticed that one can group them into families using specific symmetries. In 1964 Gell-Mann and Zweig proposed that all hadrons, particles interacting with strong forces, are built out of the elementary objects with a spin value of $\frac{1}{2}$ (fermions), called quarks (only quarks u, d, s were proposed at this time). It was proposed that quarks have electric and color charges, which are responsible for the electromagnetic and strong interactions, respectively. Later, the c, b, t heavy quarks were discovered and a quark family has been completed. Table 1.1 summarizes the quark basic properties: masses, electromagnetic charges and quantum numbers.

One of the main assumptions of this hypothesis is that only composite objects without any specific color (color singlets) can be experimentally observed. This puts constraints on how the hadrons can be built. If each quark/anti-quark can have three colors/anti-colors(red, green, blue/or corresponding anti-colors) then the hadrons are built either out of the three quarks (baryons) or quark and anti-quark combinations (mesons). The theory which describes strong color interactions is called Quantum Chromo Dynamics (QCD).

These interactions are mediated by exchange of massless field bosons called gluons. Each gluon carries the color/anti-color charge. This makes possible, in contrast to the situation in electrodynamics, direct interactions between the gluons.

1.2 Chiral Symmetry

The Lagrangian, which describes the dynamics of a free fermion, has the following form:

$$L = \bar{\psi}(i\gamma_\mu \delta^\mu - m)\psi$$

According to the Noether theorem, if a given Lagrangian is invariant under certain global transformations of the fields ψ, then the corresponding charges and currents are conserved. For example, for the above Lagrangian one can consider two global transformations:

- vector $SU(2)_V$ transformation: $\Lambda_V : \psi \rightarrow \psi e^{-i\frac{\vec{\tau}}{2}\vec{\theta}}$
  where: $\vec{\tau}$ - Pauli matrices,
- axial $SU(2)_A$ transformation: $\Lambda_A : \psi \rightarrow \psi e^{-i\gamma_5\frac{\vec{\tau}}{2}\vec{\theta}}$
  where: $\gamma_5 = i\gamma^0\gamma^1\gamma^2\gamma^3, \gamma$ - Dirac matrices.

It can be shown that the first part of the Lagrangian ($m_q = 0$) is invariant under the axial and the vector transformations. The second part is also invariant under the vector transformation but not under the axial (for the non-zero mass fermions). The vector

Table 1.1: Quark masses and their quantum numbers.

Flavor	Mass $[MeV/c^2]$	I	I_3	S	C	B	T	$\frac{Q}{e}$
u	1.7 to 3.3	$\frac{1}{2}$	$\frac{1}{2}$	0	0	0	0	$+\frac{2}{3}$
d	4.1 to 5.8	$\frac{1}{2}$	$-\frac{1}{2}$	0	0	0	0	$-\frac{1}{3}$
s	~ 101	0	0	-1	0	0	0	$+\frac{2}{3}$
c	~ 1270	0	0	0	1	0	0	$-\frac{1}{3}$
b	~ 4190	0	0	0	0	-1	0	$+\frac{2}{3}$
t	~ 172000	0	0	0	0	0	1	$-\frac{1}{3}$

transformation corresponds to a rotation in the isospin space [1]. The invariance under this transformation manifests itself in the mass degeneracy of hadron states with the same isospin (e.g. pions). The axial transformation rotates hadron fields ψ into states of the opposite parity but same mass. The invariance of the Lagrangian under both transformations $SU(2)_V \times SU(2)_A$ is called chiral symmetry. The fact that it is not observed in nature means that the symmetry is broken. For example the ρ meson with $(J^{PC}) = 1^{--}$ has mass $m_\rho = 0.77\ GeV/c^2$, which is significantly lower than the mass of the a_1 meson with $J^{PC} = 1^{++}$ ($m_{a1} = 1.23\ GeV/c^2$)).

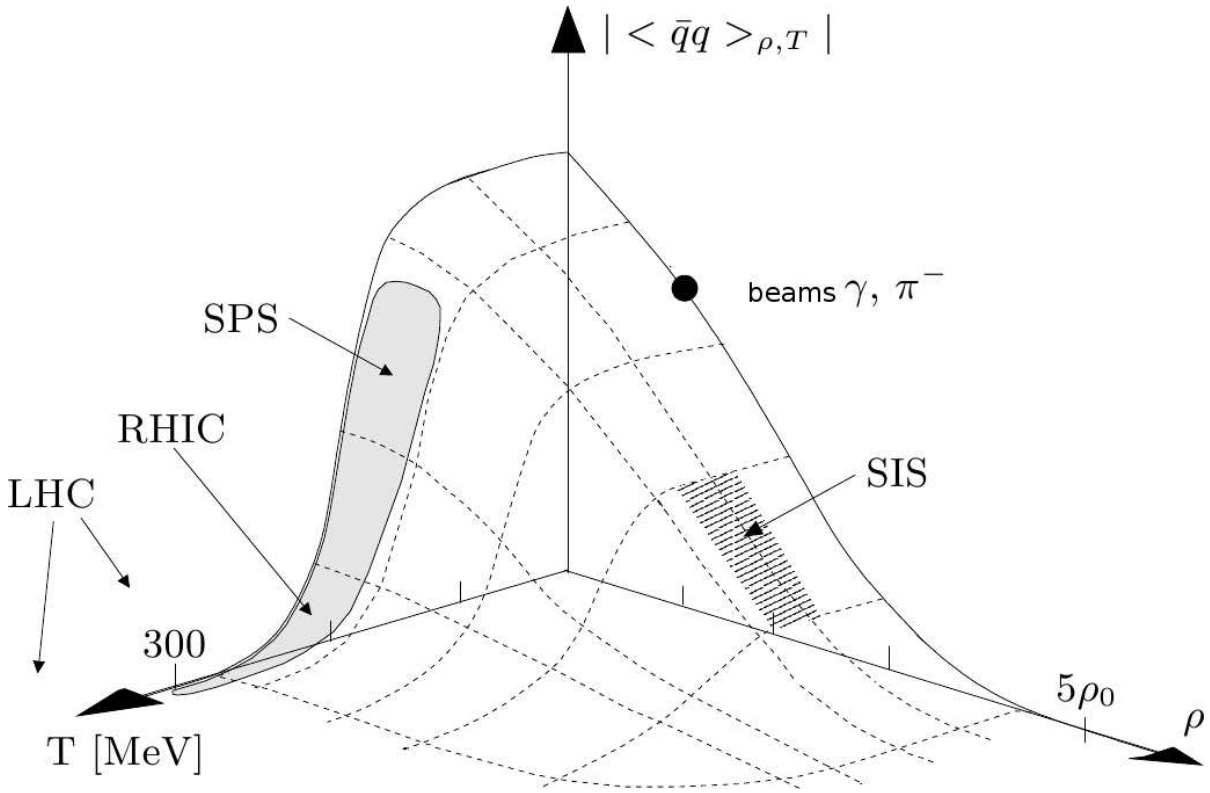

Figure 1.1: Value of two quark condensate as a function of the density and temperature, based on the NJL model [4].

The masses of the quarks are generated in the Standard Model in two ways. One, like for the leptons, via coupling to the Higgs field in the electroweak interactions. This explicitly breaks the chiral symmetry of the Lagrangian and is responsible for the mass generation of heavy quarks c, b, t. The other mechanism, essential for the masses of light quarks u, d, s, is induced by a spontaneous chiral symmetry breaking. This mechanism is

signalized by the appearance of two, four quark and gluon condensates (for a recent review see [2]). The quark condensates are non-vanishing structures of the quark-anti quark pairs created in the vacuum by non-perturbative QCD effects. The dynamical interaction between these condensates and the quarks causes that the quarks acquire large effective mass. On the other hand early predictions based on the Nambu-Jona-Lasino model[3] indicated that at higher nuclear densities and/or temperatures the expectation value of two quark condensate decreases (see Fig. 1.1, [4]). Furthermore, it has also been proposed that under such conditions lowering of the masses of light vector mesons ρ, ω and ϕ can be used as a signal for the chiral symmetry restoration in dense nuclear matter. However, more complex calculations based on QCD sum rules indicate that the connection between the meson masses and the quark condensates is much more evolved and is related to the integral of the meson spectral function. Therefore, the QCD sum rules provide constraints on both the WIDTH and MASS of the meson at a given density, but do not answer the question about in-medium masses in the unique way [2].

Independently from theoretical considerations, from the experimental point of view the fundamental question "how does the hadron masses change in dense and hot medium?" remains open. To address this there are in principle two experimental methods followed in the world :

a) Measurements of the meson mass distribution (spectral function) inside nuclear matter. As demonstrated by the NA60 collaboration this method is suitable for the short lived ρ meson [5],

b) Measurements of the so-called "transparency ratio" of nuclear matter for a given meson. This method has been used to study properties of the ω and ϕ mesons in cold nuclear matter (nucleus). It allows to derive conclusions on the meson broadening (width increase) inside the nuclear matter [6] [7] [8].

For the latter one, measurements of the ϕ and ω production in $p-p$ reactions , which is the subject of this thesis, is an important reference. Though, the masses of both mesons are similar, their internal quark structures differ from each other (see next section for more details), hence can help to disentangle effects related to u, d and s quarks. Indeed,

the measured meson transparency indicate large absorption inside nuclear matter, which is equivalent to at least 10-fold increase of the meson natural width.

Recently, the HADES collaboration also measured a ϕ to ω cross section ratio in $Ar + KCl$ collisions at 1.756 $AGeV$ [9]. It is an order of magnitude larger as compared to the one measured in pp collisions close to the production threshold but it is in agreement with thermal model predictions (see Fig. 1.2). The result might indicate larger absorption of the ω as compared to the ϕ meson. On the other hand one should note that in this case the ϕ meson is created at sub-threshold energy ($\epsilon < 0$). Thus, observed enhancement of the ϕ production may indicate importance of multi-step processes with intermediate short-lived resonances involved [10] or/and meson final-state effects in the dense nuclear matter [2]. To complete the picture, further measurements have been performed with $p + Nb$ system at $3.5 AGeV$ with the HADES spectrometer and data analysis is in progress.

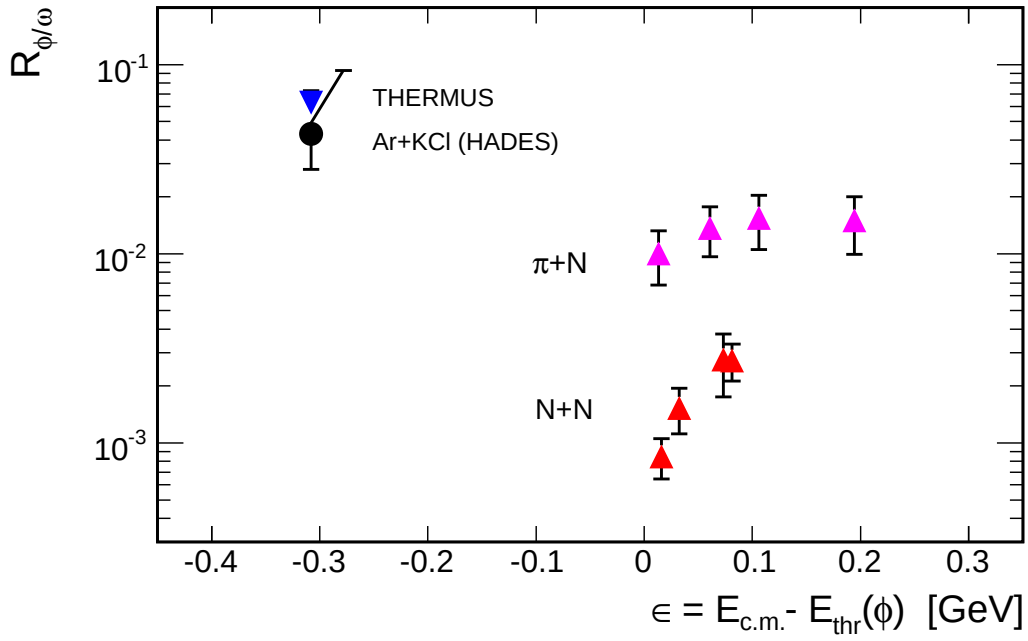

Figure 1.2: Comparison of the ϕ to ω ratio as a function of the excess energy ϵ. The result obtained with the HADES spectrometer in the $Ar + KCl$ collisions at 1.756 $AGeV$ is placed among other experimental results - the $NN \to NN\phi$ and the $\pi N \to N\phi$ reactions. Also thermal model (THERMUS [11]) in relation to the HADES result is presented.

The High Acceptance Di-Electron Spectrometer (HADES) working at SIS energies

(see fig. 1.1) aims for systematical investigations of properties of the light vector mesons in elementary and heavy ion collisions along both lines. The e^+ e^- decay channel was chosen as the best option to directly study properties of the light vector mesons. This is because the leptons don't interact strongly and can reveal the behavior of the mesons inside the dense nuclear matter. But also the meson reconstruction via hadronic decays, as shown in this thesis, is possible.

1.3 Light Vector Mesons ϕ and ω

The light vector mesons ρ, ω, ϕ are formed from the quark triplet u, d, s ($SU(3)$ flavor multiplet). The meson ground states composed by these quarks are listed in Table 1.2 giving their basic properties.

Table 1.2: Mesons ground states with the different total angular momentum, strangeness and isospin content [12].

quark combination	I	I_3	S	J^P 0^-	Mass $[MeV/c^2]$	J^P 1^-	Mass $[MeV/c^2]$
$\|u\bar{d}>$	1	1	0	π^+	139	ρ^+	775
$\|d\bar{u}>$	1	-1	0	π^-	139	ρ^-	775
$(\|d\bar{d}> - \|u\bar{u}>)\frac{1}{\sqrt{2}}$	1	0	0	π^0	135	ρ^0	775
$\|u\bar{s}>$	$\frac{1}{2}$	$\frac{1}{2}$	1	K^+	494	K^{*+}	892
$\|d\bar{s}>$	$\frac{1}{2}$	$-\frac{1}{2}$	1	K^0	497	K^{*0}	892
$\|\bar{u}s>$	$\frac{1}{2}$	$-\frac{1}{2}$	-1	K^-	494	K^{*-}	892
$\|\bar{d}s>$	$\frac{1}{2}$	$\frac{1}{2}$	-1	$\bar{K}^0$	497	$\bar{K}^{*0}$	892
$(\|u\bar{u}> + \|d\bar{d}> - 2\|s\bar{s})\frac{1}{\sqrt{6}}$	0	0	0	η_8		ϕ_8	
$(\|u\bar{u}> + \|d\bar{d}> + \|s\bar{s})\frac{1}{\sqrt{3}}$	0	0	0	η_0		ϕ_0	

The vector mesons ϕ and ω are linear combinations of the singlet ϕ_0 and octet ϕ_8 states of the SU(3) flavour symmetry nonet. The ϕ_0 and ϕ_8 states have the same isospin and the hyper charge ($Y = B + S$) quantum numbers, therefore they can mix and form the observed ω and ϕ mesons:

$$\phi = \phi_0 sin\theta_v - \phi_8 cos\theta_v \text{ and } \omega = \phi_8 sin\theta_v + \phi_0 cos\theta_v$$

From the following equations one can obtain meson masses:

$$\begin{aligned} M_\phi^2 &= M_0^2 sin^2\theta_v + M_8^2 cos^2\theta_v - 2M_{08} sin\theta\ cos\theta, \\ M_\omega^2 &= M_8^2 sin^2\theta_v + M_0^2 cos^2\theta_v + 2M_{08} sin\theta\ cos\theta, \\ M_{\phi\omega}^2 &= 0 = (M_0^2 - M_8^2) sin\theta\ cos\theta + M_{08}(sin^2\theta - cos^2\theta) \end{aligned}$$

the θ_v, which is a mixing angle, can be obtained:

$$tg^2\theta = \frac{M_\phi^2 - M_8^2}{M_8^2 - M_\omega^2}.$$

Next using a Gell-Maan-Okubo empirical mass formula [13] [14] one can calculate that $\theta_v = 39^o$. It is also possible to calculate this value from the meson radiative decay widths [15] [16] and one obtains $\theta_v = 37^o$.

On the other hand an "ideal" mixing angle:

$$sin\theta_v^{id} = \frac{1}{\sqrt{3}} \rightarrow \theta_v^{id} = 35.3^o$$

makes the ϕ and ω ideal mixing states:

$$\phi = |s\bar{s}> \qquad \omega = \frac{1}{\sqrt{2}}(|u\bar{u}> + |d\bar{d}>).$$

For this ideal mixing angle the ϕ meson is built only out of the strange quarks and the ω meson only from the u and d quarks. However, if the mixing angle would be the ideal one ϕ decay into 3 pions should be strongly suppressed because respective quark diagram for the decay displays disconnected quark lines . This is in fact the principle for the so called OZI rules discussed in section 1.4 (see Fig. 2.2 there). On the other hand, assuming a small deviation of θ_v from the ideal, one is able to explain the following branching ratio for the ϕ and the ω mesons [12].

$$
\begin{aligned}
\phi &\rightarrow K^+K^- 49\% \\
&\rightarrow K^0\bar{K}^0\ 34\% \\
&\rightarrow \pi^+\pi^-\pi^0\ 15\% \\
\omega &\rightarrow \pi^+\pi^-\pi^0\ 90\% \\
&\rightarrow \pi^+\pi^-\ 1.7\% \\
&\rightarrow \pi^0\gamma\ 8.9\%
\end{aligned}
$$

1.4 OZI Rule and its Violation - Experimental Data

As it has already been mentioned, the branching ratio for the $\phi \rightarrow \pi^+\pi^-\pi^0$ is suppressed and the $\phi \rightarrow K^+K^-$ channel is enhanced. Suppression of the three pion with respect to the kaon decay channel is explained by a rule formulated by Okubo-Zweig-Iizuka (OZI [17]). This rule says that a process, in which there are disconnected quark lines (fig.1.3a), is less probable to occur than the process with connected quark lines (fig.1.3b).

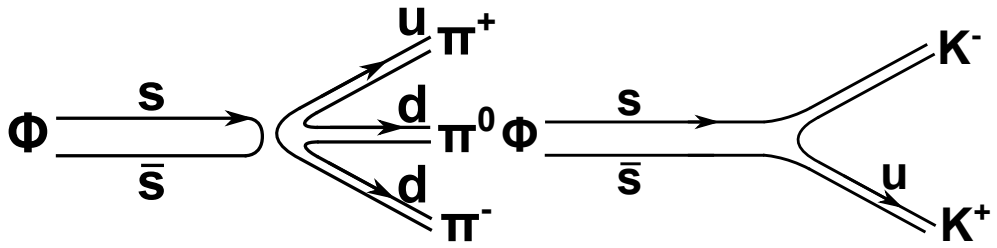

(a) ϕ decay into the three pions - disconnected quark lines.

(b) ϕ decay into two kaons.

Figure 1.3: OZI rule examples.

The OZI rule also allows to make predictions for the production of the ϕ vector meson in proton or pion induced reactions.

The production of ϕ meson, composed out of the pure $s\bar{s}$ state, in pp reactions is schematically presented in Fig. 1.4. The ϕ meson has parity and spin $J^{PC} = 1^{--}$ and that is why an odd number of gluons is needed in the production graph. At least three gluons

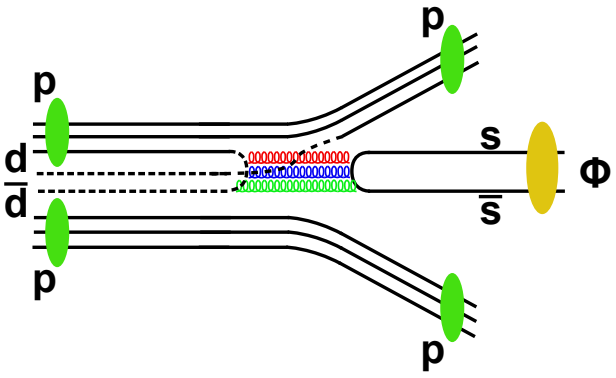

Figure 1.4: ϕ production in pp reactions.

are required to produce a color singlet state. Such process would be strongly suppressed and can proceed only due to a small admixture of the u, d quarks in the ϕ meson wave function.

The cross section of the ϕ meson production is generally normalized to the ω production cross section. The ratio of this cross sections equals[18]:

$$R_{\phi/\omega} = \frac{A + B \to \phi X}{A + B \to \omega X} = tan^2(\delta\theta_v) f = 4.21 \cdot 10^{-3} \cdot f, \tag{1.1}$$

where f is a ratio of the available phase space for the ω and ϕ production, in a given reaction, and $\delta\theta_v$ is a deviation from the ideal mixing angle.

The validity of this rule was studied since the 70'ties in various experiments:

- π proton induced reactions [19], [20], [21], [22], [23], [24], [25], [26], [27],
- high energy proton - proton reactions (for the momentum of the beam particles above 10 GeV/c) [24], [28], [29], [30]
- proton - anti-proton annihilation [31], [32], [33]

Results from these measurements are summarized in [34] and almost all of them show indications of the OZI rule violation, being largest in proton-antiproton annihilation at rest. In Fig.1.5 an example of such measurements from the OBELIX experiment is shown.

As it can be seen, the OZI rule is strongly violated. It is mostly evident for the reactions where in addition to the ϕ and ω light particles (γ,π) are produced. The violation of the

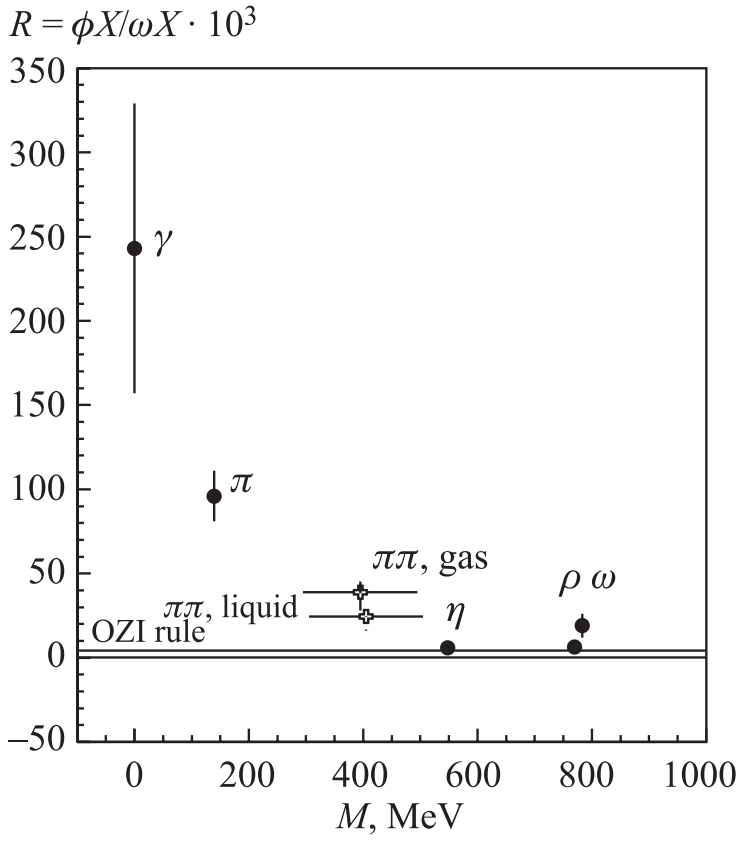

Figure 1.5: OZI rule violation as a function of the X particle mass. Presented by the OBELIX experiment [35]. Data obtained in $p\bar{p}$ annihilation at rest.

OZI rule depends also on the four momentum transfer (the smaller momentum transfer the larger the effect). This phenomenon was explained by several scenarios:

- the proton has a polarized $s\bar{s}$ contribution in its wave function [36],
- two step kaon exchange contribute to the ϕ meson production process [37] [38],
- ϕ resonance production vi cryptoexotic baryon $B_\phi uddss\bar{s}$ [39] [40].

To confirm one of the scenarios it was suggested to perform measurements in kinematic conditions as close as possible to the proton-antiproton annihilation at rest. For the proton - proton induced reactions the ϕ to ω ratio was available only for the higher energies. However, during last 10 years the DISTO and ANKE experiments measured ϕ and ω cross sections close to the production threshold of the ϕ meson. This allowed to estimate the energy range where the OZI rule violation is largest (see fig. 1.6).

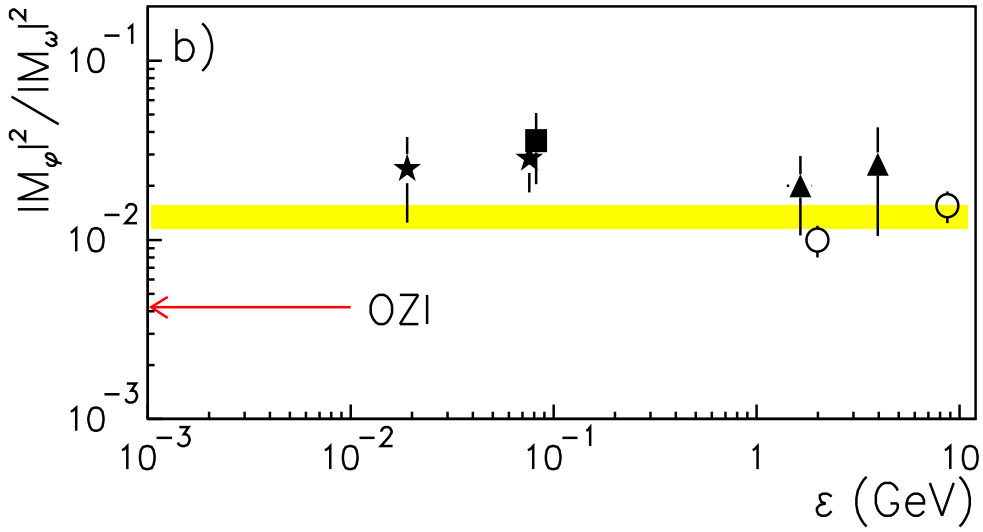

Figure 1.6: Ratio of matrix elements for the ϕ to ω production is shown as a function of the excess energy. The value predicted by the OZI rule is marked with red arrow and yellow band with FSI corrections [41]. Star points are the data from the ANKE collaboration [42], the squares from the DISTO [43], while the triangles and circles ($> 10\ GeV$) are extracted from ref. [44], [45], [46], [47].

In Fig.1.6 a compilation of proton-proton data is shown together with the predictions from model, in which the final state proton-proton interactions (FSI) are taken into account [48](yellow) and OZI rule (red arrow). As one can see, extracted ratio of matrix elements is in conflict with the OZI rules and largest deviation is observed at energies close to the production threshold. The model of A.Sibirtsev [41] is found to be in good agreement with the experimental data points at high energies (fig.1.6 yellow bar), but still it can not explain the data at energies close to the ϕ production threshold. The example of this model illustrates the importance of the intermediate energy to clarify the beam energy dependence of the ϕ production in pp reactions.

The results from the HADES pp experiment at 3.5 GeV kinetic energy ($\epsilon = 280\ MeV$) will allow to fill the gap between the data points in high energy region ($> 10\ GeV$) and energy just above the ϕ meson production threshold.

Chapter 2

Accelerator Area and HADES Spectrometer

2.1 Accelerator Area

Before going into detailed description of the High Acceptance Di-Electron Spectrometer (HADES) experiment setup, the accelerator area where the spectrometer is located is presented in this section. The accelerator complex (fig. 2.1,[49]), which provides beams for the HADES experiment, is located at the GSI Helmholtzzentrum für Schwerionenforschung GmbH facility in Darmstadt, Germany.

It can be logically divided into several different areas. The aim of the first part (UNILAC - UNIversal Linear Accelerator) is to extract ions and inject them into the synchrotron. This is realized in several steps. First, the ions are extracted out of a MEVVA or MUCIS ion source. In the next a Low Energy Beam Transport system (LEBT) together with a mass spectrometer for selecting appropriate isotopes is used and the beam is transported to a High Current Injector (*ger. Hochstrominjektor* - HSI). After this the energy of ions is $1.4\,MeV/u$ at maximum. In front of the next stage the beam is stripped and a particular ion charge state is selected. Then, the Alvarez linear accelerator[50] increases the energy of the ions to $11.4\,MeV/u$. In the next step the heavy ion synchrotron (*ger. SchwerIonen-Synchrotron* - SIS 18) is used to increase the momenta of ions to the required high energy. The whole facility can provide beams of protons up to uranium and

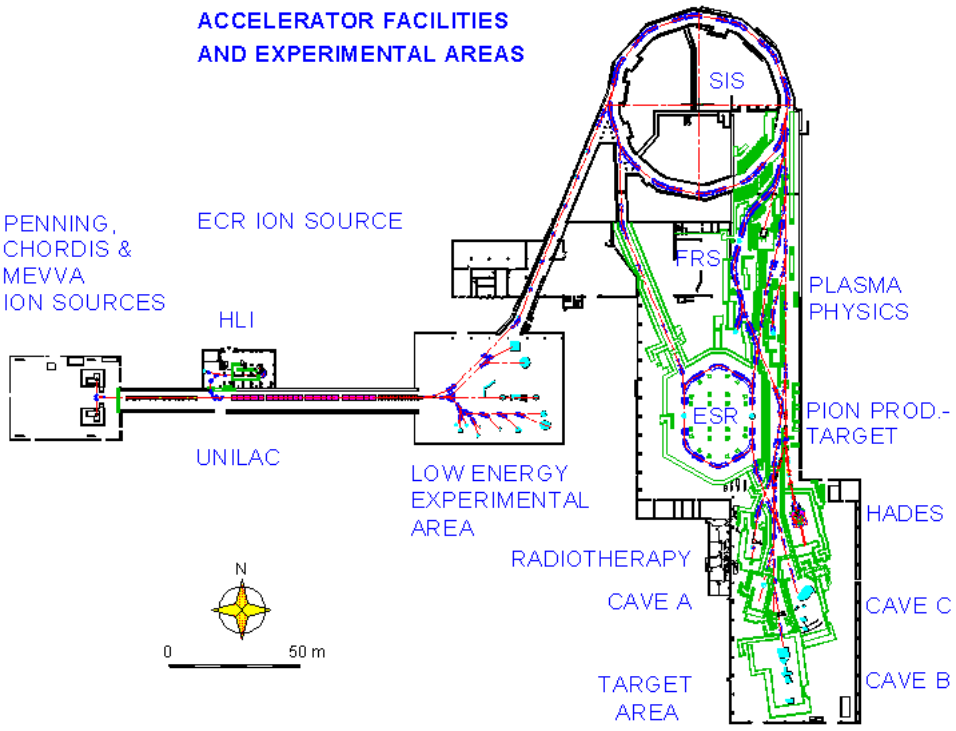

Figure 2.1: Schematic view represents placing of the different parts of the GSI Helmholtzzentrum accelerator complex. Starting from the left: ion sources, linear accelerator, low energy experimental areas, SIS-18 and finally the high energy experimental region with different experiments - among them the HADES spectrometer.

a designed maximum momentum for this system equals:

$$p = qB_0R_0,$$

$$\text{where : } B_0R_0 = 18\ [T * m] \text{ and this corresponds to: } 1 - 4.5\ GeV/c.$$

The SIS 18 consists of 24 bending magnets and 24 lenses. The vacuum in the beam pipe is on the level of $1.3 \cdot 10^{-7}\ Pa$. The acceleration of the ions is realized in two cavities. Each ion at this point experiences a potential of $16\,kV$ in frequency range of $0.8 - 5.6\ MHz$. Afterwards, the beam is transferred to the experimental areas , for example to the FOPI, HADES, FRagment Separator (FRS) or to the Heavy Ion Storage Rings (*ger. ESR - Experimentier Speicher Ring*). The full process of the ion acceleration takes $\sim 1 - 3s$, depending on the required ion kinetic energy.

2.2 HADES Spectrometer

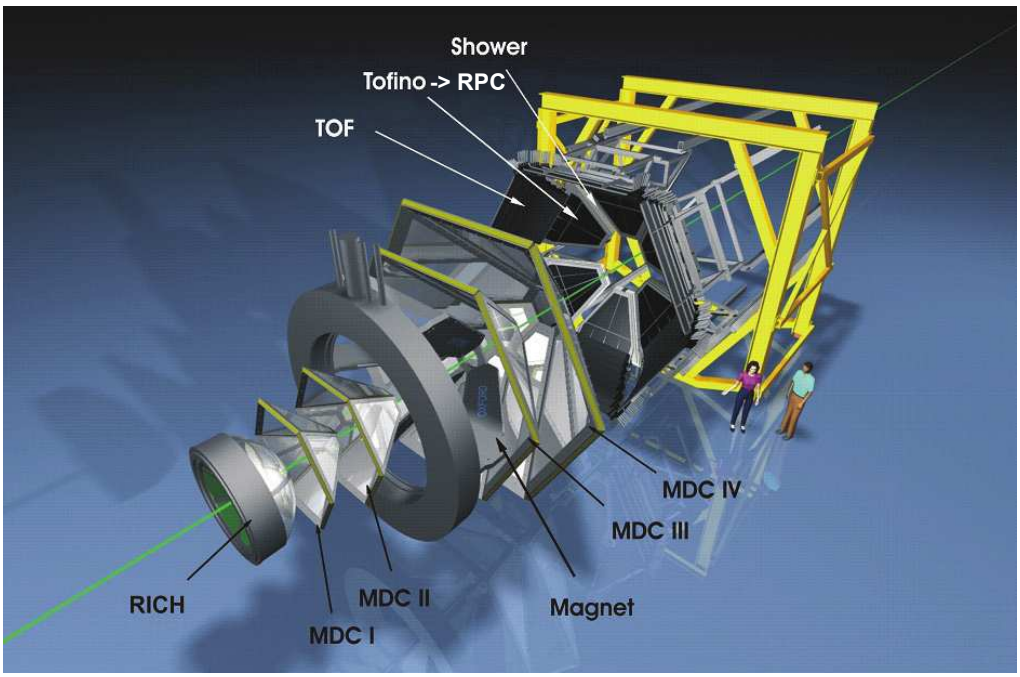

Figure 2.2: Artistic view of HADES spectrometer. Several different types of detectors are used: for direct electron identification RICH and Pre-Shower, time of flight measurements (TOF, TOFino) for particle identification MDC and superconducting magnet for the momentum reconstruction. The detector arrangement is according to a sixfold symmetry. The green line represents the beam axis. Detailed description of individual components can be found in the following sections.

The HADES[51] spectrometer, presented in Fig. 2.2, is located at the GSI Helmholtzzentrum für Schwerionenforschung GmbH in Darmstadt, Germany. Its purpose is to measure and reconstruct products of heavy ion, proton and pion collisions. Experiments are done with beams with energies up to a few $AGeV$ and intensities of typically $10^8 particles/s$. The main focus in the detector design was put on electron-positron pairs which carry undisturbed information about the high density phase of the collision. The chosen di-lepton channel has relatively small branching ratio. For example for the ω meson it is on the level of 10^{-5} and for the ϕ meson 10^{-4}. Therefore, the experimental set-up has to be able to cope with high interaction rates and to discriminate electron pairs from the overwhelming hadronic background. In more details these demands are related to:

- large acceptance - the spectrometer covers polar angles in the range of 18^o to 85^o and almost all azimuthal angles (besides the area of detector frames and magnet coils). This allows to have 35% acceptance for lepton pairs,
- mass resolution - in order to separate different particle species e.g. ω from ρ, the invariant mass resolution $\frac{\delta M}{M}$ of the di-electrons must be below 1%,
- high interaction rates - the detector and its electronics has to cope with $2 - 4 \cdot 10^4$ triggered interactions per second to provide sufficient statistics in the interesting decay channels,
- trigger - designed in such a way, that it allows to accept events with electrons and discards non relevant data,
- high granularity - facilitates the particle tracking in a high multiplicity environment.

All specifications mentioned above define the HADES experimental setup. It consists of several different detector systems:

- Multiwire Drift Chambers (MDC),
- Superconducting electromagnet,
- Ring Imaging CHerenkov detector (RICH),
- Time Of Flight TOF and TOFINO,
- Pre-Shower,
- START and VETO,
- Resistive Plate Chambers (RPC).

This set of different detectors is versatile such that it allows to measure, besides the electron pairs, hadronic products of reactions. In this dissertation (chapter 4) K^+ K^- identification will be described. To present the whole picture of the HADES spectrometer functionality it is necessary to focus on its different components, described in the next sections.

2.2.1 Multiwire Drift Chambers

The Multi Wire Drift Chamber detector, shown in Fig. 2.3, allows to measure a position, direction, energy loss per length and together with the magnetic field of the superconducting magnet (see subsection 2.2.2) momentum of the particle.

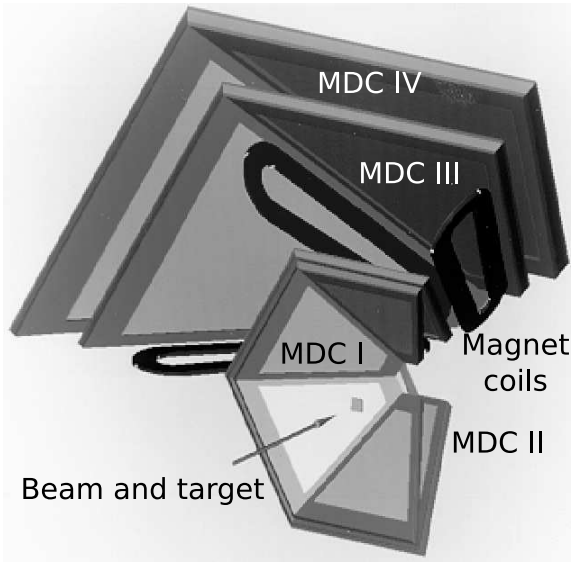

(a) Artistic view of MDC set-up together with a magnet. For the sake of the clarity a few MDC modules were removed from the picture. MDC detector, which is consisting out of 24 modules, is logically divided into four planes. First two (MDC I and II) are placed in front of the magnetic field, created by the superconducting magnet. The two others (MDC III, IV) are put behind the magnetic field.

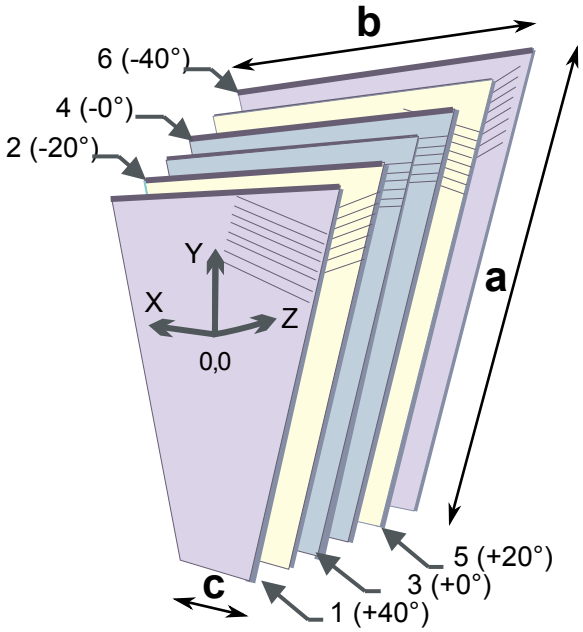

(b) One MDC module consists out of six differently orientated anode wire planes and 7 cathode planes (for better visualization the cathode wire planes are not shown).

Figure 2.3: The MDC detector

In order to be able to measure all these parameters with desired resolutions (e.g. 1% mass resolution for the ω meson) the detector is divided into four layers. Each layer consists of 6 modules located in individual HADES sectors. One module covers almost 60^o of azimuthal angle and polar angle from 18^o till 85^o. The size of the modules depends on the layer number. The dimensions of all planes are listed in Tab. 2.1. To keep the same cell granularity the distance between the wires also increases and translates to the cell

sizes ranging from 5×5 mm to 15×10 mm for the innermost to the outermost chambers, respectively.

Table 2.1: Dimensions for the different MDC planes (see fig. 2.3b).

Plane	a[mm]	b[mm]	c[mm]
I	839	767	139
II	1049	905	205
III	2139	1804	310
IV	2689	2224	345

The inclination of the detector, with respect to the vertical position, is chosen in such way, that the trajectory of the particles, which paths are the shortest from the target to the MDC, are perpendicular to the detector (see Fig. 2.3a). A chamber module consist of 6 field/sense (anode) planes and 7 cathode planes (sense wires have potential of 0 V and cathodes 2 kV). The wire orientation are established in such way (see Fig. 2.3b), that they are rotated by $\pm 0^o, \pm 20^o, \pm 40^o$ with respect to the x axis in Fig. 2.3b. For the two 0^o planes, the wires are shifted between each other by half of the distance between the wires to determine, on which side of the sense wires the particle is passing by.

To measure momentum a track deflection in a toroidal magnetic field is determined. The magnetic field is created by the superconducting magnet between planes I-II and III-IV. When the parameters of the magnetic field, particle charge and the deflection angle are known then the momentum of the particle can be calculated. With the achieved position resolution of 120 μm per wire plane a typical momentum resolution amounts to $2 - 3\%$ for protons and pions and $1 - 2\%$ for electrons, depending on the particle momentum[51].

On top of this basic tracking feature, MDC system is used to perform the particle energy loss (dE/dx) measurement. The measurement itself rely on the gas ionization in the chamber. HADES MDC chambers operate with gas mixture of He-Isobutan with the ratio of 3 : 2. The admixture of isobutan is necessary to absorb photons, created by an avalanche. The minimum energy needed for He ionization is 25 eV. When the particle is crossing the module, it creates so called primary electron-ion pairs. Electrons are accelerated near the anode wires and acquire enough energy to ionize an additional

He atoms (secondary ionisation). This process leads to development of the avalanche with electrons and ions drifting in the opposite directions. The current created by the avalanche (mainly moving ions) is then amplified and shaped in a front-end electronics based on a ASD8 ASIC[52]. Once the signal crosses a predefined level, a logic pulse is created for the drift time measurement. In addition Time Over Threshold (TOT) is created. The width of this signal is proportional to the signal amplitude and hence energy loss.

The dependency of dE/dx is described by the Bethe-Bloch[53] formula:

$$-(\frac{dE}{dx}) = (4\pi N_A r_e^2 m_e c^2)\frac{Z}{A}\frac{z^2}{\beta^2}[\frac{1}{2}ln\frac{2m_e c^2\beta^2\gamma^2 T_{max}}{I^2} - \beta^2 - \frac{\delta}{2}] \text{ where :}$$

N_A : Avogadro's number $= 6.022 \times 1023\ mol^{-1}$,

r_e : classical electron radius $= 2.817 \times 10 - 13\ cm$,

I : mean excitation potential,

m_e : electron mass,

Z : atomic number of the absorber,

A : atomic weight of the absorber,

z : charge of the particle in e units,

$\beta = \frac{v}{c}$: beta of the particle, $\gamma^2 = \frac{1}{1-\beta^2}$,

σ : density correction,

T_{max} : maximum energy deposit in a single collision.

and is utilized for the particle identification. Combining measurements from individual 24 MDC wire planes, a truncated mean is calculated. The obtained resolution of the MDC energy loss measurement is around $\sim 6 - 7\%$ and it depends on the particle momentum [54].

2.2.2 Superconducting Electromagnet

As mentioned above, the magnetic field for the momentum measurement is created by the superconducting toroidal magnet. The design of the Iron-Less Super conductive Electromagnet (ILSE, [55]) accounts for several important requirements:

- it covers the HADES acceptance in azimuthal and polar angles,

- produces a transverse momentum kick $\delta p/p \sim\ 2-5\%$,
- magnetic field is negligible in the region of the Cherenkov detector and the time of flight wall detectors,
- it is build with light materials to reduce production of secondary particles.

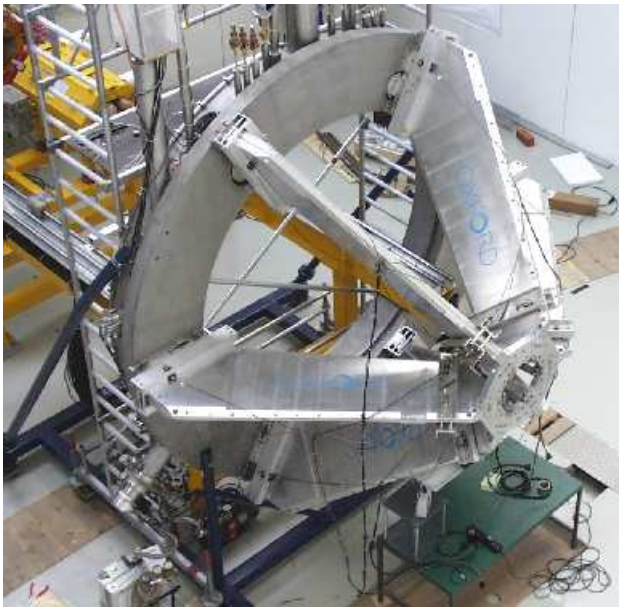

Figure 2.4: Super conducting magnet ILSE composed out of six coils located in the vacuum chambers.

The magnet is built out of six coils placed in the vacuum chambers. During the operation of the magnet the temperature inside the coils is lowered to the 4.56 K. Therefore the toroidal coils can work in a superconducting mode. The maximum allowed current for each coil is 3566 A. In total it gives for all coils $NI = 484000\ A$ and creates a magnetic field inside the coil $B = 3.77\ T$ and between the coils (in the air) 0.7 T. The direction of the current is such that the trajectories of the particles with positive (negative) charge were bent to the higher (lower) polar angles.

2.2.3 Ring Imaging Cherenkov Detector

The RICH (Ring Imaging Cherenkov, see Fig. 2.5) detector plays a significant role in the lepton identification. The concept of the RICH operation is based on the Cherenkov

effect: particles moving with a speed grater than the phase velocity of light in the given material emit photons [56]. Created electromagnetic waves are radiated in a specific polar angle direction, which can be described by a formula:

$$\begin{aligned} cos(\theta) &= \frac{1}{\beta n} \text{ where:} \\ n &- \text{index of refraction} \\ \beta &= \frac{V}{c} \end{aligned}$$

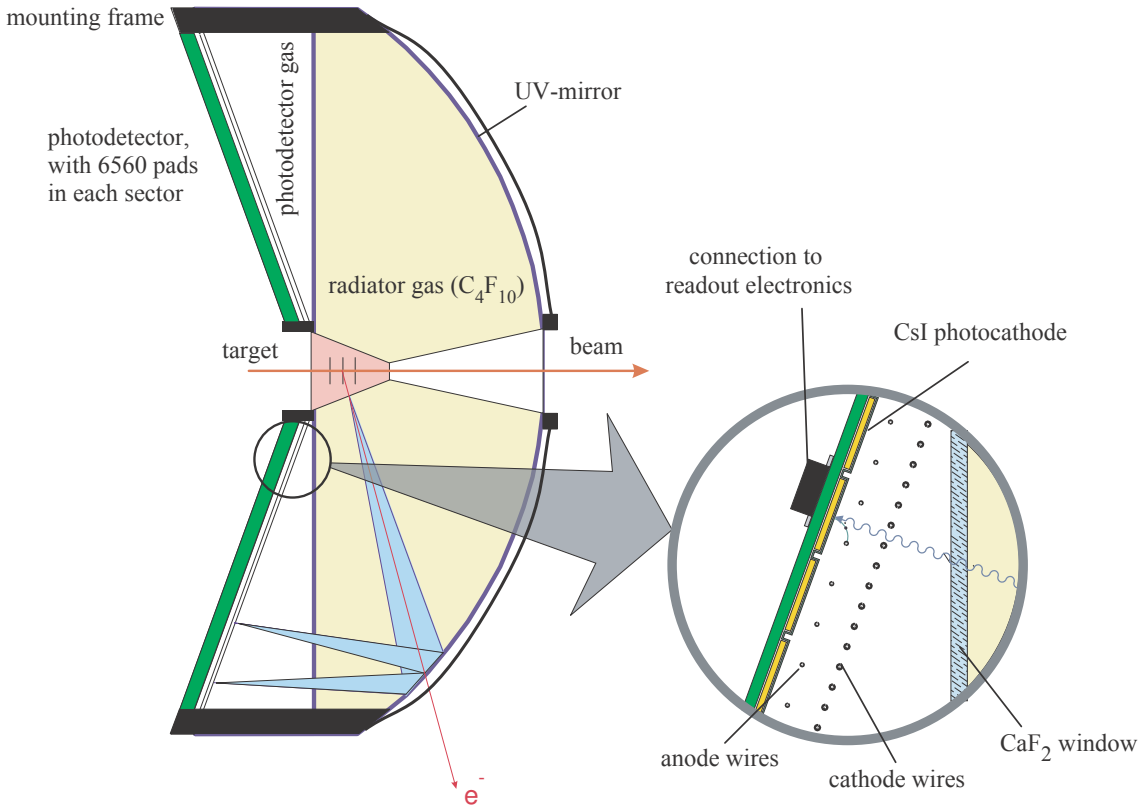

Figure 2.5: Cross-section of the RICH detector[57]. Di-leptons emitted from the target are crossing radiator gas (C_4F_{10}) and emit Cherenkov photons. The photons are reflected by the spherical UV-mirror, passing the CaF_2 window and are focused on the position sensitive photodetector.

The HADES RICH detector uses the advantage of threshold character of the Cherenkov effect. Particles created in the target, which is placed in the middle of the spherical RICH mirror, are traversing the C_4F_{10} radiator gas volume shown in Fig. 2.5. The $\gamma_{thr} = \frac{1}{\sqrt{1-\beta^2}}$ value for the radiator gas is 18.2. This puts constraints on the momentum of the particles, which can create the Cherenkov light. Therefore, only leptons with

momentum $p_{threshold} > 9,3\,MeV/c$ are able to create Cherenkov photons. For example, for pions the required momentum is $p_{threshold} > 2.55\ GeV/c$, which is not accessible in the reactions under study with the HADES. This allows to reduce the hadronic background in the interesting di-lepton signal.

Emitted light is deflected by the aluminized carbon mirror. The mirror material is selected due to its stiffness, small radiation length and a high reflectivity, which amounts to 80%. The shape of this mirror is such that it reflects the light and creates rings of radius of $5.5\ cm$ on a position sensitive photon detector. As it can bee seen in Fig.2.5, the photon detector is separated from the radiator gas volume by a CaF_2 window. Such construction is necessary to achieve good transmission for the ultra-violet light, which dominates the photon spectrum. The incoming photons impinge on a light sensitive material CsI, which cover position sensitive cathode plane of the photon detector, and induce emission of photo-electrons. The photo-electrons are accelerated in the electric field created by the anode wires of a multiwire proportional chamber, ionize the detector gas and generate the electron avalanche. Created ions travel to the cathode and this produces a signal amplified by the front-end electronics. In average $8-15$ photons, depending on the polar angle, are detected.

2.2.4 TOF Detector

The TOF detector (Fig. 2.6) covers polar angles from 45° to 85° and it is built out of six sectors (Fig.2.6a). Each sector is composed out of 8 modules, each one consisting of 8 scintillator rods (BC408). The structure for one sector is presented in Fig.2.6b. The area of the rodes cross sections varies from $2 \times 2\ cm$ for the four lower ones to $3 \times 3\ cm$ for the upper one. Also the length of the rods changes from 147.5 cm to 236.5 cm.

The purpose of this detector is to measure a time of flight of the particles created in the target. The particle crossing a scintillator rod creates light, which is transported to both ends of the detector. Then it is converted to an electric signal in a photomultiplier (EMI 9133B). The information from the TOF is used also for a first level trigger (LVL1). It is based on a hit multiplicity, which for A+A collisions is a good measure of centrality. The data from the TOF system is acquired with $200\ ps$ time resolution, which corresponds

to the position resolution of $3-4$ cm. In the further analysis this has influence on the particle species separation based on the reconstructed velocity and momentum.

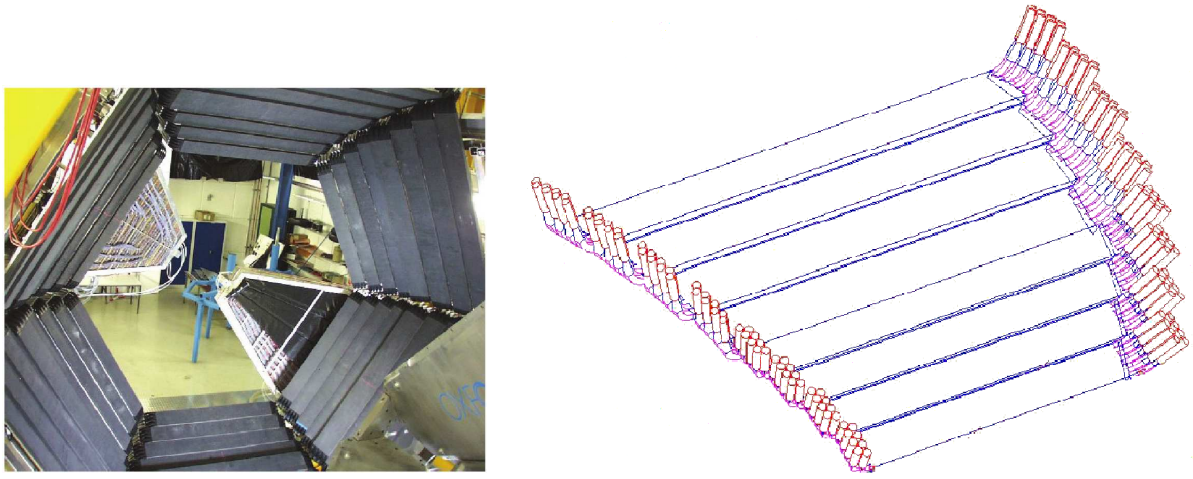

(a) View of TOF detector. It follows the six-fold symmetry of the HADES spectrometer.

(b) Detailed sketch of one TOF sector - 8 modules, each consisting of 8 rods.

Figure 2.6: TOF detector.

The time of flight, position and the energy loss (dE/dx) corresponding to the amplitude of the signal can be determined by means of the following formulas:

- time of flight:

$$\begin{aligned} t_{TOF} &= \frac{1}{2}(t_{right}+t_{left}) - \frac{L}{2V_g} \text{ where :} \\ V_g &- \text{is the group velocity of the light in the rod,} \\ t_{right},\ t_{left} &- \text{time measured on the left and right side of the detector,} \\ L &- \text{length of the rod,} \end{aligned}$$

- position:

$$x = \frac{1}{2}(t_{right}-t_{left})V_g$$

- and energy loss of the particle:

$$
\begin{aligned}
dE &= k\sqrt{A_{left}A_{right}}e^{\frac{L}{\lambda_{la}}} \text{ where:} \\
A_{left},\ A_{right} &- \text{is time over threshold (amplitude) of the signal,} \\
\lambda_{la} &- \text{light attenuation length in the rod,} \\
k &- \text{constant.}
\end{aligned}
$$

2.2.5 Tofino Detector

As already mentioned, the TOF detector covers only some part of the acceptance of the HADES spectrometer. The remaining part is covered by the TOFino (Fig. 2.7) detector.

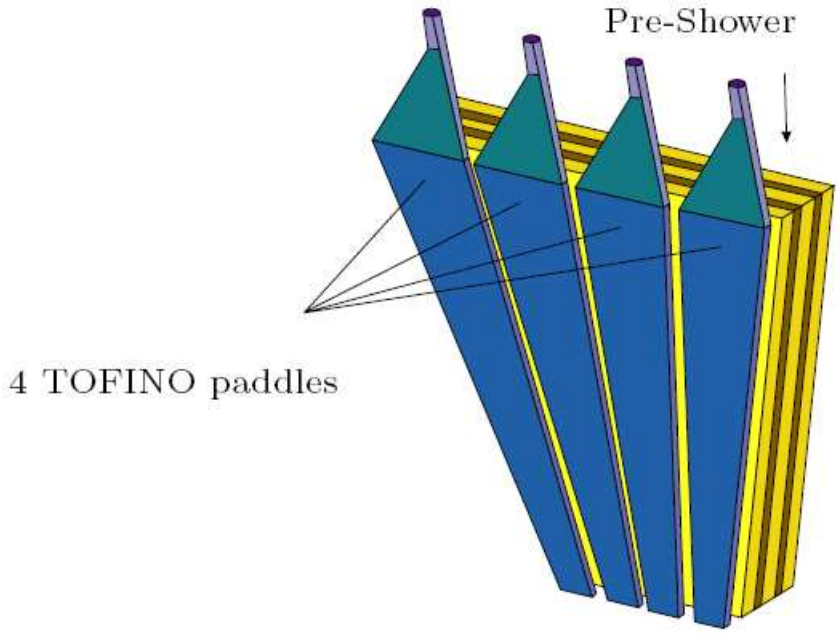

Figure 2.7: One sector of the TOFino detector built out of 4 paddles and placed on the Pre-Shower detector.

This detector has, because of funding problems, much smaller granularity - four scintillator paddles per sector (in total 24 for the HADES spectrometer) arranged long wise to the beam axis. Like the previous TOF detector it is used to extract time of flight information:

$$
\begin{aligned}
t_{tof} &= t - \frac{x_{PreShower}}{V_g} \text{ where:} \\
V_g &- \text{ is a group velocity of the light in the paddle,} \\
t &- \text{ time registered by the photomultiplier.} \\
x_{PreShower} &- \text{ hit position derived from the Pre-Shower}
\end{aligned}
$$

The signal is readout from one side only, which makes it impossible to determine the hit position from the detector alone. This information is taken from the Pre-Shower detector (subsection 2.2.6, see fig. 2.7). Also here energy deposit can be extracted from the amplitude of the signal.

The main disadvantage of this detector is its low resolution of 400 *ps* and low granularity. These facts were the main reason of replacement of this detector with a high granularity Resistive Plates Chamber (RPC) detector (operational after 2008).

2.2.6 Pre-Shower Detector

The Pre-Shower detector (Fig. 2.8) is also divided into six sectors. Each sector is constructed with three chambers separated by two lead converters. One chamber is built with two cathode planes and one anode plane, with sense and field wires displaced by 7.5 mm. One cathode plane is subdivided into pads (32×32) with individual read-out. The main goal of this detector is to distinguish electrons from hadrons by means of an electromagnetic shower produced inside lead converters. This method supplements TOF measurement in a region where particles have higher momenta and hence are more difficult to separate by the TOF method.

When an electron is passing the detector, it loses the energy in the lead converters and produces the electromagnetic shower. This happens because a high energy electron, when scattered in the electric field of atoms also emit electromagnetic radiation called bremsstrahlung (deceleration radiation). The bremsstrahlung is strongly dependent on the mass of the particle. It is inversely proportional to the squared mass, hence important for the electrons.

A basic idea of the operation of Pre-Shower detector is shown in Fig. 9.20. Emitted photons are converted into electron-positron pairs . These pairs again emit photons which

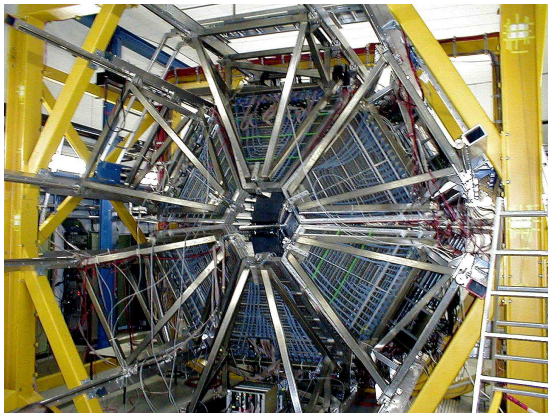

(a) Photograph of the Pre-Shower detector mounted and fully equipped with readout electronics.

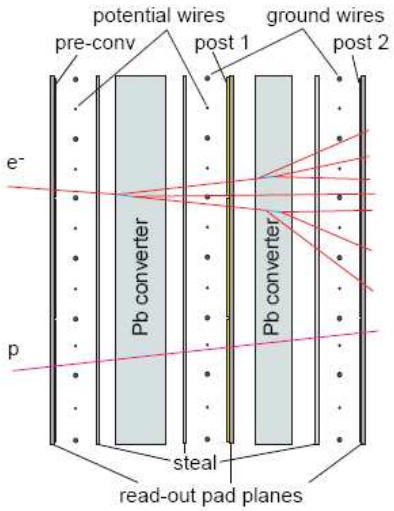

(b) Cross section of the Pre-Shower sector. Three chambers separated with lead converters and the response of the detector to two different types of particles (electron and proton) are schamatically shown.

Figure 2.8: Pre-Shower detector.

converts and this produces the electromagnetic shower. By comparing an integrated charge signal from 3×3 pads signal in the pre (before converter) and post1 and/or post2 (behind the converters) chambers one can differentiate electrons from hadrons - the signal becomes more significant in the post1/2 chambers for the electrons.

2.2.7 Start and Veto Detector

VETO and START detectors are symmetrically built diamond detectors. The diamonds are created with so called Chemical Vapor Deposition technique (CVD,[58]). This kind of material ensures a fast response, small secondary particles production (due to a small thickness of the detectors) and very good time resolution of $20 - 30$ ps. The detectors consist of eight sectors of diamond aligned with respect to each other (Fig. 2.9a). Both detectors are normally placed $75\,cm$ away from the target (Fig. 2.9b).

When a particle crosses the diamond detectors it produces electron-hole pairs which move towards metal electrodes, attached to the diamond and kept at potential of 250 V.

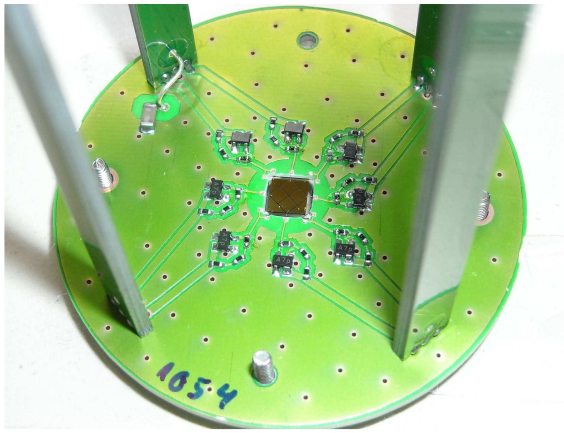

(a) START/VETO detector composed of eight small detections fields (4 inner and 4 outer regions) with transistor amplifiers [59].

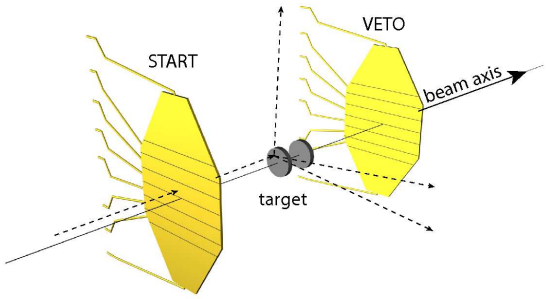

(b) The Placement of the START and VETO detectors according to the beam and the target.

Figure 2.9: START and VETO detectors.

The signal from the START detector initiates a first level (LVL1) trigger decision if there was no signal in the corresponding segment of VETO detector. Such case indicate that there was a reaction in the target.

These detectors are routinely used for heavy ion reactions. However, they appeared not suitable for the p p experiments because of too low efficiency. Only recently, new development based on mono-crystal diamond material resulted in successful operation. However, for the $p+p$ experiment described in this thesis no START detector was used.

2.2.8 Forward Wall Detector

The Forward Wall detector presented in Fig. 2.10 is a newly installed detector. Its main purpose is to detect the spectator particles in deuteron proton reactions and event plane reconstruction in A+A collisions. It covers polar angles from $7,1^o$ to 0.13^o. It consists of three different size scintillators and photomultipliers modules. The size of modules varies from $40\ mm \times 40\ mm$ for 156 modules, $80\ mm \times 80\ mm$ for 88 pieces to $160\ mm \times 160\ mm$ for 76 on the border of the detector. In total there are 320 scintillator and photomultiplier modules (see Fig.2.10a).

Having the time of flight with typical time resolution of $\sigma_{tof} = 400ps$ and angle with respect to the beam, one can calculate the velocity. If the assumption is made for the

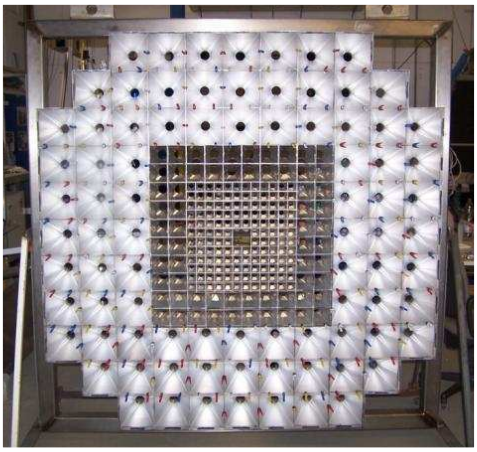

(a) Front view of the Forward-Wall detector without mounted detectors. Size of the modules increases when going from the inner to the outer area of the detector.

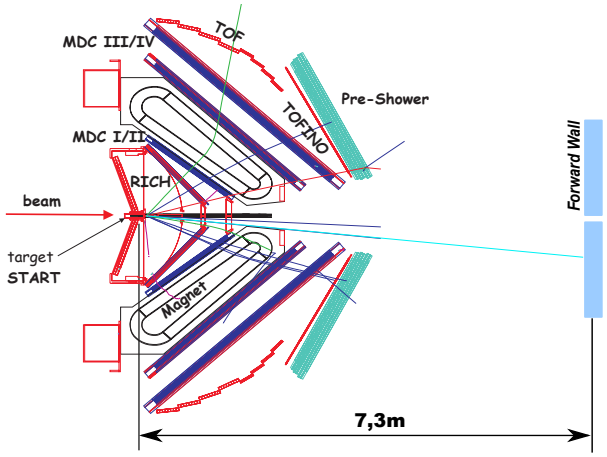

(b) Sketch of the HADES spectrometer and the placement of the the Forward Wall module.

Figure 2.10: Forward Wall detector.

particle type (e.g. proton in deuteron proton reaction), it is also possible to estimate the momentum.

2.2.9 Resistive Plate Chamber Detector

The Resistive Plate Chamber (RPC, [60], Fig. 2.11a) detector replaced the TOFino detector in 2008. Therefore, this detector was not used during the data taking in the experiment described in this thesis.

The requirements for the newly constructed detector are challenging. It has to cope with rates of the order of $\frac{1000 particles}{cm^2}$ and provides double hit rates below 10%. In order to distinguish leptons from pions it has to have a very good time resolution. As demonstrated in series of experiments, the detector achieves 70 ps time resolution [61], which is enough to separate pions from electrons up to momentum of 400 MeV/c. The HADES RPC detector is, as most of the other detector systems, composed out of six sectors. Each sector has two partially overlapping layers of the individually shielded RPC cells, which is shown in Fig. 2.11a. One cell of the RPC consists of:

- shielding of the cell (Fig. 2.11b,1),

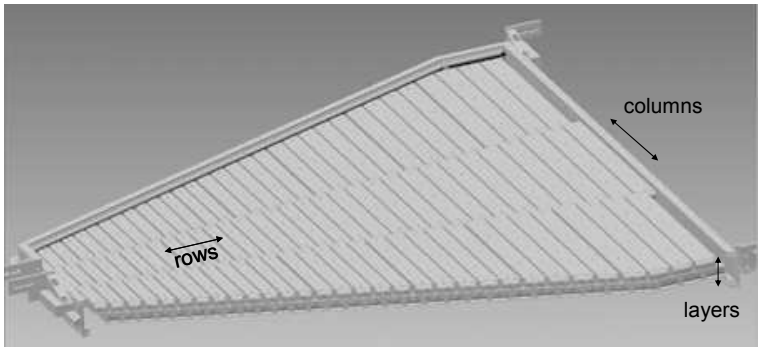

(a) Sketch of the RPC sector. It is composed out of 31 rows x 3 columns x 2 layers = 186 cells.

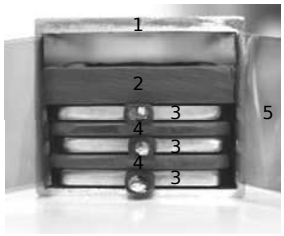

(b) The construction of the individual RPC cell.

Figure 2.11: RPC detector.

- plastic pressure object (2),
- aluminum electrodes (3),
- glass plates (4),
- kapton insulation (5).

The cell is filled with admixture of SF_6 and $C_2H_2F_4$ gas. To the electrodes a high voltage (5 kV) is supplied and when a charged particle is crossing the cell it ionizes the gas. The electrons are accelerated in the electric field towards the anode. This causes further ionization and creates an electron avalanche and a measurable electric signal. The signal is detected on both sides of the detector cell, by dedicated front-end electronics [62]. It allows, as in case of the TOF detector (subsection 2.2.4), to determine the hit position but with better (8 mm) resolution. The amplitude of the created signal is used to improve the time of flight measurments by walk corrections.

2.2.10 Target

In the HADES experiment the type of the target depends on the currently realized physics program. It was either thin foils or a liquid form of hydrogen. For instance in a $C + C$ at $1 - 2GeV$ a 5 mm thick foil was used. The density of this material was 2.15 g/cm^3 and interaction probability was 5%.

Figure 2.12: LH_2 target during the 2007 $p+p$ at 3.5 GeV beam time.

In case of $p+p$ reactions at 3.5 GeV described in this thesis, the prepared target was composed out of liquid hydrogen (LH_2, Fig. 2.12). It has been developed at Institute de Physique d'Orsay (IPN).

It was built out of two vessels - one inside the other. The inner one (5 cm long with a diameter of 2.5 cm) was holding the LH_2 liquid and it was operating at $20K$ temperature and at normal atmospheric pressure. The outer one was providing a thermal isolation. The system was operated in the vacuum and the target was closed with a $100\mu m$ thick Mylar foil. The interaction probability with the Mylar foil was 0.05%. This was much lower in comparison with LH_2 target interaction probability - 0.7%, and hence did not produced significant background.

2.3 Trigger and Data Acquisition System of HADES spectrometer

The HADES experiment has a significant amount of electronic channels, which is around 80000. It is neither possible nor necessary to transport and store all the data on the storage devices. Therefore the experiment had two levels of the triggers for an event selection. The system for the data taking is briefly described in the following sections (status during the 2007 $p+p$ year production beam time). The Forward Wall readout hardware will be presented in chapter 10 in more details as an example. This choice is based on the fact,

that author of this dissertation participated in the development of the readout electronics for the Forward Wall detector.

2.3.1 First Level Trigger

As mentioned in the introduction of this chapter, to reduce the amount of the data two levels of the triggering are used in HADES. The first level trigger (LVL1) is generated based on a predefined signal multiplicity from the TOF and the TOFino detectors and, if available, with START(no VETO) signal. The TOF/TOFino multiplicity conditions used in the $p+p$ experiment described in this thesis are presented in Tab.2.2.

Table 2.2: Multiplicity conditions during pp at 3.5 GeV kinetic energy beam.

Multiplicity type	Downscaling
Mult.$\geqslant 2$	256
Mult.$\geqslant 3$	1

The main trigger used for the analysis of the $pp \rightarrow ppK^+K^-$ channel was Mult.$\geqslant 3$. The other trigger was used for the normalization purposes (pp elastic scattering) and was downscaled to avoid too large dead time.

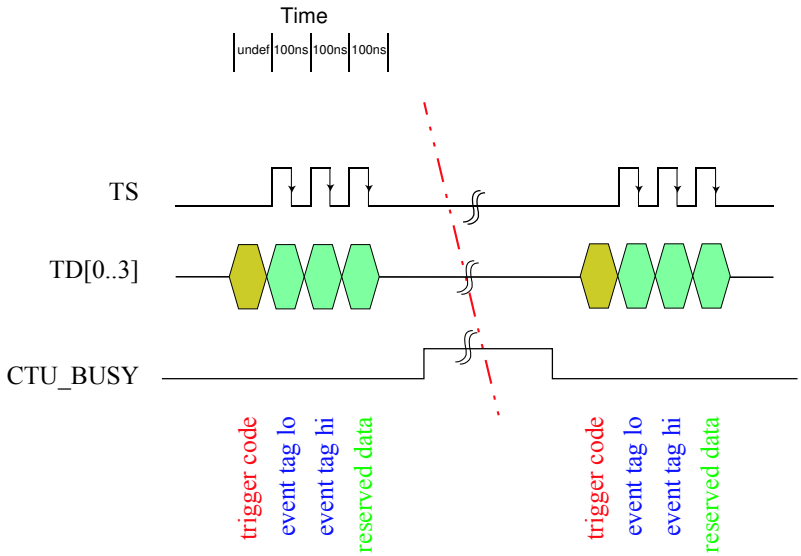

Figure 2.13: LVL1 trigger data transmission. It contains information about the trigger type, number(tag) and reference time.

The LVL1 trigger signal was generated in the Central Trigger Unit (CTU) and was distributed via HADES trigger bus with differential signals presented in Fig. 2.13. The information which was contained in the LVL1 trigger data transfer was following:

- reference time - sent on TS line and it was used for synchronization of the data from all readout systems,
- trigger code - valid on the rising edge of the reference time signal, mainly only two types of the code was used: take data and calibration,
- trigger tag - trigger sequential number saved into the headers of transferred events, allows event builder to merge all incoming data into one file without risk of mixing it.

After receiving LVL1 trigger the data was stored in the local readout electronics buffers awaiting for a second level trigger decision (LVL2).

2.3.2 Second Level Trigger

After each LVL1 trigger decision the data from the Pre-Shower, TOF and RICH detector was also simultaneously processed and sent to the Matching Unit (MU,[63]) where electron signal was searched in real time to generate the LVL2 trigger. The schematic overview of the HADES trigger system is presented in Fig.2.14.

The algorithms for the data preprocessing were realized in the electronic hardware, integrated locally with the detector specific data readout boards. In the Shower IPU (Image Processing Unit) the algorithm [64] was checking weather electromagnetic shower occurred in the acquired event. This was done by checking if the accumulated charge in the fired pads of clusters of the three consecutive Pre-Shower chambers was increasing.

The RICH IPU [65] was searching for the ring patterns. Due to the special design of the RICH detector (pads with tuned sizes) the ring radius is always 8x8 pads. Nevertheless it is still a challenging task to find a ring on top of an electronic noise and background originating from the hits of charged particles on the pads.

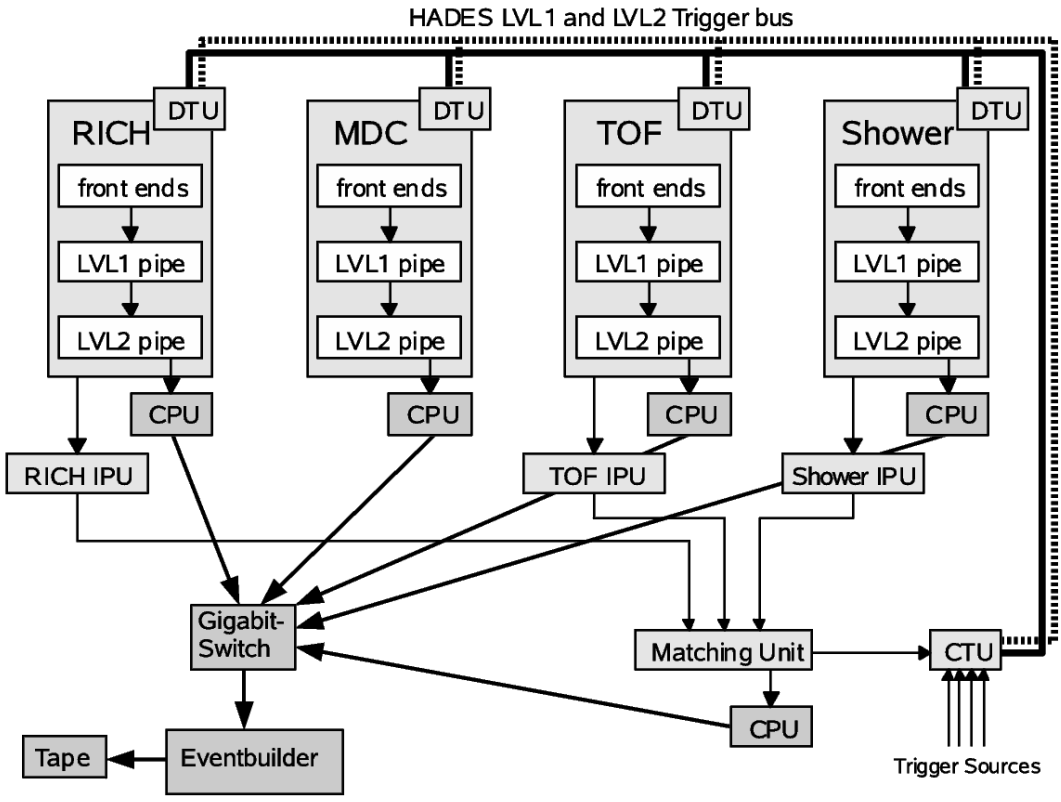

Figure 2.14: Overview of the HADES trigger and readout system. The Central Trigger Unit (CTU) accepts the multiplicity triggers coming from the TOF and TOFino detectors and converts them into the LVL1 trigger. After receiving the LVL1 trigger the Detector Trigger Units start the readout electronic and the experimental data is stored in LVL1 pipe. In parallel the pattern recognition algorithms are executed in the detector specific Image Processing Units (IPUs). The matching unit (MU) combines the information from the IPUs and based on the results sends either positive or negative decision (LVL2 trigger). If the decision was positive the data is read out via the VME CPUs and transported to the Event Builder (EB).

Based on the information from the TOF and START detectors, the TOF IPU calculated particle velocity and by this mean it could distinguish electrons or positrons from slower particles.

Finally, the MU was combining the corresponding information from the RICH and the Pre-Shower/TOF IPUs and performing spatial correlation of the hit position of the electron candidates found by these detectors. Based on this grounds, the data was discarded

or transported further to the Event Builder (EB), where it was collected and sent further to record on the tapes.

For the presented analysis of the $pp \rightarrow ppK^+K^-$ it is essential to mention, that part of the data (LVL1 events) is stored independent on the LVL2 trigger decision. Such down-scaled events (down-scaling was defined in the MU) allow to perform hadronic analysis.

Chapter 3

Data Analysis

3.1 Introduction

The data presented in this thesis have been taken during 3 weeks in April and May 2007. The experiment was done using the proton beam with a kinetic energy of 3.5 GeV. A total amount of $1.7 \cdot 10^9$ events have been collected. Among these events $1.15 \cdot 10^9$ were produced by the multiplicity 3 trigger (M3). In order to be able to identify particle tracks inside the HADES spectrometer it is necessary to combine information from different detector subsystems. The HADES collaboration has developed a standardized strategy for a such complex analysis. HYDRA (**H**ades S**y**stem for **D**ata **R**eduction and **A**nalysis [66]) is a software package based on the C++ ROOT platform [67]. With the help of this program **D**ata **S**ummary **T**apes (DST) files for the further analysis are created, which includes a calibrated data from all detector systems. In more detail, the DSTs files contain identified hits on RICH, TOF/TOFINO and Pre-Shower with corresponding parameters like coordinates, time of flights values, energy loss etc. and also reconstructed tracks in MDCs. In the next step of the analysis a PAT (**P**ostDST **A**nalysis **T**ool [68]) is executed (see for the details chapter 4). In this part of analysis particle identification of a specific reaction decay channel is done and kinematic variables as the invariant masses, emission angles of reconstructed particles etc. are calculated In the last stage of the analysis the obtained results are compared with simulation data, which are processed in exactly the same way as the real data. The whole path of the experimental data analysis is shown in

Fig. 3.1.

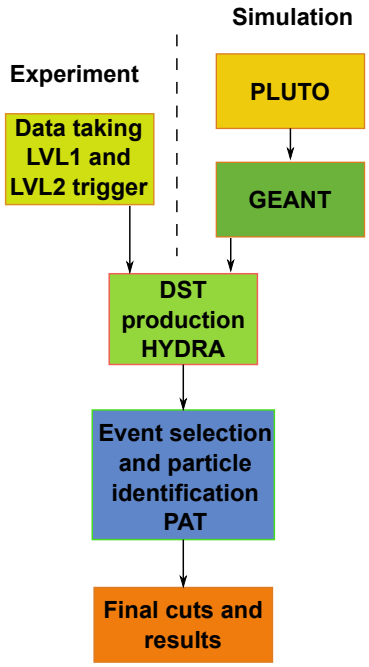

Figure 3.1: Analysis flow - experimental and simulation data.

The main purpose of this analysis was the identification of the $pp \rightarrow pp\phi$ exclusive channel and the estimation of the ϕ meson production cross section. In order to obtain corrections due to acceptance and reconstruction efficiency losses, detailed simulations are needed to determine the effects of the apparatus (see chapter 6). Simulated events are generated using a Monte Carlo event generator (PLUTO [69]). It produces events for a given reaction channel based on physics model, defined by the user. Particle properties and decay channel are taken from the Particle Data Group [12] and are stored inside the PLUTO data base. The events from the PLUTO program are then used as an input to the Detector Description and Simulation Tool called Geant [70]. The Geant simulation environment is used to define the HADES geometry and material budget. The simulated tracks of particles are transported through the HADES spectrometer and generate detector hits. These hits are created out of a realistic physical models of processes taking place inside the detectors. Next, the hits are digitized and packed into the events, which represents the response of the HADES detectors including front-end and readout electronics. The following steps of data processing are the same as for the experimental data.

Having both, experimental and simulated data, it is possible to calculate respective

corrections due to reconstruction efficiencies and detector acceptance. Finally, the exclusive cross section of ϕ meson production (chapter 7) can be extracted. For the investigation of the OZI rule violation (chapter 1.4) ratio of the ϕ to ω meson cross section needs to be calculated. The respective $pp \rightarrow pp\omega$ exclusive production must be analysed. This analysis has been performed by K. Teilab from University of Frankfurt and the respective cross section for ω production has been derived [71].

3.2 Tracking in HADES Spectrometer

As mentioned before, the HYDRA package is used to reconstruct tracks and hits related to the particles measured inside HADES acceptance.

First, the particle trajectory is reconstructed based on the position and the drift times of fired wires in the MDC detector. Based on this partially reconstructed tracks, so called track segments, can be obtained. The track segments are created independently for the MDC I/II (inner) and MDC III/IV (outer) doublets. In next steps both tracklets are merged together and aligned with the TOF or the TOFINO/Pre-Shower hits.

The mechanism of track segment matching is presented in Fig. 3.2. The inner MDC track segments are projected to the target area assuming straight line approximation. Segments with best match to the target are selected. For outer segments all combination of hits are considered but then both, inner and outer MDC track segments are projected and matched on a special plane - kick plane. The kick plane is a hyperplane, obtained from simulations, which approximates the place of the deflection of charged particles in the HADES magnetic field just by sudden change - a "kick"- of the trajectory [72].

Knowing the deflection of a particle in the magnetic field of known strength and its charge one is able to calculate its momentum. This is done in two steps. First the cubic spline method [51],[73] is applied to calculate first approximation of the momentum. Second, based on the previous result, a fourth order Runge Kutta algorithm of Nystrom [74] is used. Implementation of this method solves differential equations of motion in the known magnetic field.

In order to identify electrons, the inner MDC track segments are matched with the rings reconstructed in the RICH detector and hits in the TOF or TOFINO/Pre-Shower

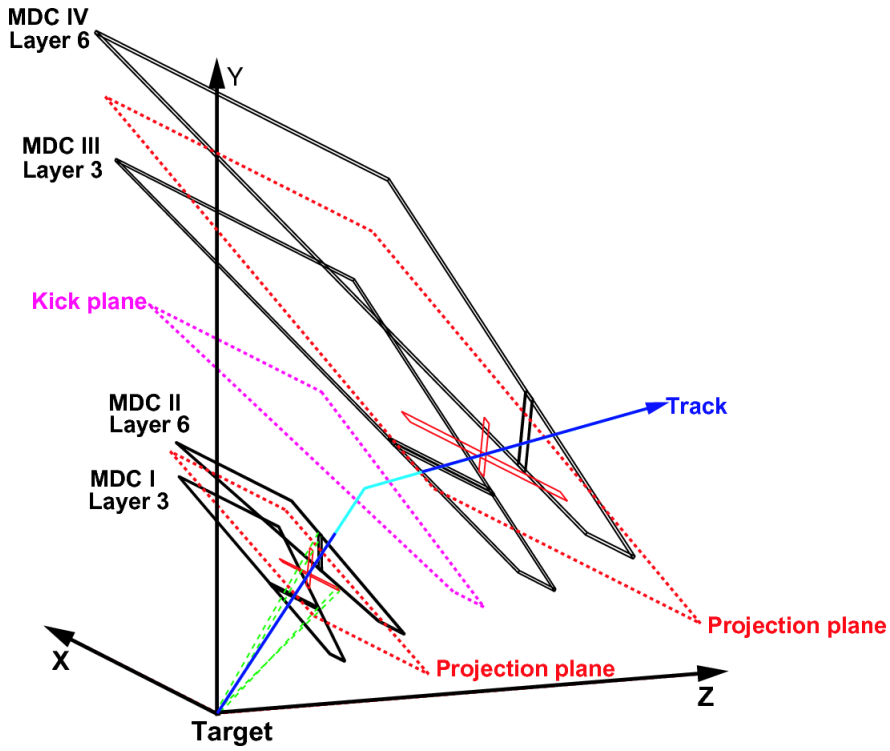

Figure 3.2: Sketch of the track reconstruction method. The inner MDC track segments are projected to the target area and to the kick plane. The outer MDC track segments are projected to the kick plane and are used to find the correlation with the hits in the META detector (TOF,TOFINO and Pre-Shower).

detectors.

For the hadron (proton, pion, kaons) identification the tracks are correlated with hits in the TOF or TOFINO/Pre-Shower detectors only. Having particle momentum and correlated time of flight and/or energy loss in the detectors a particle identification can be performed.

3.3 Time of Flight Recalculation

As it was already mentioned, there was no START detector in HADES set-up during $p+p$ experiment. Consequently, there was no direct information about time of the reaction which is mandatory for the velocity ($\beta = V/c$) calculation and, in next steps of analysis, for the particle identification. Therefore, it was necessary to recalculate the time of flight

(t_{new}) using different approach.

The method applied in this analysis was based on following information:

- measured stop times in the TOF and TOFino detector with respect to the LVL1 trigger time - denoted below as t_{tof},
- hypothetical time of flight calculated from the momentum and the path length of the reconstructed track assuming that mass of the particle (id) is known - denoted below as $t_{mom\ id}$.

One should note that measured time of flights t_{tof} are related to the calculated ones by simple relation: $t_{tof} = t_{mom} + \mathit{offset}$, where the *offset* is a time offset (time when the LVL1 trigger fired) changing event by event, which however, can be eliminated for a given event using time differences between particles produced in the reaction.

Let us illustrate the algorithm on example of the $pp \rightarrow pp\phi$ reaction channel and the $\phi \rightarrow K^+K^-$ decay branch. For the complete channel reconstruction only one proton and K^+, K^- pair identifications are necessary.

The time of flight for K^+ , $t_{new\ K^+}$, is obtained from the following equations:

$$t_{\Delta\ pK^+} = \frac{t_{tof\ p} - t_{tof\ K^+}}{2} \tag{3.1}$$

$$t_{mean\ pK^+} = \frac{t_{mom\ p} + t_{mom\ K^+}}{2} \tag{3.2}$$

$$t_{new\ K^+} = t_{mean\ pK^+} - t_{\Delta\ pK^+} \tag{3.3}$$

Likewise for the 2nd particle:

$$t_{new\ K^-} = t_{mean\ pK^-} - t_{\Delta\ pK^-} \tag{3.4}$$

The reference particle, which is chosen to be a proton, is calculated as hereafter:

$$t_{new\ p} = \frac{t_{mean\ pK^+} + t_{mean\ pK^-} + t_{\Delta\ pK^+} + t_{\Delta\ pK^-}}{2} \tag{3.5}$$

The time of flight recalculation for the ϕ meson exclusive analysis is done for all possible mass association to the three reconstructed tracks and associated t_{tof} for the given event.

There are in fact only 2 combinations per event to be considered since a negative charge particle is always assumed to be an antikaon. This assumption is of course later verified by means of particle identification cuts described below. For each combination, a correlation of the momentum and the velocity of the particle is plotted and compared to the expected ones for the kaons and the protons.

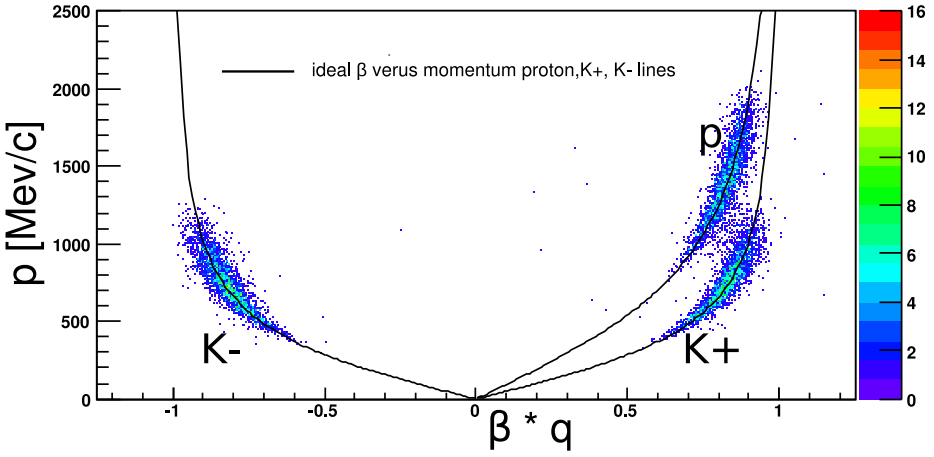

Figure 3.3: Time reconstruction in the β versus momentum representation. Black solid line shows proton, K^+, K^- masses.

To illustrate results of such recalculation and experimental resolution, events from the simulated reaction $pp \to \phi pp \to K^+K^-pp$ are displayed in Fig. 3.3. The displayed results is for the correct mass associations. In order to evaluate resolution effects important for the particle separation, the mass of the particle has been calculated from the measured momentum and velocity :

$$m = \sqrt{\frac{(1-\beta^2)p^2}{\beta^2}}$$

The results, mean and RMS values of the mass distributions, are presented as a function of momentum in Fig. 3.4 for protons and kaons. In Fig. 3.4a it is clearly visible that mean values of the mass distributions (fitted with a Gauss function) are in agreement with the expected masses of proton and kaon. Furthermore, the relative mass resolution is plotted as a function of the momentum in Fig. 3.4b . The resolution decreases for the increasing momentum. A better resolution obtained for the given momentum for the pro-

tons as compared to the kaons results from the time recalculation procedure which takes into account 3 and 2 time measurements, respectively. As one can expect a time error resulting from the time recalculation with more tracks is smaller (see eq.3.5).

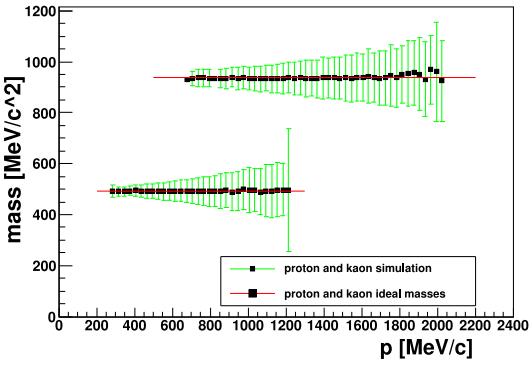

(a) Proton and kaon masses as a function of the momentum, with calculated σ. Red lines shows expected masses of the particles

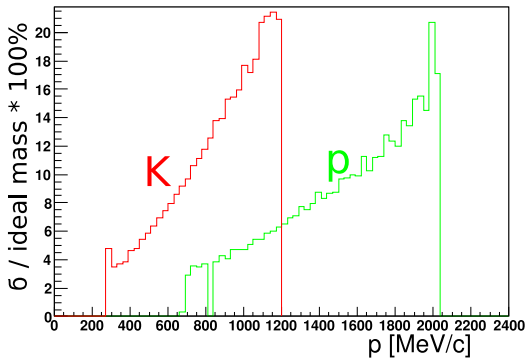

(b) Errors for the proton and kaon mass distribution as a function of the momentum.

Figure 3.4: Mass resolution as a function of the particle momentum resulting from the time reconstruction procedure.

Chapter 4

Event Selection and Particle Identification

The ϕ meson is reconstructed in the channel $pp \rightarrow \phi pp \rightarrow K^+K^-pp$. This decay mode has been chosen because of its large branching ratio - $49.2 \pm 0.6\%$. The particles, which are required to be detected for the exclusive channel, are at least two particles with a positive charge (proton and K^+) and one with a negative charge (K^-). Identification of these particles and reconstruction of their momenta are sufficient to retrieve full reaction kinematics (including not detected proton). Furthermore, the HADES acceptance for three prong events is higher by an order of magnitude as compared to reconstruction of four-prong events (two kaons and two protons).

In the next sections of this chapter applied cuts are described in more detail. In the first step of the analysis events containing 2 or 3 particles with a positive charge and one particle with a negative charge are selected. In the next step, particle identification by means of time of flight and energy loss in MDC is performed. In order to reduce a particle misidentification and to reduce the background in the ϕ meson mass region, cuts on the particle momenta applied. Thus, analysis procedure consists of following conditions imposed on reconstructed tracks:

- momentum cuts - section 4.1,
- particle identification via conditions defined on the particle mass calculated from the time-of-flight and momentum reconstruction - section 4.2,

- particle identification via cuts on MDC energy loss section 4.3.

If one of the particles is not fulfilling a given cut (e.g. the proton mass cut) then it is excluded from the hypothesis that it is a specific type of the particle. After all cuts, if there are more than 3 remaining particle candidates per event, event selection is made via global χ^2 test (section 4.4). Afterwards from the event only one combination is chosen with identified p, K^+ and K^- particles. Finally, when particles are identified, a p, K^+K^- missing mass is calculated and compared to the proton mass by means of one dimensional condition to select the ppK^+K^- reaction channel (section 4.5 and 4.6).

4.1 Momentum Cuts

The momentum distributions retrieved from the simulation of the $pp\phi$ exclusive channel are presented in Fig.4.1. It shows that they can be utilized to partially separate protons from kaons.

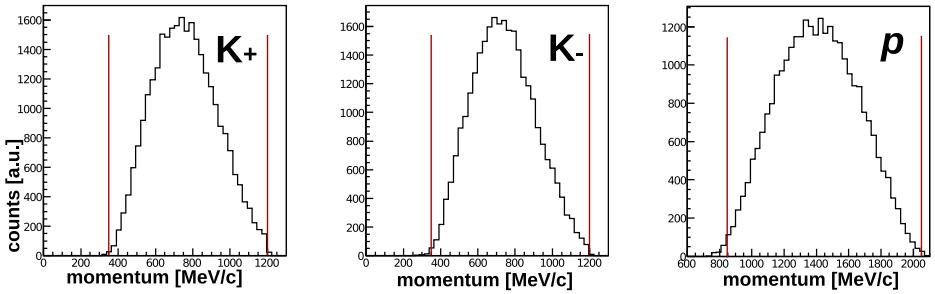

Figure 4.1: Momentum distribution for different particles - simulation. The red lines represent imposed momentum cuts.

In order to preserve maximal statistics for the relevant reaction channel a conservative conditions on the momenta distributions have been imposed (see Fig.4.1 red lines):

$$350MeV/c < K^+_{mom}, K^-_{mom} < 1200MeV/c$$

$$800MeV/c < p_{mom} < 2050MeV/c$$

It is clear that for the momenta smaller than 1200 MeV/c proton and kaons must be distinguished by other means, as explained in the next section.

4.2 Mass cuts

As described in section 3.3, because of the lack of START detector the time of flight reconstruction was mandatory. It was based on the hypothesis that a given event consists from one (or two) protons and two kaons. After assigning K^- identity to the track of the particle with a negative charge, two combinations per event (3 in case of 4 particles per event) were considered. Assuming a specific particle mass association to the remaining tracks corresponding time of flight were calculated from the measured momenta (t_{mom}), as given by equations 3.1-3.5 in section 3.3. Finally, from the reconstructed time of flights (t_{new}) particle masses were calculated and could be compared to the true ones by means of one dimensional conditions.

In order to determine widths of such conditions a dedicated simulation for the ppK^+K^- channel is performed. To illustrate the method, the condition for the proton identification is presented in detail below. Fig.4.2a shows a mass distribution as a function of the proton momentum as derived from the time reconstruction algorithm. This distribution is divided into 30 MeV/c momentum slices. Next, as shown in Fig.4.2b, the projection on the axis is fitted with a Gauss function.

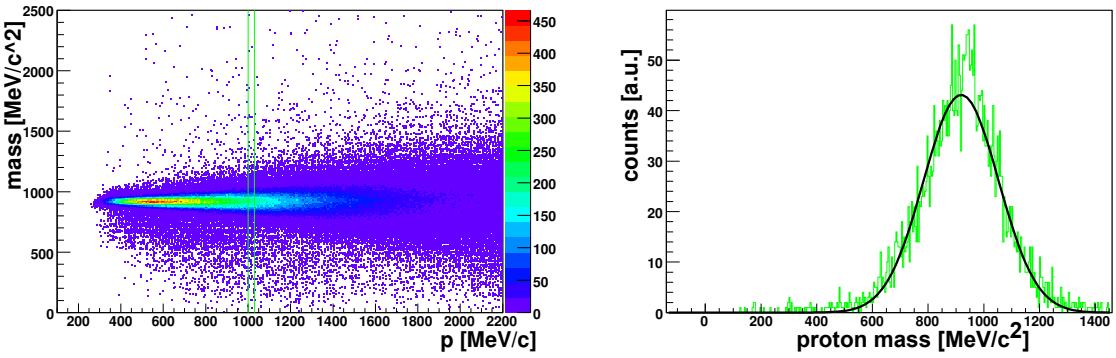

(a) Proton mass distribution as a function of the momentum for the ppK^+K^- channel.

(b) Reconstructed proton mass distribution for the 1000 MeV/c – 1030 MeV/c momentum region.

Figure 4.2: Determination of the width of the proton mass distribution based on simulation.

In this way, the mean value and σ of the mass distributions for protons and kaons as a

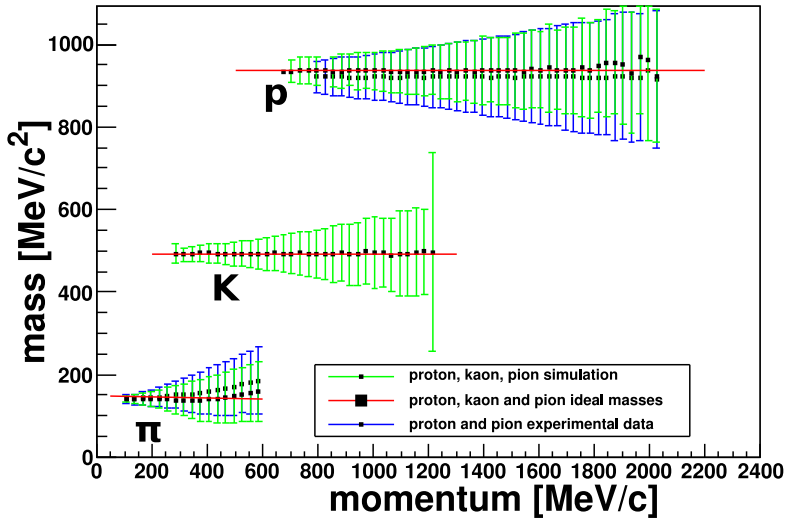

Figure 4.3: Distributions used to define momentum dependent mass cuts. The black points with green error bars show the simulation results, black points with blue error bars represent the experiment data.

function of the momentum (shown in Fig.4.3) is evaluated. For the particle identification, a mass window with the width equal to 2σ is defined for both protons and kaons.

Since the calculated widths are very important for the correct particle identification and later efficiency corrections they should be validated by a direct comparison with the ones derived from the experiment data. Unfortunately there is not enough statistics to obtain such comparison for the interesting ppK^+K^- channel. However, the reaction channel $pp \rightarrow pp\pi^+\pi^-$ is much more abundant and could be analyzed in this context. For the particle identification selections on the MDC energy loss, described in more detail in section 4.3, is applied by means of two dimensional conditions shown in Fig 4.4a. Furthermore, a cut on the $p\pi^+\pi^-$ missing mass around the proton mass, shown in Fig.4.4 by red lines, has been utilized to increase the purity of the channel selection. Using these events the widths of the proton and pion mass distributions could be extracted from the experimental data (Fig.4.3 black points with blue error bars) and compared to the simulated ones (Fig.4.3 black dots with green error bars). As it can be seen from Fig.4.3 both distributions are in agreement.

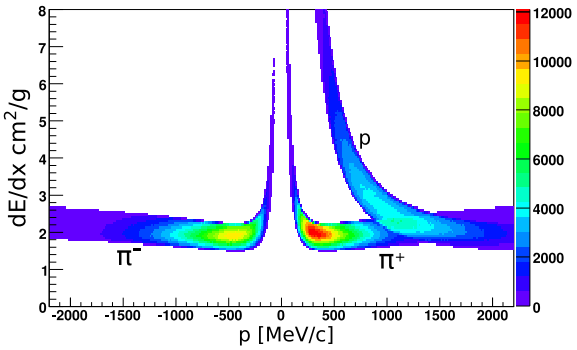

(a) MDC dE/dx cuts individually applied for pions and protons.

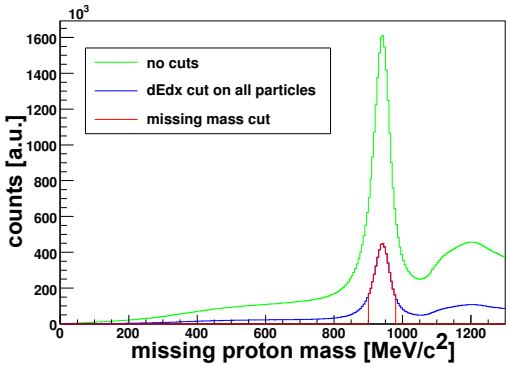

(b) $p\pi^+\pi^-$ missing mass distribution for the $pp \rightarrow pp\pi^+\pi^-$ event hypothesis in different stages of analysis. The green line is just after the particle identification, blue one after the dE/dx cuts and red one after the missing mass cut.

Figure 4.4: $pp\pi^+\pi^-$ selection for validation of proton and pion mass reconstruction algorithm

4.3 MDC Energy Loss Cuts

Particle identification by means of the MDC energy loss (MDC dE/dx) is very similar to the one used in the time of flight analysis with the exception that no event hypothesis must be used. The identification is performed by means of two dimensional conditions, extracted from the simulation, which were applied on the momentum versus dE/dx distributions.

In order to validate respective conditions the $p\ p \rightarrow p\ p\pi^+\pi^-$ reaction channel is used for the extraction of appropriate momentum dependent cuts. In order to select the $pp\pi^+\pi^-$ reaction channel particle identification by means of the time recalculation method were applied. Fig.4.5 (left panel) shows obtained mass distribution together with applied mass windows to select protons and pions. Finally, a condition on the $p\pi^+\pi^-$ missing distribution around the proton mass was imposed for the final selection of the reaction channel.

After the events with proton and two pions are uniquely identified, the MDC dE/dx versus momentum distribution is constructed and divided into 30 MeV/c momentum slices. For each slice a fit with the Landau function is made (example for the proton is shown in Fig.4.6).

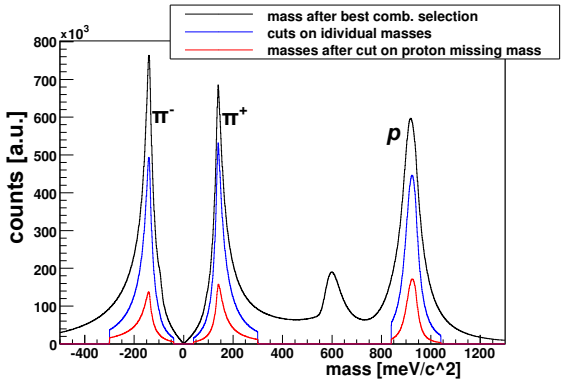

(a) Mass distributions reconstructed from time of flights with prominent peaks corresponding to protons and pions.

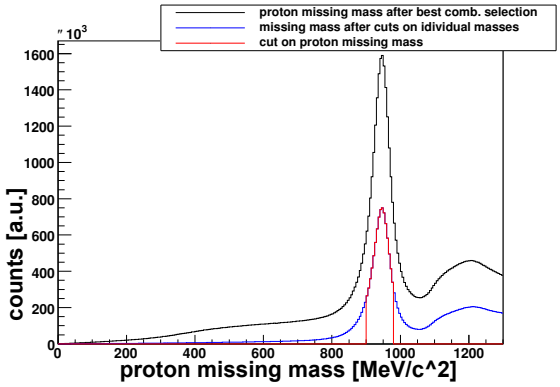

(b) Proton missing mass cut.

Figure 4.5: $pp\pi^+\pi^-$ selection for validation of the MDC dE/dx distributions for protons and pions.

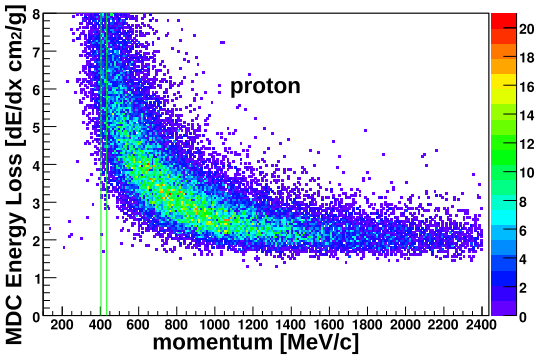

(a) Proton dE/dx distribution as a function of the momentum.

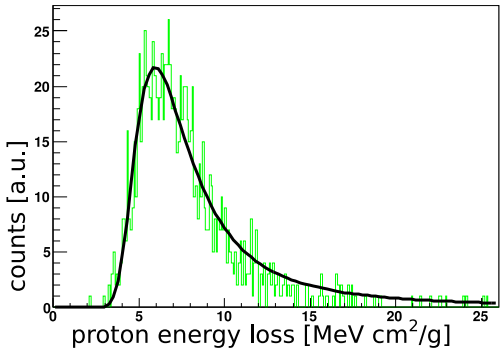

(b) Energy loss distribution for the 400 MeV/c – 440 MeV/c momentum region.

Figure 4.6: Momentum dependent proton dE/dx distributions from simulation with Landau function fit.

The most probable value and RMS is extracted from the fits for protons and pions as a function of momentum (black points with blue error bars) and are shown in Fig.4.7. A similar procedure was repeated for the simulation (black points with green error bars). As one can see, the obtained mean and RMS values agree with the simulated ones very well. The respective distributions for kaons were obtained from the simulations and are shown in Fig.4.7, too. As one can see, the discrimination of kaons from protons and pions

is possible only below momenta of 800 and 600 MeV/c, respectively.

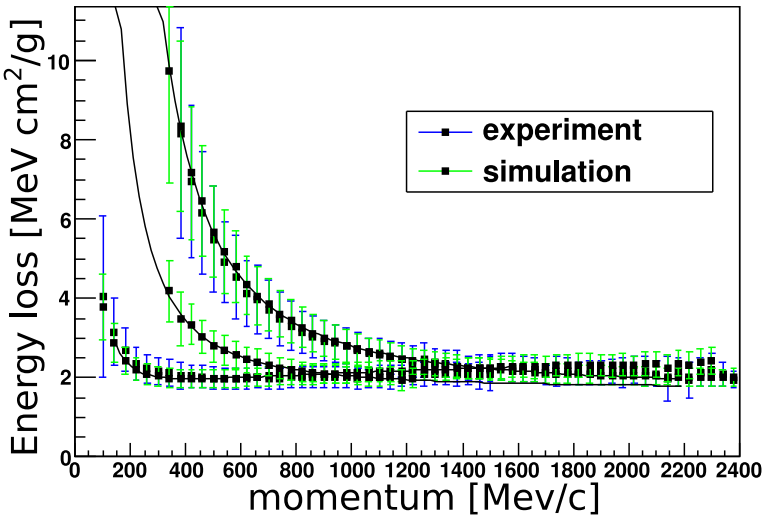

Figure 4.7: dE/dx distributions used for defining momentum dependent cuts.

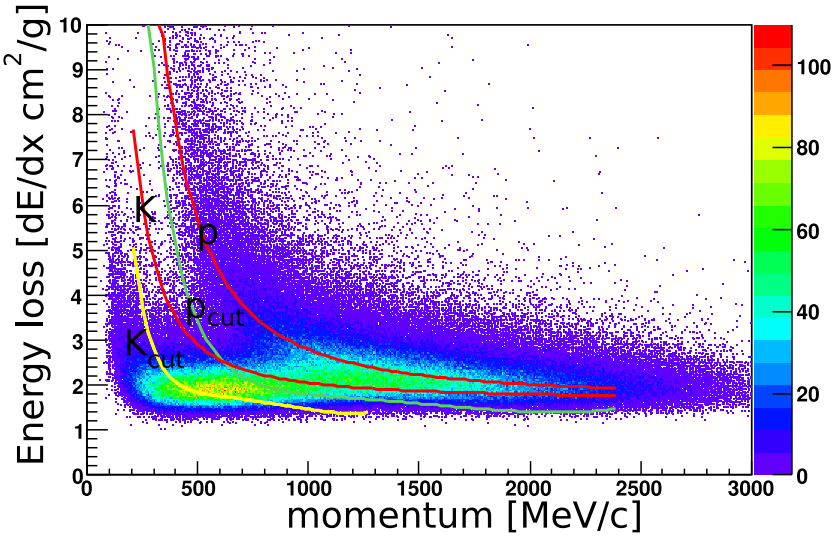

Figure 4.8: dE/dx cuts. Red lines are fitted polynomial functions to the most probable values of the dE/dx as a function of the momentum. The yellow line is a a cut for the kaons, green for the protons.

Since the dE/dx distributions are not symmetric, the conditions defined for the particle identification are defined in the following way:

$$K^{+/-} \text{ MDC } dE/dx > \text{most probable value} - 2.5RMS_{kaon}$$

$$p \text{ MDC } dE/dx > \text{most probable value} - 2.5RMS_{proton}$$

The graphical representation of these cuts imposed on the experimental distributions is shown in Fig. 4.8. The red lines describe the most probable dE/dx values for a given particle type. The green and yellow line represents the dE/dx cut used in the analysis, which separates respectively protons and kaons from the pions.

4.4 Particle identification

After applying the cuts described in the previous sections, the particles were qualified for a particular type - p, K^+, K^-. In some cases (for example 4 particles per event) there were more than one classified combination per event and one needed to determine the best pK^+K^- particle combination. In such case to identify the particles in the unique way, the MDC dE/dx measurements were used and a global event χ^2 is calculated:

$$\chi^2_{combination\ I,II,III} = \sum_{i=1} \frac{(dE/dx_{Ideal\ i} - dE/dx_{measured\ i})^2}{(dE/dx)^2_{resolution}}$$

The combination with the lowest χ^2 value is used to identify the particles. At this point, when checking the simulation data, in $\sim$ 99% of the events the particles were properly identified.

4.5 Missing Mass Cut

In the presented $pp\phi$ exclusive reaction channel it is only required to detect three particles. The kinematics of the fourth one (proton) can be obtained from the known momentum vectors of the beam, the target and the identified 3 particles (p, K^+, K^-).

Fig.4.9a shows the pK^+K^- missing mass distribution for the identified proton and kaon candidates. As one can see the background is very large and exceeds the signal visible as a small peak around the proton mass. The background originate mainly from misidentified pions from reactions of the type $pp\pi^+\pi^-\pi^0$, which has much larger cross

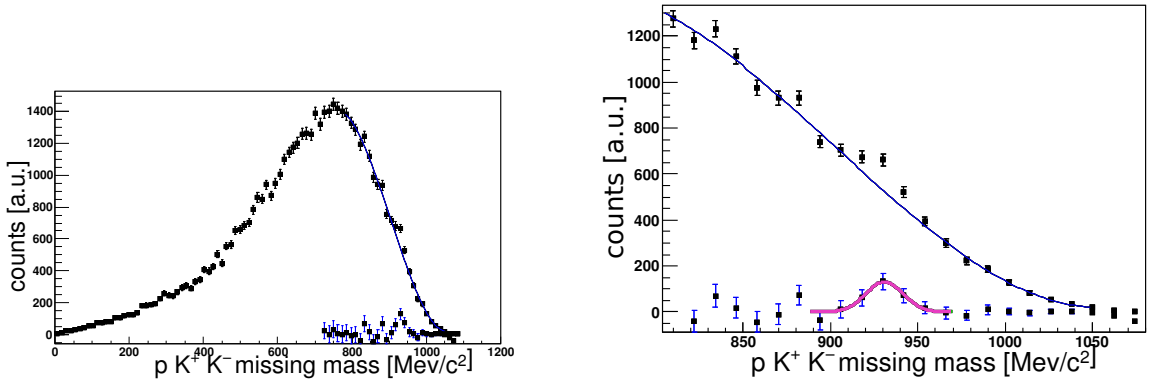

(a) Background fit with fourth order polynomial function (blue line) to extract the pK^+K^- missing mass signal.

(b) Zoom of experimental data for the pK^+K^- missing mass. To the experimental points a Gauss function is fitted (magenta line).

Figure 4.9: Missing mass cut

section (around 4 mb, to be compared with 1 μb for the ppK^+K^-). In the right panel of Fig.4.9 a zoom around the pK^+K^- missing mass peak is shown together with a Gauss function fit. Fig.4.9b shows, that the mean value of the experimental data points is shifted relative to the proton mass by 8 MeV/c^2 and it is located at 930.1 MeV/c^2 (instead of 938 MeV/c^2). This has recently been explained by a 1% uncertainty of the magnetic field value given by the current read-out, which corresponds to the absolute field value. A similar effect has also been observed for the other mesons (ω, K^0) and it is under investigation.

Following the obtained results, for the best signal to background ratio a cut for the ppK^+K^- selection has been defined in the pK^+K^- missing mass around the proton peak:

$$930 - 1.4\sigma < p \text{ missing mass } < 930 + 1.4\sigma$$

where σ amounts to $8.6 MeV/c^2$ for the experimental data and $6.5 MeV/c^2$ for the simulation. The number of the protons in the extracted peak ($1.4\sigma cut$) is 183 ± 15.9 (statistical error) and should be larger or at least equal to the number of extracted ϕ meson particles.

4.6 Vertex Cuts

The vertex cut is based on the trajectory information carried by two kaons. Based on this it is possible to extract the vertex position - marked with V in Fig.4.10a. The coordinates of this point and the distance (R in Fig.4.10b) to the actual beam position can be calculated. The position of the beam is extracted from all available experimental data for a different time periods of the experiment. This allows to compensate for any shifts caused by changes of the beam direction [75]. In Fig.4.10b the the x and y position from one day of data taking is presented.

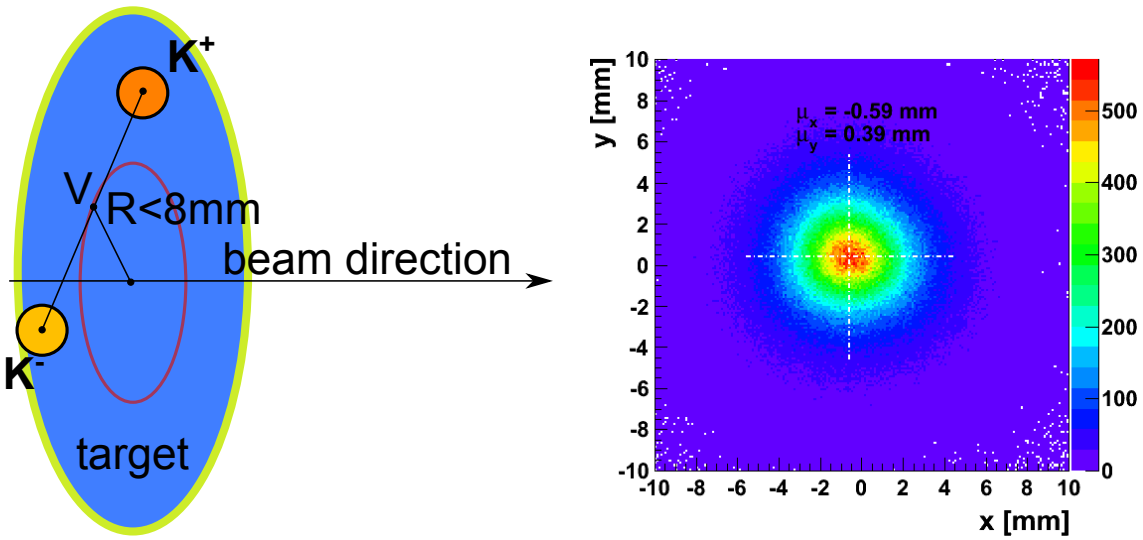

(a) Vertex (V) of K^+ and K^- in relation to the beam position (R). The blue area marks the hydrogen target position (scale is not preserved).

(b) X Y beam vertex position extracted from one day of the experimental data.

Figure 4.10: Vertex cut.

The geometrical cut is applied based on an assumption that for the kaons, which are the result of the ϕ meson decay, the vertex should be close to the actual beam position. The data from the experiment (black points with blue error bars Fig.4.11) and from simulation (green line Fig.4.11) is presented in logarithmic scale in Fig.4.11. The cut is represented by the red line. As one can see above 8 mm the experimental data are higher than the simulation (when the areas below the cut are in agreement). This indicates an admixture of uncorrelated events. Therefore, the events are accepted when the distance between the kaons vertex and the beam position is smaller than 8 mm.

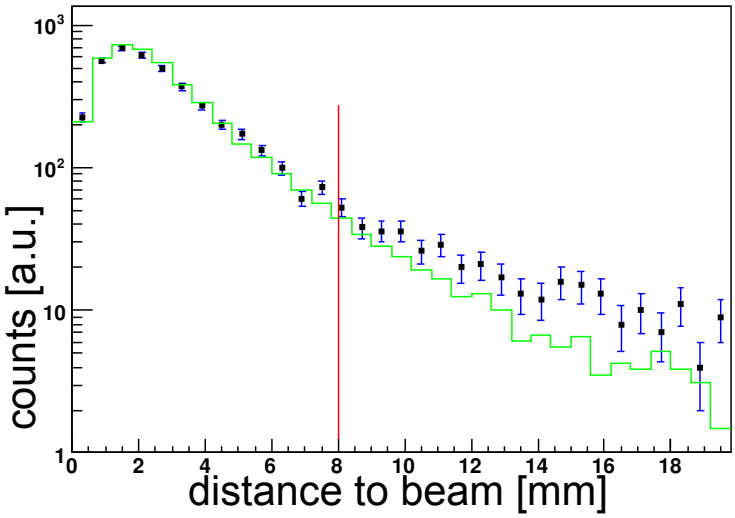

Figure 4.11: Distance of the kaons vertex to the beam position from the experimental data (black points with blue error bars) and simulated (green line). The red line represents upper limit (8 mm) of the distance between K^+ K^- vertex and beam position for the accepted events.

Chapter 5

ϕ Meson Yield Estimation

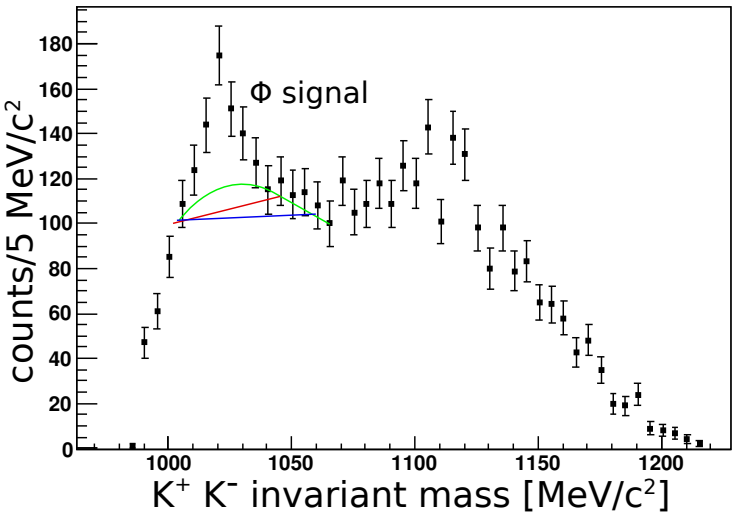

Figure 5.1: K^+ K^- invariant mass signal after all cuts described in the previous sections and particle identification. Different lines under the ϕ meson peak represent various fits for the background estimation. The proper background estimation is described in the next part of this chapter. Also the visible structure above 1100 MeV/c^2 is explained later on.

As a result of previously presented cuts applied to the data sample an experimental signal with ϕ meson peak, visible in Fig.5.1 at 1020 MeV/c^2 K^+K^- invariant mass, is obtained. To extract the ϕ meson yield it is necessary to estimate the shape of the background. In Fig.5.1 there is no clear indication how it should look like. Green, blue and red lines are examples of fits obtained with different background functions. Fitting the background shape with polynomial functions would lead to a large systematical error.

In order to avoid this and to estimate in a proper way the background under the ϕ signal the side band method is employed.

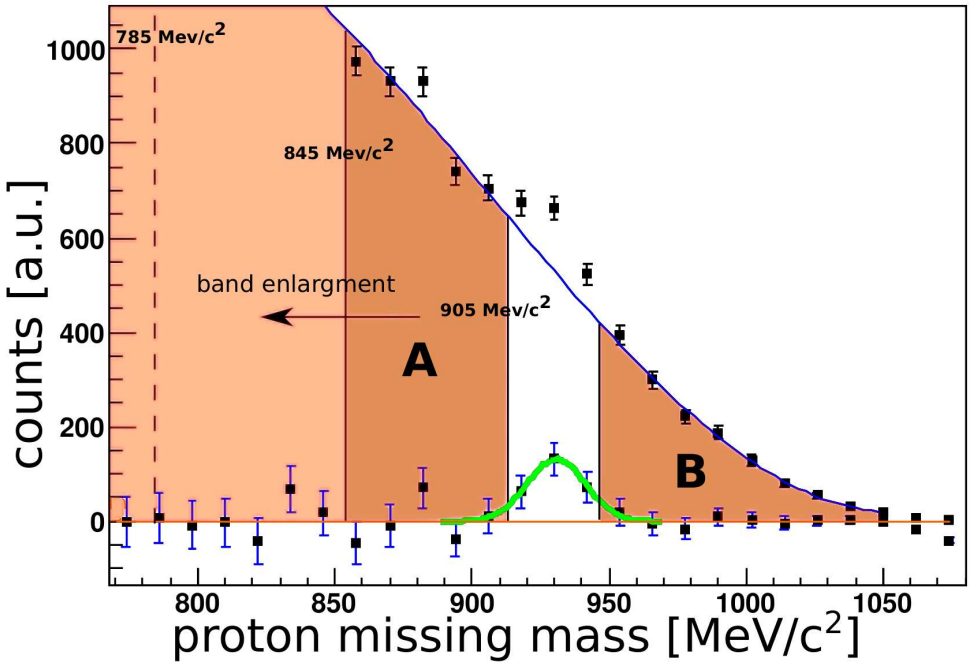

Figure 5.2: Side band method implementation for the background estimation. The plot shows the missing mass distribution and areas, from which the background is extracted (A and B). To check the stability of the extracted background the width of band A is changed from 60 MeV/c^2 to 360 MeV/c^2.

In the implementation of the side band analysis method, the events in the missing mass of pK^+K^- which are outside the proton mass were taken to simulate the behavior of the background (see Fig. 5.2 - A and B range) and normalized to the background area around the ϕ peak:

$$M_{inv\ K^+K^-} < 1000\ MeV/c^2 \text{ and}$$

$$1040 < M_{inv\ K^+K^-} < 1075\ MeV/c^2$$

The conditions for the side band widths are:

$$pK^+K^-_{missing\ mass} > 945\ MeV/c^2 \text{ and} \tag{5.1}$$

$$915\ MeV/c^2 - 60\ MeV/c^2 \cdot W < pK^+K^-_{missing\ mass} < 915\ MeV/c^2. \tag{5.2}$$

Where W is a parameter used to determine how accurate and stable is the background as a function of the width of left band (Fig.5.2 - area A). It was varied from 1 to 6 (60 MeV/c^2 to 360 MeV/c^2) and under such conditions it was found that the shape under the ϕ peak changes only slightly. The background obtained by this method with $W = 1$ is plotted as black points with red error bars in Fig.5.3 and, as one can see, it nicely describes the background behavior around the ϕ meson peak. By subtracting the background from the K^+ K^- invariant mass the ϕ meson signal is established.

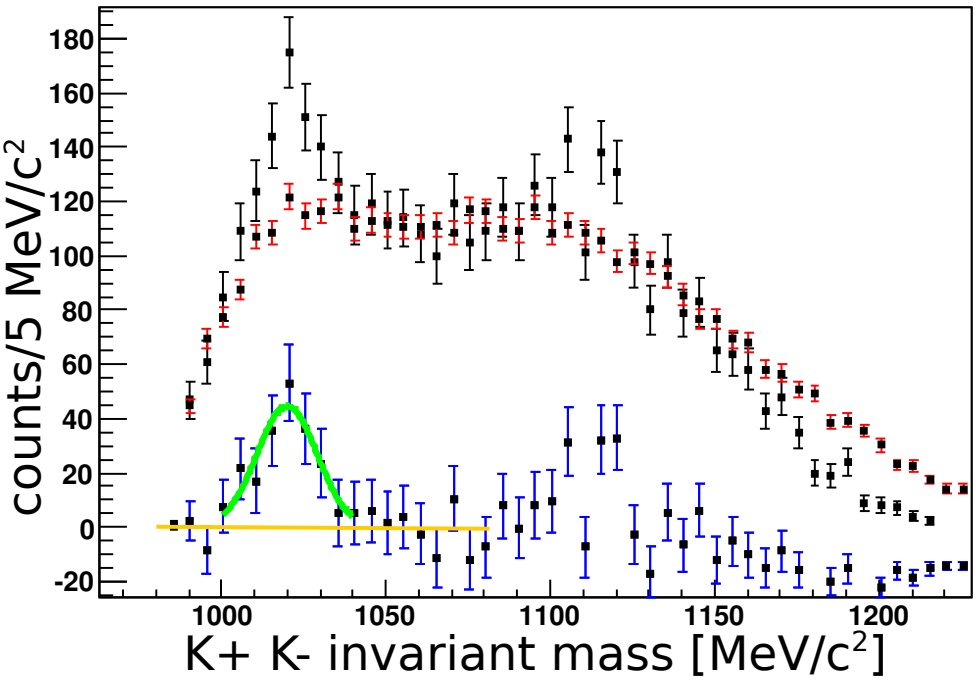

Figure 5.3: Experimental signal - black points, background estimated by the side band method (with $W = 1$)- red points with red error bars, extracted ϕ meson signal - black points with blue error bars(exp. signal minus background).

The mean position of the peak presented in Fig.5.3 is $\mu = 1020.5\ MeV/c^2 \pm 2\ MeV/c^2$ and the width $\sigma = 7.5\ MeV/c^2 \pm 2 MeV/c^2$. The derived ϕ yield equals to 183±35.2($stat.$)± 16.8($syst.1$). Where the first part of the error ($stat.$) is statistical and second part ($syst.1$) is systematical. It is calculated from the different background estimations under the ϕ peak. This is in agreement with the number of counts in the proton peak extracted from the pK^+K^- missing mass distribution, which equals to 190 ± 13.8 (stat.). In Tab.5.1 the number of counts in the proton peak extracted from the missing mass spectrum is

compared to the ϕ yield from K^+ K^- invariant mass. This is done for various widths of the missing mass cut, where the cut width is changed in terms of the RMS width. As one can see, both yields are consistent.

cut value $[RMS]$	$\frac{p_{yield}}{\phi_{yield}}$
2	1.05
1.9	1.07
1.8	1.02
1.7	1.06
1.6	1
1.5	1
1.4	1.04
1.3	0.97
1.2	0.92
1.1	0.94
1	1.03

Table 5.1: Comparison of ϕ yield with yield in the proton peak from the pK^+K- missing mass for different missing mass cuts.

Above 1100 MeV/c^2 in the invariant mass spectrum (see Fig.5.3) one can see another structure, which can not be described by the background created with side band method. The origin of this structure can be explained by simulation of the dominant background channel the $pp \rightarrow pp\pi^+\pi^-\pi^0$. In Fig.5.4 the green histogram represents K^+K^- invariant mass distribution obtained from misidentified pions originating from the $pp \rightarrow pp\pi^+\pi^-\pi^0$ reaction channel. Simulated events were treated in the same way as experimental data - the same cuts and particle identification as for ϕ meson exclusive channel analysis. In the same mass region as for the reconstructed K^+ K^- invariant mass (above 1100 MeV/c^2) a second structure appears. The blue line shows the invariant mass distribution for the misidentified pions but obtained with the side band method described above. As one can see the background obtained with the side band method describes the background shape around the ϕ meson mass region very well. On the other hand, like for the experimental K^+ K^- invariant mass, the structure above 1100 MeV/c^2 is not reproduce. Hence, one can conclude that the background estimation based on the side band technique is a good

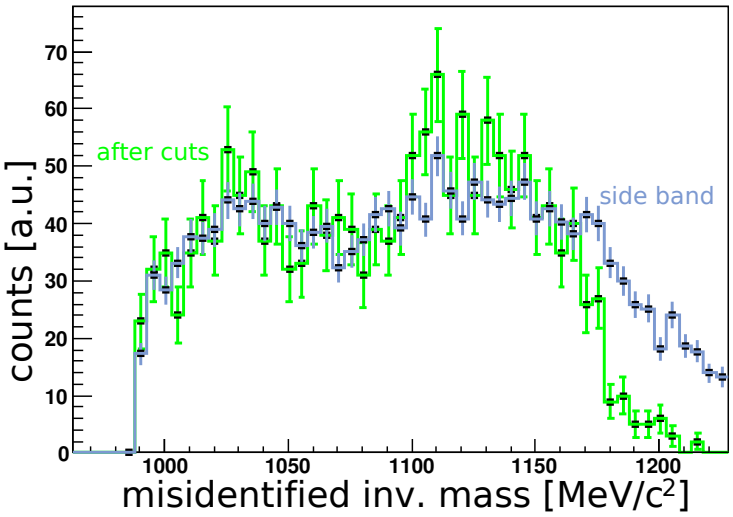

Figure 5.4: Green curve: misidentified K^+ K^- invariant mass from the $pp \to pp\pi^+\pi^-\pi^0$ reaction channel with visible structure above 1100 MeV/c^2. The blue line: data constructed like in the side band method. This indicates that the three pions channel is a source of this K^+ K^- invariant mass shape.

approach only for the $950 < M_{K^+K^-} < 1100 MeV/c^2$.

5.1 Estimation of Systematic Errors

As it was discussed in previous section, the systematic error was obtained by different background estimation. However, it is necessary to introduce an additional error due to the different cut effects on the simulated and experimental data. This impose an additional systematic error for the determination of the final ϕ meson exclusive production cross section. To estimate the cuts influence it is necessary to compare the simulation and experimental yields when varying these cuts. The cuts are changed in respect to the RMS values obtained on a given distributions (see section 4.2 and 4.5). The results of this investigations are presented in Tab.5.2.

A relative change is calculated by comparing the fraction of the ϕ meson yield from the simulation and experiment when cuts are open to 2RMS to the one when the cuts are changed:

$$RC = \frac{\phi_{sim.\ diff\ cuts}}{\phi_{exp.\ diff\ cuts}} \div \frac{\phi_{sim.\ 2\cdot\sigma\ cuts}}{\phi_{exp.\ 2\cdot\sigma\ cuts}} \tag{5.3}$$

cut type	cut value [σ]	Relative Change RC
K^+ mass	1.8	0.98
	1.6	1.05
K^- mass	1.8	1.02
	1.6	1.09
proton mass	1.8	1.04
	1.6	1.21
K^+K^-p missing mass	1.9	1.03
	1.8	0.98
	1.7	1.02
	1.6	0.97
	1.5	0.98
	1.4	1.03
	1.3	0.98
	1.2	0.93
	1.1	0.97
	1	1.08

Table 5.2: Comparison of simulated and experimental ϕ yields under different cuts conditions.

The estimated systematical error ($syst.2$) is on the level of 7% and can be quadratically added to the ϕ meson yield systematic error, finally $\phi_{yield} = 183 \pm 35.2(stat.) \pm 16.8(syst.1) \pm 12.8(syst.2)$.

Chapter 6

Comparison of Experimental and Simulated Data

In order to get the ϕ meson exclusive production cross section (see Chapter 7) corrections for the spectrometer acceptance and reconstruction efficiency losses must be applied. Respective correction factors can be obtained only by means of dedicated simulation. For the simulation a certain reaction model must be assumed. Therefore it is important to compare the experimental and simulation results inside the HADES acceptance. If the model describes the measured distribution, extrapolation to the full phase space is justified.

In the next subsections the angular (sec. 6.1), momentum of the ϕ meson (sec. 6.2) and mass distributions (section 6.3) of the kaons and protons are presented. The simulation is done as illustrated in the section 3.1. In the event generator used for the ϕ meson simulation a simple production model was assumed. An isotropic ϕ angular distribution in the Center of Mass (CM) frame and an uniform phase space population in the proton-meson Dalitz distribution were assumed.

In order to show the ϕ signal distributions it is necessary to extract the background for each of investigated distributions. To do so, the background subtraction must be applied. Two different techniques described in next sections were investigated.

6.1 Angular Distributions

In first step, angular distributions in the CM frame are analyzed. The proton distribution for the ppK^+K^- reaction (shown in the bottom panel Fig.6.1) is obtained as the difference between two distributions obtained for:

a) the events inside the window around the ϕ peak in the K^+K^- invariant mass distribution (Fig.6.1 upper panel - black symbols),

b) the events contained in the side bands (Fig. 5.2) with the normalization to the area below the ϕ peak (Fig.6.1 upper panel - black symbols with red error bars).

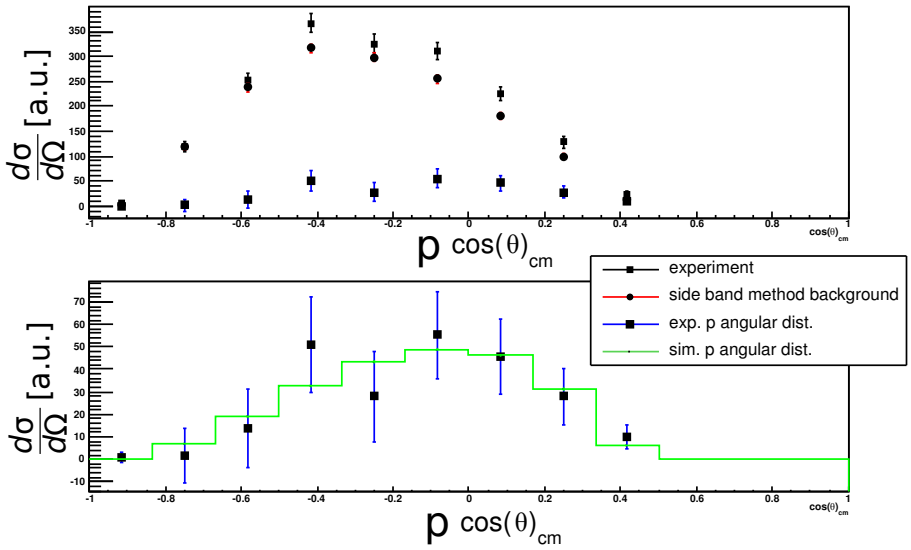

Figure 6.1: Angular distribution of the detected (black points with blue error bars) and simulated proton (green histogram) in the center of mass frame. Upper plot shows distributions for the events inside the window around ϕ peak (black points) and for the events inside the side bands (black points with red error bars). Signal (black points) is the difference. Bottom plot shows comparison of the signal to the simulation

Similar procedure has been applied to derive the ϕ angular distribution. The result is shown in Fig.6.2.

As one can see both distributions are in agreement in the shape with the simulation, which was normalized to the same area. Therefore the assumption of the isotropic angular distribution is fairly correct. This conclusion is consistent with the results obtained by

the DISTO experiment but the excess energy for the ϕ meson production was 80 MeV [76].

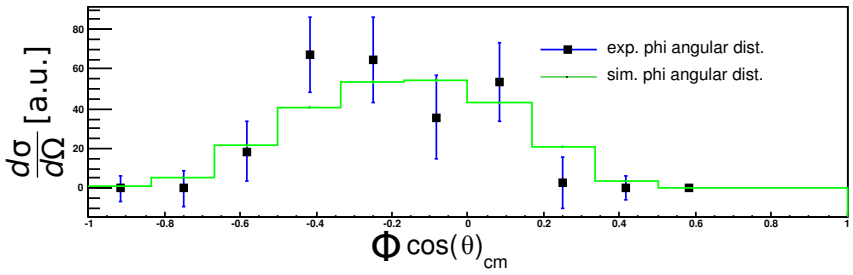

Figure 6.2: Angular distribution of the ϕ meson reconstructed from the experiment (black points with blue error bars) and simulated (green histogram) data in the center of the beam and target proton mass.

6.2 Momentum Distributions

In next step, the momentum distributions of the protons and ϕ meson are investigated. The distributions obtained from experiment and simulation are shown in Fig.6.4. In the right column the background was extracted with the side band method described above. In this case the simulated data and experimental one do not fully cover. In order to check the reason for this discrepancy the condition for the side band was changed to the following one:

$$M_{inv.\ K^+K^-} < 1000\ MeV/c^2 \text{ or } 1040\ MeV/c^2 < M_{inv.\ K^+K^-} < 1070\ MeV/c^2 \quad (6.1)$$

$$M_{missing\ mass} > 855\ MeV/c^2 \quad (6.2)$$

This ensures that the background distributions are created only from the events, which are in a direct neighborhood of the ϕ meson peak (see Fig.5.3). It is also similar to the area where the background extracted with the side band method for the K^+ K^- invariant mass fully covers experimental points (see Fig.5.3). This also confirms the observation made with the simulation presented in Fig.5.4 where one see that the side band background describes the distribution of missidentified pions in the K^+K^- invariant mass only in the mass region given by equation 6.1.

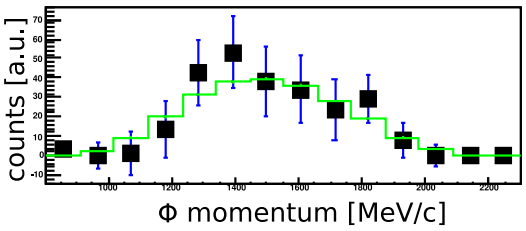

(a) ϕ meson momentum distribution.

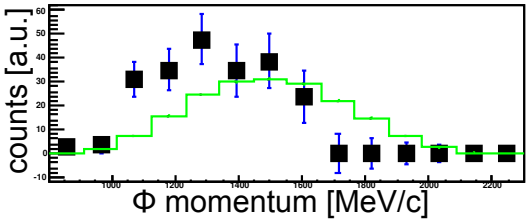

(b) ϕ meson momentum distribution.

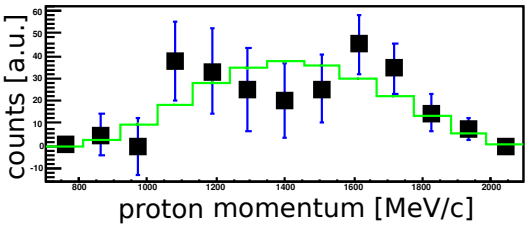

(c) Detected proton momentum distribution.

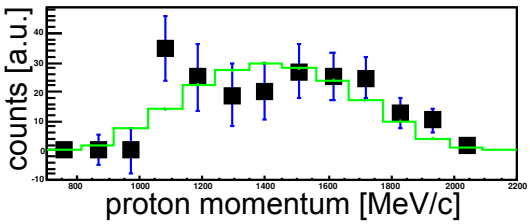

(d) Detected proton momentum distribution.

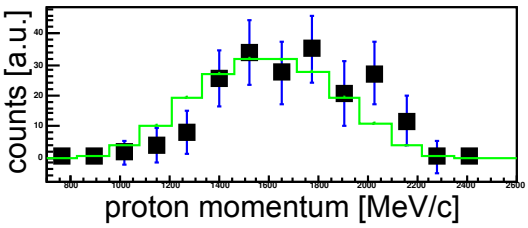

(e) Missing proton momentum distribution.

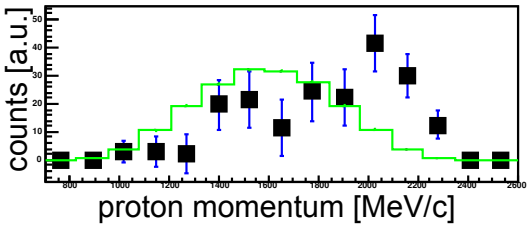

(f) Missing proton momentum distribution.

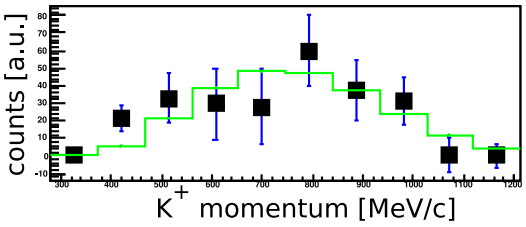

(g) K^+ momentum distribution.

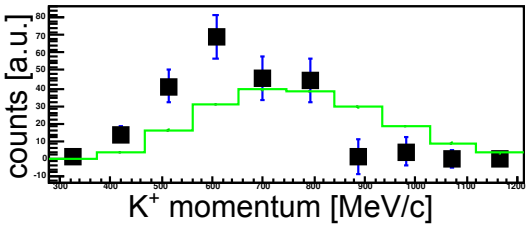

(h) K^+ momentum distribution.

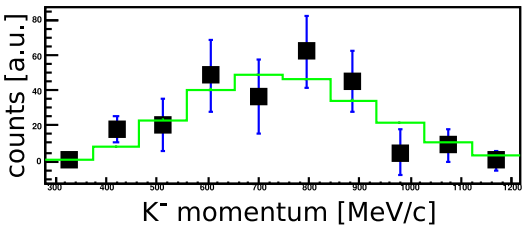

(i) K^- momentum distribution.

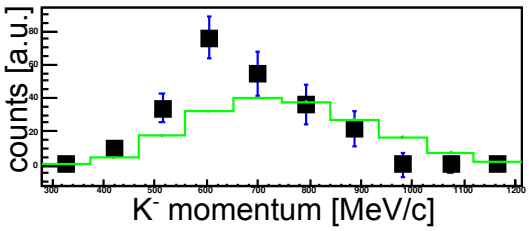

(j) K^- momentum distribution.

Figure 6.3: Comparison of the simulated (green histograms) and experiment (black points with blue error bars) momentum distributions. The left column represents the background extracted with conditions described in equation 5.1, the right corresponds to the method used for ϕ meson K^+ K^- invariant mass background estimation. As one can see the first method describes the channel reaction momentum distribution in a better way.

With such conditions the simulated and the experimental data are found to be in a good agreement. One should mention that the ϕ meson and proton angular distribution presented above does not change when applying this modified condition. Therefore the conclusion about the agreement between the simulation and experimental data holds for all presented differential distributions.

6.3 Mass Distributions

As the last step, in Fig 6.4 we show comparison of the proton, and kaon mass distributions for the ϕ signal extracted with the side band method to the simulated ones. As once can see, obtained mass distributions agrees very well with the expected ones and confirms, in particular for the kaon masses, that the observed signal originates from the ppK^+K^- channel. Fig.6.4d shows p ϕ invariant mass distribution, which also agrees with the simulation confirming assumed phase uniform distribution.

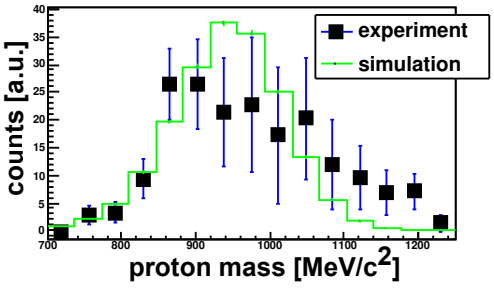

(a) Detected proton mass distribution.

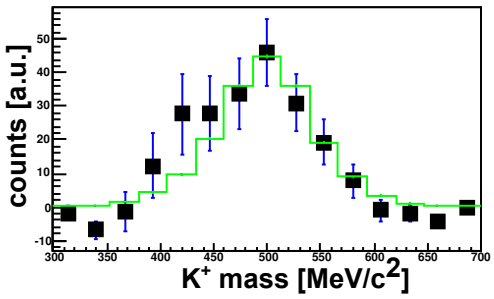

(b) K^+ mass distribution.

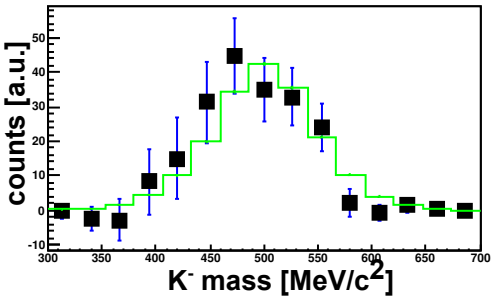

(c) K^- mass distribution.

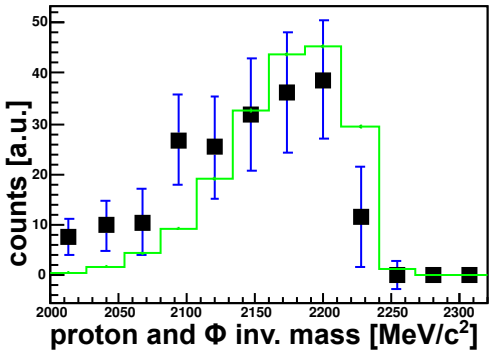

(d) p and ϕ invariant mass distribution.

Figure 6.4: Comparison between the simulation (green histogram) and experiment (black points with blue error bars) data of mass distributions for a different particles. As one can see in all cases the data is in agreement (within 2σ).

The obtained results also ensure that the model used for the ϕ meson production agrees reasonable with the measured distributions and can be used for calculation of the acceptance and efficiency correction factor. The correction factor has been obtained with the PLUTO and Geant simulation programs and full reconstruction scheme will be presented in the next section (see chapter 7).

Chapter 7

ϕ Production Cross Section

To calculate the exclusive ϕ meson production cross section following formula has been used:

$$\sigma^{\phi}_{4\pi} = N_{\phi\ 4\pi}\frac{\sigma_{el.4\pi}}{N_{el.4\pi}} = N_{\phi\ 4\pi}\frac{\sigma_{el.acc}}{N_{el.acc}} \text{ ,where:}$$

$N_{\phi\ 4\pi}$ – Number of events corresponding to ϕ meson production in $p+p$ reactions in the full phase space,

$\sigma_{el.4\pi}$ – cross section for the elastic scattering,

$N_{el.4\pi}$ – number of proton-proton elastic scattering events,

$\sigma_{el.acc}$ – cross section for the elastic scattering inside the HADES acceptance,

$N_{el.acc}$ – number of events with the elastic scattering reconstructed inside the HADES acceptance.

In order to obtain the acceptance and reconstruction corrected number of counts for the ϕ meson ($N_{\phi\ 4\pi}$) one has to consider:

- acceptance and efficiency correction factor of the HADES spectrometer for the $pp \rightarrow pp\phi \rightarrow ppK^+K^-$ exclusive channel - $AccEff$,
- branching ratio br for the $\phi \rightarrow K^+K^-$ decay - $BR = 49.2^{+0.6}_{-0.7}$[12],
- downscaling factor of the LVL1 trigger - dsc,

The acceptance and efficiency corrections are extracted from the $pp \rightarrow pp\phi \rightarrow ppK^+K^-$ exclusive channel simulation. This is done by calculation of the ratio of the number of simulated events to the number of reconstructed events after all cuts described in chapter 4. The obtained correction factor is used to multiply obtained ϕ meson yield. The downscaling factor is related to the LVL1 events, which were stored independently from the LVL2 trigger decision, and it equals 2.87. Having all these factors one is able to determine the $N_{\phi\ 4\pi}$:

$$N_{\phi\ 4\pi} = \frac{AccEff \cdot dsc}{br} \phi_{experimental\ yield} \tag{7.1}$$

In the next section the elastic scattering cross section correction factor $\sigma_{el.acc}/N_{el.acc}$ is presented.

7.1 $p\ p$ Elastic Scattering Cross Section - Normalization Factor

To obtain the $N_{el.acc}$ it is necessary to select experimental events containing pp elastic scattering. For this purpose during the experiment the dedicated M2 trigger was used. The elastic scattering reaction can be fully described by two independent variables [79]. These variables are a laboratory azimuthal angle (Φ) and a laboratory polar angle (Θ). Using these variables one can derive the following equation for the elastic proton-proton events :

$$\mid \Phi_1 - \Phi_2 \mid \ = \ \pi \tag{7.2}$$

$$cot\Theta_1 \cdot cot\Theta_2 \ = \ \gamma_{cm} \tag{7.3}$$

where, the γ_{cm} is the Lorentz factor of the CM system in relation to the laboratory system. It is defined as:

$$\gamma_{cm} = \sqrt{\frac{E_{beamproton} + m_{proton}}{2m_{proton}}}$$

After applying a two-dimensional cut around the expected values derived from the

Eq. 7.2-7.3 a prominent peak is visible in Fig.7.1 and one can uniquely identify elastic proton-proton scattering events.

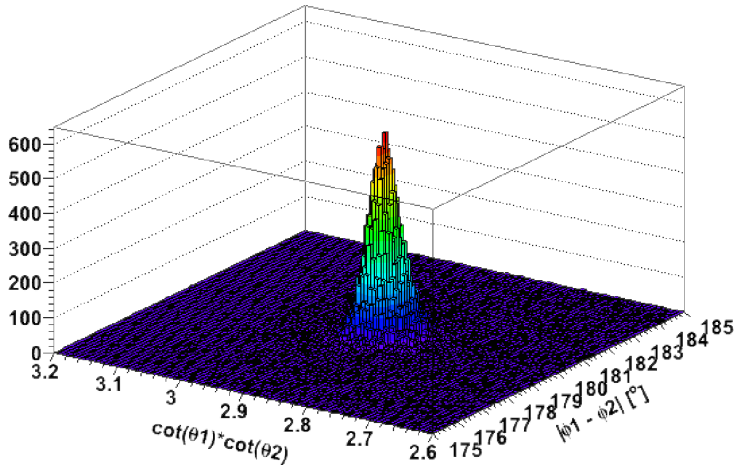

Figure 7.1: Angular distribution of the scattered protons in two dimensional representation of $\mid \Phi_1 - \Phi_2 \mid$ versus γ_{cm}. The peak originates from the pp elastic scattering.

However, integrating the visible signal does not deliver $N_{el.acc}$,yet because it is necessary to correct this number for the reconstruction efficiency. This is done with usage of simulation chain presented in section 3.1. The results of this analysis are presented in Fig.7.2. The ratio between the reconstructed number of the elastic events and the generated with PLUTO (within the HADES acceptance) gives the HADES efficiency for the *pp* elastic scattering reaction channel [77].

As one can see in Fig.7.3 the PLUTO event generator (Fig.7.3 solid black line) is not able to describe properly the elastic scattering cross section at beam momentum of 4.34 GeV/c, which corresponds to 3.5 GeV beam kinetic energy. Therefore, when determining the $\sigma_{el.acc}$ it is necessary to rely on the experimental data derived by the [78] at beam momentum 4 GeV/c (Fig.7.3 green points) and 4.5 GeV/c (Fig.7.3 gray points). The mean value (Fig.7.3 blue points) of these cross sections is taken as an approximation to the $\sigma_{el.acc}$ at 4.34 GeV/c beam momentum.

Finally, the correction factor $\frac{\sigma_{el.acc}}{N_{el.acc}} = 267 \cdot 10^8 \pm 2\%(stat.) \pm 7\%(syst.)$ [77].

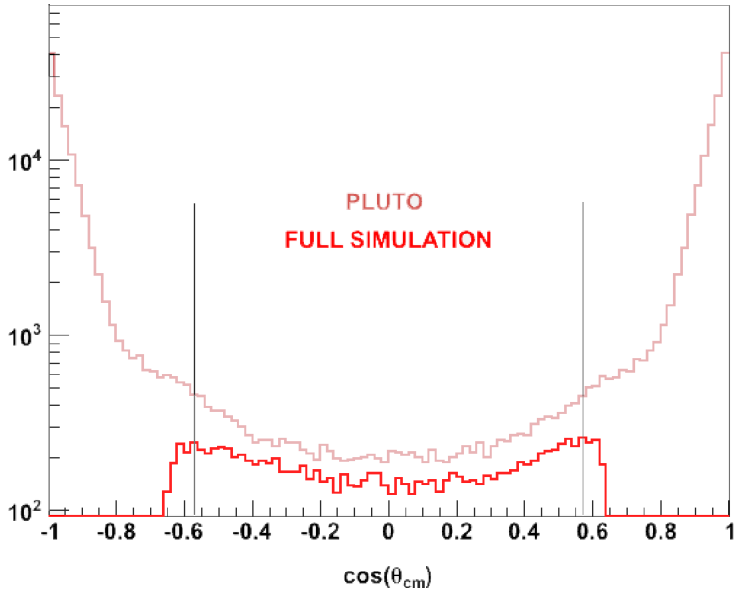

Figure 7.2: Comparison of the polar angle distribution simulated with PLUTO (light red line) and reconstructed (dark red line) pp elastic pairs.

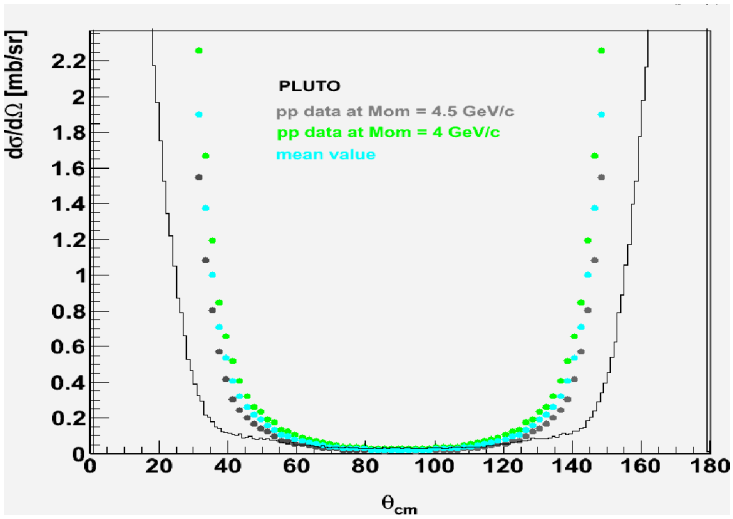

Figure 7.3: Differential elastic cross sections. Green and gray measurements [78] are used to estimate $\sigma_{el.acc}$ at 3.5 GeV beam kinetic energy (blue points).

7.2 Production Cross Section for $pp \rightarrow pp\phi$ at 3.5 GeV

With the correction factors described in the previous sections the $\sigma_{\phi}^{4\pi}$ exclusive production cross section can be calculated and it equals:

$$\sigma_{\phi}^{4\pi} = 1.05[\mu b] \pm 0.2[\mu b](stat.) \pm 0.13[\mu b](syst.) \tag{7.4}$$

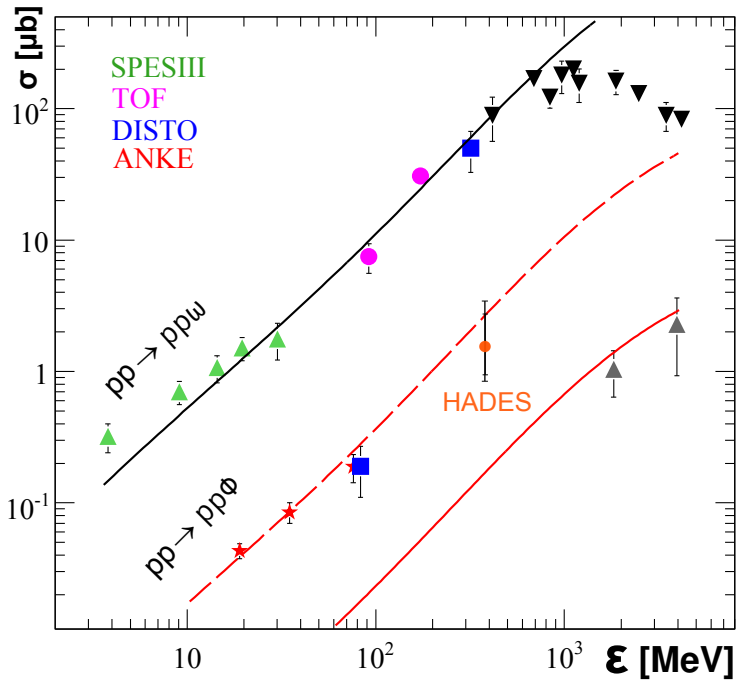

Figure 7.4: Exclusive ω and ϕ production cross section in pp reactions [80]. HADES result at 3.5 GeV kinetic energy is placed among already existing data points. The three lines represents a three body phase space for the production as a function of the energy normalized to the ω cross section at high energy (black line), ϕ meson at low energy (red dashed line) and ϕ in high energy region (red line) cross sections. Obtained result at 280 MeV excess energy for the ϕ meson production is in-line with the data from ANKE and DISTO experiments.

Fig.7.4 shows the world data on the ϕ and ω meson production cross sections in pp reactions as a function of the excess energy [42] [43] [81] [82] [83] [84] [85]. The three lines represents a dependence of three body phase space as a function of the excess energy where the final state proton-proton interaction effect is taken into account as well. This is equivalent to the assumption of a constant matrix element for the meson productions and production governed by the phase space only. The black line is normalized to the ω production cross section at high energy. For the ϕ meson two lines are presented, which differ by selected region of normalization: red dashed line shows result with normalization close to the production threshold while the solid presents result for the normalization fixed at high energy region. For the beam energy studied in this thesis the excess energy

for the ϕ meson production equals 280 MeV. In Fig.7.4 HADES data for exclusive ϕ meson production cross section is shown with orange circle. The achieved result is in-line with the results accomplished by ANKE and DISTO experiments close to the ϕ meson threshold production.

In HADES experiment the ω meson cross section was obtained as well. Fig.7.5 shows the ω meson peak in the proton-proton missing mass distribution extracted from the analysis of $pp \rightarrow \omega pp \rightarrow pp\pi^+\pi^-\pi^0$ reaction channel [71]. The ω meson cross section production was estimated to be $106.5 \pm 0.9(stat.) \pm 7.9(syst.)[\mu b]$. It is necessary to underline that at this kinetic energy the angular distributions measured for the ω meson in the CM frame are only slightly anisotropic in contrast to the results obtained at lower energies where strong anisotropy was observed [81]. This can indicate different production processes for the ϕ and ω mesons close to the production threshold.

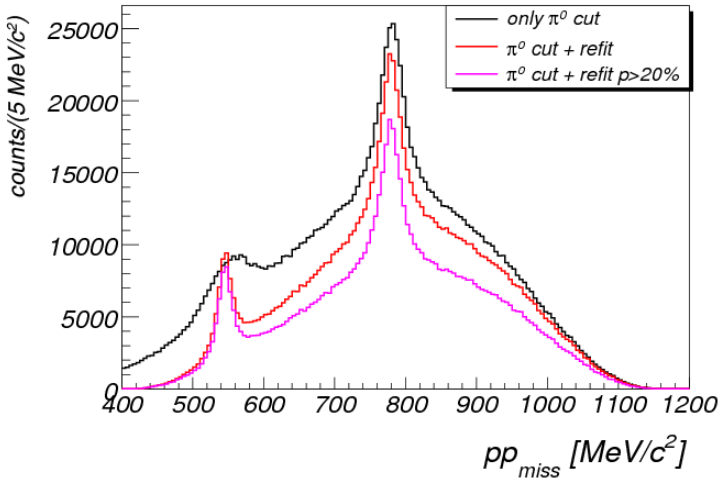

Figure 7.5: ω meson peak at 782 MeV/c^2 extracted from $pp \rightarrow \omega pp \rightarrow pp\pi^+\pi^-\pi^0$ reaction channel with HADES [71]

Based on these result the ϕ to ω production cross section ratio $R_{\phi/\omega}$ in pp reaction at 3.5 GeV kinetic energy can be calculated and amounts to:

$$R_{\phi/\omega} = 0.0099 \pm 0.0018(stat.) \pm 0.0012(syst.)$$

In Fig.7.6 this ratio is shown together with already existing results from $N-N$ (red points), $\pi - N$ (pink points) and $Ar + KCl$ (HADES-black point) collisions as a function

of excess energy for the ϕ meson production in elementary collisions. The excess energy for the heavy ion collisions is calculated assuming $N-N$ reactions of the same nominal kinetic beam energy. It leads to a negative value indicating subthreshold production which can proceed through secondary processes or/and direct $N-N$ reactions utilizing nucleons with large fermi momentum inside colliding nuclei. As already discussed in the introduction, the ratio observed in heavy ion reactions is larger at least by one order of magnitude as compared to the $N-N$ reactions, even the one observed at much higher energy of 3.5 GeV obtained in this work (green point). This might indicate that indeed other reaction mechanism is responsible for the ϕ meson production in heavy ion reactions. Among many possible reactions channels, secondary pion-nucleon collisions seems to be an obvious candidate. However, also for this reaction channel observed $R_{\phi/\omega}$ is larger, if one take into account that secondary pions are produced with low energies.

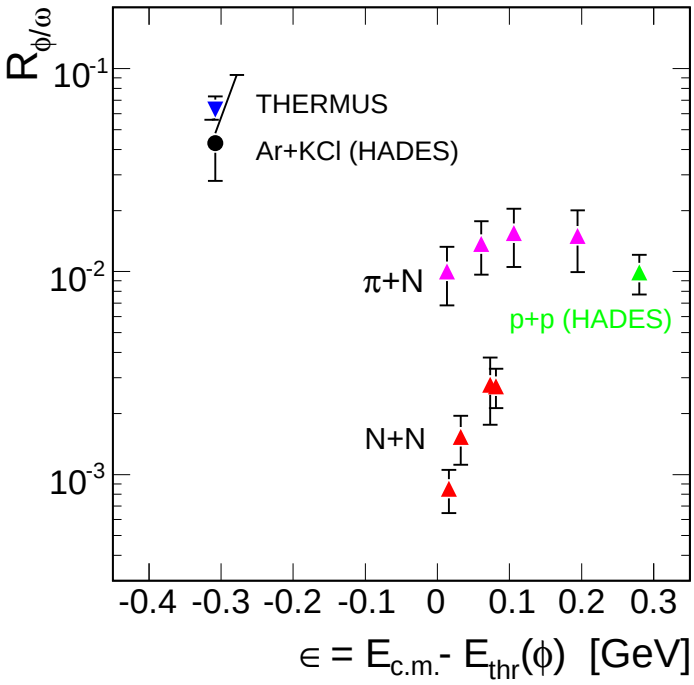

Figure 7.6: Ratio of ϕ to ω meson production cross sections at different ϕ excess energy and reaction types. Among other results there are results originating from the HADES experiment: in the region of ϕ meson sub-threshold production with $Ar + KCl$ reaction (black point) and from pp reaction at 3.5 GeV kinetic energy (green point)

It is also interesting to compare obtained $R_{\phi/\omega}$ (green point) to the one for the πN reactions at high energy. Both results are similar and are factor $\sim$ 2-3 above predictions given by the OZI rule ($4.2 \times 10^{-}3$). For the latter one, phase space factor f in equation 1.1 can be neglected due to sufficiently high energy above the production threshold what is reflected by almost constant $R_{\phi/\omega}$ value for the $\pi - N$ reactions. This excess above naive OZI rule predictions is clearly lower as compared to the one measured close to the production threshold in $N - N$ reactions ($\sim$ 7-8 [42], [43]).

Chapter 8

Conclusions and Outlook

The experimental results presented in this work, despite the low statistics, allows to estimate the ϕ meson exclusive production cross section $\sigma_{\phi}^{4\pi} = 1.05[\mu b] \pm 0.2[\mu b](stat.) \pm 0.13[\mu b](syst.)$. The agreement between simulation, where isotropic angular distribution in the CM frame and an uniform phase space population in the proton-meson Dalitz distribution are implemented, is observed. This agreement confirms that extracted in this work production cross section for the ϕ meson production (in context of acceptance and efficiency corrections) are reliable. From the same experimental data, but other analysis, the ω meson exclusive cross section production was acquired. Therefore the direct comparison between these two cross sections is possible and results in $R_{\phi/\omega} = 0.0099 \pm 0.0018(stat.) \pm 0.0012(syst.)$. The extracted data points are supplementary to the data of the ϕ to ω ratio in $Ar + KCl$ collisions at 1.756 $AGeV$ - measured by HADES and other low-energy $N - N$ data. In order to complete the picture on the $R_{\phi/\omega}$ excess seen in the heavy ion collisions new data from $p - A$ reaction channel at the same energy regime are required. The HADES collaboration measured $p + Nb$ system at $3.5AGeV$. The data analysis is currently in progress and its results will complete the picture of ϕ and ω meson production at this range of the kinetic energy.

Part II

Chapter 9

Upgrade of HADES Data Acquisition System

In the near future the measurements of the HADES spectrometer will be performed at a SIS-100, of the upcoming FAIR [86] accelerator complex at GSI. After this, following years the HADES collaboration will continue its experimental program up to the kinetic beam energies per nucleon of 8 GeV. Also during experiments at SIS-18 with a heavy ion collisions (like Au+Au) with a high charged particle multiplicity, the volume of the data will exceed this for what the system was prepared. It will reach 400 MB/s for the whole detector system with accepted LVL1 trigger rate of 20 kHz and 100 kHz in peak. The above was the reason for an upgrade of the HADES detector and its trigger and readout systems [87].

9.1 Trigger Readout Board : TRBv2

To build this new system it was necessary to take a decision what should be a structure of it and answer the questions - how the new readout electronics for each detector, what kind of the media for the data transfer, protocols, central trigger system and event builder will looks like. The whole approach was constructed on an idea of one platform for all subsystems. Adapting the "one platform" concept, the TRBv2 (Trigger and Readout Board version 2) was built [88].

To accomplish the above requirements this board consists of:

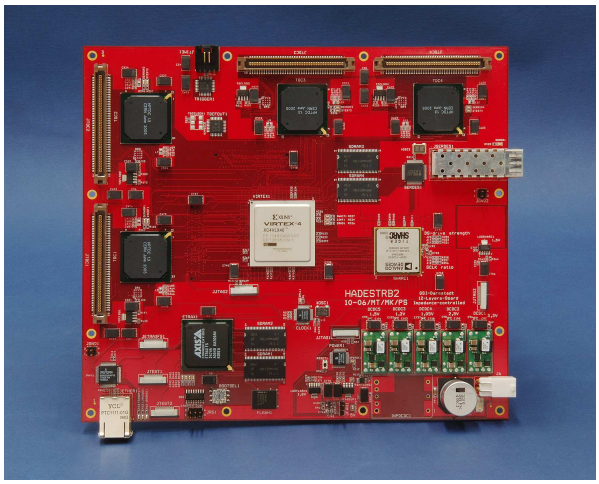

(a) TRBv2 board top view. Equipped with 128 time to digital converter channels, Virtex 4 FPAG, ETRAX-FS multi-processor, optical link, DSP, power supply, Ethernet connection.

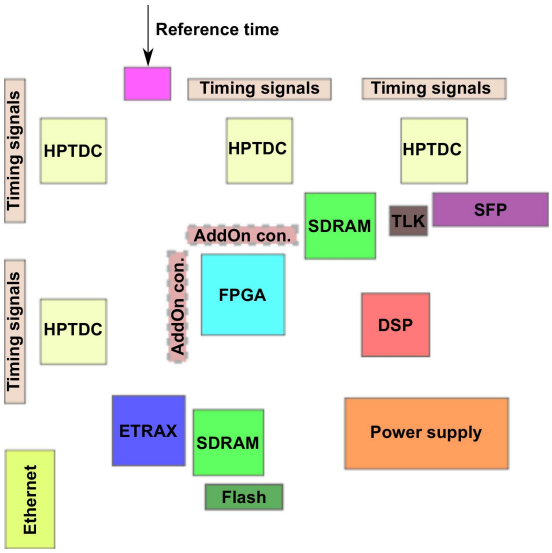

(b) Main components of the TRBv2. Dashed line for the connector placed in the back of the board.

Figure 9.1: TRBv2.

- four 32 channel Time to Digital Converter chips (HPTDCs),
- FPGA Virtex4 LX40 - it manages all the data flow on the board and it is connected to all main components on the board,
- ETRAX-FS multi-processor [91] - it is used for the DAQ and slow-control functionality. The processor runs a standard Linux 2.6 kernel in the 128 MBytes of memory and it is directly connected to the 100 $Mbit/s$ Ethernet. The integrated three co-processors (each 200 MHz) allow a high I/O bandwidth without the main CPU intervention,
- flash, where the ETRAX-FS processor boots from,
- optical link (2.5 Gb/s) - the FPGA sends data with the help of a TLK2501 Texas Instrument device [92] to the optical SFP (Small form-factor pluggable transceiver),
- Tiger-Shark DSP [93](600 MHz) - it can be used for the prepossessing of the data,
- AddOn connector - is a very high data-rate digital interface connector, which allows

to connect add-on (AddOn) boards. This can expand the field of possible applications by providing additional front-end electronics, computational power (other FPGAs and DSPs) or particular interfaces for the given detector subsystems. The pins of the AddOn connector are linked to the Virtex 4, Etrax-FS and also to the power supply of $+5\ V$,

- two 1 Gb SDRAM memory banks, connected to the ETRAX-FS and to the FPGA,
- 48 V galvanically isolated power supply.

The means for programming the HPTDC ASIC are generally the same as in the TRBv1 (see appendix 10) but with some differences of the board architecture. First of all, the HPTDCs are in one JTAG chain and the access to the JTAG lines is through the FPGA registers. Additionally, the user has an easy-to-use configuration file. Using the existing Perl script it is possible to create the TDC configuration files, which are written automatically in the STAPL language. Next the user can use the Jam Player and load all required setting to the TDCs. Also with the JTAG interface the Virtex FPGA, board clock manager and chips on the AddOn boards can be programmed.

For the usage of the TRBv2 several scenarios were necessary to apply:

- stand alone TDC readout board,
- independent from the HADES DAQ system setup (section 9.2),
- temporary Central Trigger System - CTS during 2010 HADES beam tests (together with General Purpose AddOn used for converting the signals standards e.g. from TTL to LVDS),
- first platform for the readout tests of the Shower and MDC AddOn boards (see section 9.5 and 9.6),
- integrated with the current HADES DAQ and trigger system as a TDC readout board (RPC, TOF, START, VETO, Forward Wall detectors),

In the stand alone mode the system is started with the rising edge of the reference time. The reference time is split to five signals. Four of them are connected to the 32nd

channel of HPTDCs to synchronize the TDCs locally and in a bigger system with other data coming from the other readout boards. The fifth reference time initiates the readout on the FPGA. The data taking scheme from the HPTDCs is just the same as in the case of the TRBv1 (see appendix 10). When the whole event is collected in the Virtex FIFO, it is transported via port $B(15:0)$ and $C(15:0)$ of the ETRAX-FS interface, by using a customized protocol, to its internal memory.

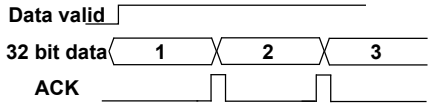

Figure 9.2: Data transfer protocol between FPGA and ETRAX-FS.

As it can be seen in Fig. 9.2, the FPGA signalize on port B pin 16 ($PB16$ - DATA VALID, Fig. 9.2) that there is a new data on the bus and if the ETRAX-FS is not busy, it confirms ($PB17$ - ACK, Fig. 9.2) that the data was written to its internal memory. After this, transmission of next word can be executed.

This also can be done with using the DMA architecture implemented in I/O processors of the ETRAX-FS (see Fig.9.3). In this situation, the FPGA sends the data in packets. Each consist of 15 data words - this is caused by input DMA FIFO size, which is only 16 words deep. When the data transfer is started, the ETRAX-FS I/O processor rises the busy signal immediately.

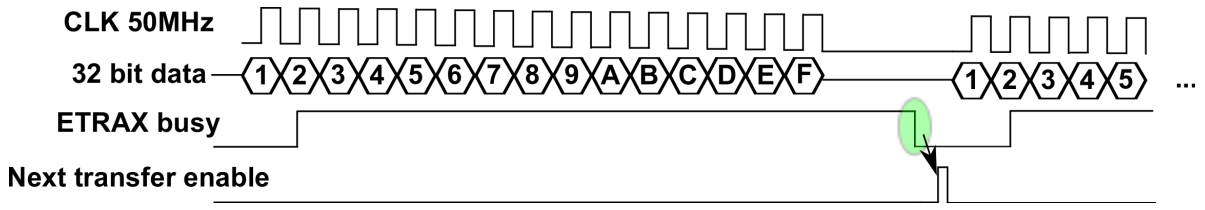

Figure 9.3: Data transfer protocol between FPGA and ETRAX-FS with DMA usage.

The algorithm prevents in this way situation in which the Linux processor indicates with unacceptable delay that it is busy meanwhile the FPGA sends a new event. This can happen when ETRAX-FS can not transfer the data via the 100 $Mbit$ Ethernet to the Event Builder or it can not copy the data from the DMA FIFO to the already filled up internal memory buffer. In this case a communication between the I/O and main processor

is needed, which can take not fixed time. If this is not the case, the busy is released and next data packet can be sent.

Table 9.1: Data transfer in the DMA mode with different data load.

32 bit words per event	LVL1 frequency [kHz]	Speed [MB/s]
14	124	11
22	82	9.2
38	44	8.5
64	27	8.1
110	18	7.9
170	10.5	7.8
640	3	7.7

More details about the implementation of the algorithms in the ETRAX-FS processor and the I/O co-processors can be found in [94].

As it was mentioned before, it is required to have access to the internal registers of the FPGA e.g. setting the delay between the reference time and trigger sent from the FPGA to the TDCs. For such situation a read/write protocol was developed. Since there are 36 lines between the FPGA and the ETRAX-FS and 34 already are occupied by the data transfer, the protocol had to be implemented on the remaining 2 lines - $PC17:16$ (see Fig. 9.4).

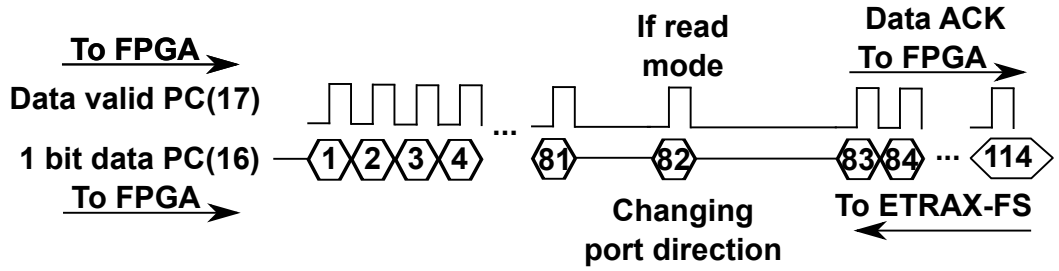

Figure 9.4: Data transfer protocol to read/write registers from/to the FPGA and also from/to other devices.

Line $PC(17)$ is used to inform the FPGA that a new bit of the data transfer ($PC16$) is on available. In the first 80 bits there is (see Fig.9.4):

- bits 3 : 0 indicate, from which device user wants to read/write. It can be directly the FPGA or via specially adapted interfaces: DSP, SDRAM or memory block inside the SFP,
- 15 - mode the r/w access, if bit 15 = 1 then this is read mode otherwise write,
- 47 : 16 - address to read/write,
- 79 : 48 - data to write, sent even in the read mode.

If this is the read mode, after 80 bits of the data transfer, the 81st pulse ($PC(17)$) from the ETRAX confirms, that the line $PC(16)$ changed its direction and the FPGA can start to send data. The described stand alone mode is useful for small applications and test setups. This mode is also used to test a newly produced TRBv2 with a specially designed AddOn Tester (see Fig. 9.5a). This board consist of one Lattice ECP2M FPGA, which can be accessed from the ETRAX-FS on the TRBv2 (the same read/write protocol as between the VIRTEX FPGA and ETRAX-FS (see Fig. 9.4). The TRBv2 and the Tester AddOn are attached to each other via the AddOn connector. The TRBv2 is not visible on this figure - it is located under the Tester AddOn board. The Tester AddOn has sixteen clock drivers [95]. One clock driver accepts one differential LVDS signal from the Lattice FPGA and splits it to 8 differential outputs with additive input to output jitter less than 1 ps (see Fig. 9.5b).

With the AddOn Tester board it is possible to check if all the measurement channels are working properly in terms of a time resolution. During such test the reference time is sent to the TRBv2 and also per one event two out of eight signals are sent to the individual HPTDC channels. The time difference between such signals has to be constant and any deviation of the time difference measurements shows the time resolution of the HPTDC together with TRBv2 PCB (Printed Circuit Board) layout, connections and cables.

Fig.9.6 presents measurements for the High Resolution mode of the HPTDC (96 ps HPTDC bin size). The mean value of two channels resolution is on the level of $RMS = 0.426 \times \text{bin size} = 40.9\ ps$.

For the START and VETO detector there is a necessity to accomplish much better results. This can be done in Very High Resolution mode (24 ps HPTDC bin size). In this

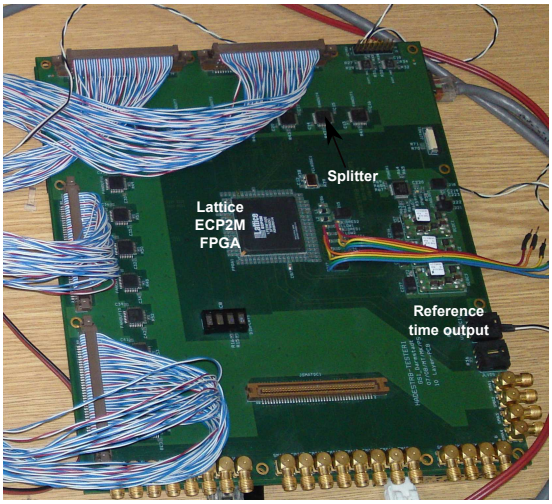

(a) Tester AddOn board top view with visible on the photograph cables going to the TRBv2 being under a test.

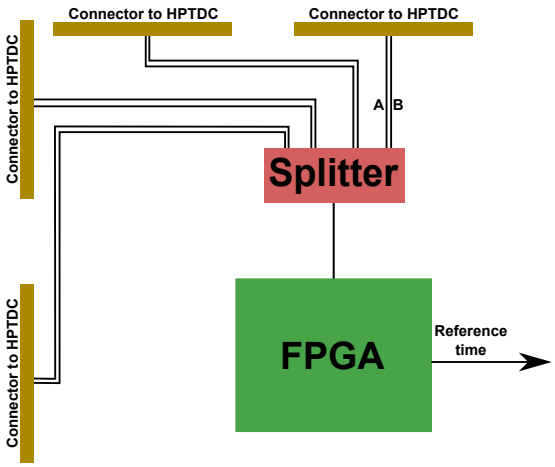

(b) Block diagram of the AddOn Tester board. One signal sent from Lattice FPGA to 8 different HPTDCs channels.

Figure 9.5: Tester AddOn with a lattice ECP2M FPGA.

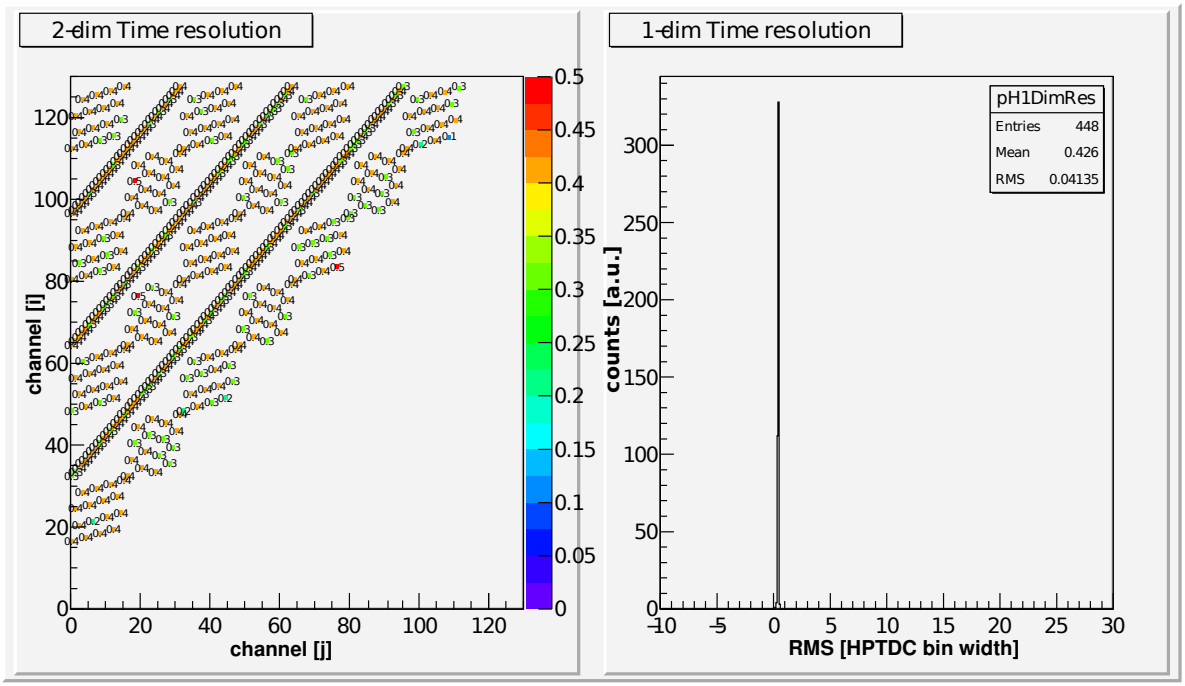

Figure 9.6: High Resolution (HR) mode. On the left side the channel to channel time resolution for all 128 TRBv2 HPTDC inputs. On the right side an accumulated RMS of all channel to channel measurements.

mode, in the HPTDC, only one fourth of the channel numbers is available - the rest is used to improve the performance of the HPTDC in terms of the time resolution.

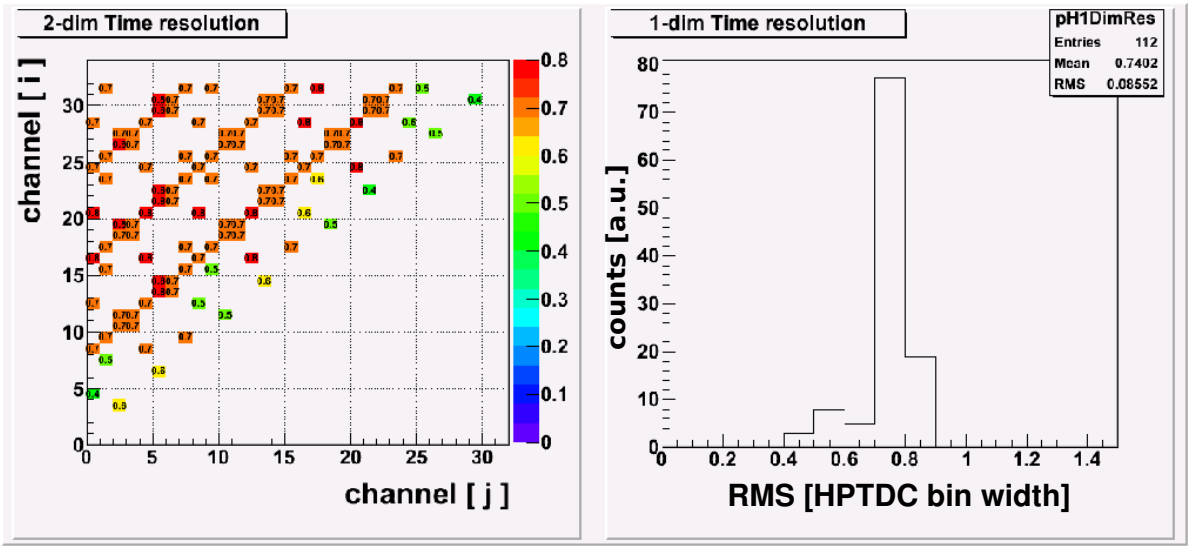

Figure 9.7: Very High Resolution (VHR) mode. On the left side channel to channel resolution for all 32 TRBv2 HPTDC inputs. On the right side accumulated RMS of all channel to channel measurements.

In such conditions, the whole test system delivers $RMS = 0.74 \times bin\ size = 17.8\ ps$.

The achieved time resolutions of the TRBv2 for the HPTDC High Resolution mode and the Very High Resolution mode are comparable with this what the manual of this ASIC demonstrates (see Tab. 9.2).

Table 9.2: Intrinsic HPTDC and the test system time resolution comparison.

Mode	HPTDC [ps]	TRBv2 [ps]
High resolution mode	34	40.9
Very High resolution mode	17	17.8

This is due to the fact that the PCB layout was prepared with great carefulness to guarantee the impedance matching and the decoupling of the transmission lines of the LVDS-timing signals. To accomplish corresponding outcome it was also necessary to apply corrections for time to digital conversion non-linearities. Accordingly, a code-density test was applied (signals delivered from Tester AddOn). Such test is based on delivering to the

HPTDCs a large number of the hits (to get a significant statistics) from some uncorrelated source. Afterward, it can be seen, which bin (a raw value of the measurement, in HR mode it is enough to check 8 bits, in VHR mode 12 bits) of the given channel is getting less or more data. The plot in Fig. 9.8 shows an example of such corrections for one channel in VHR mode.

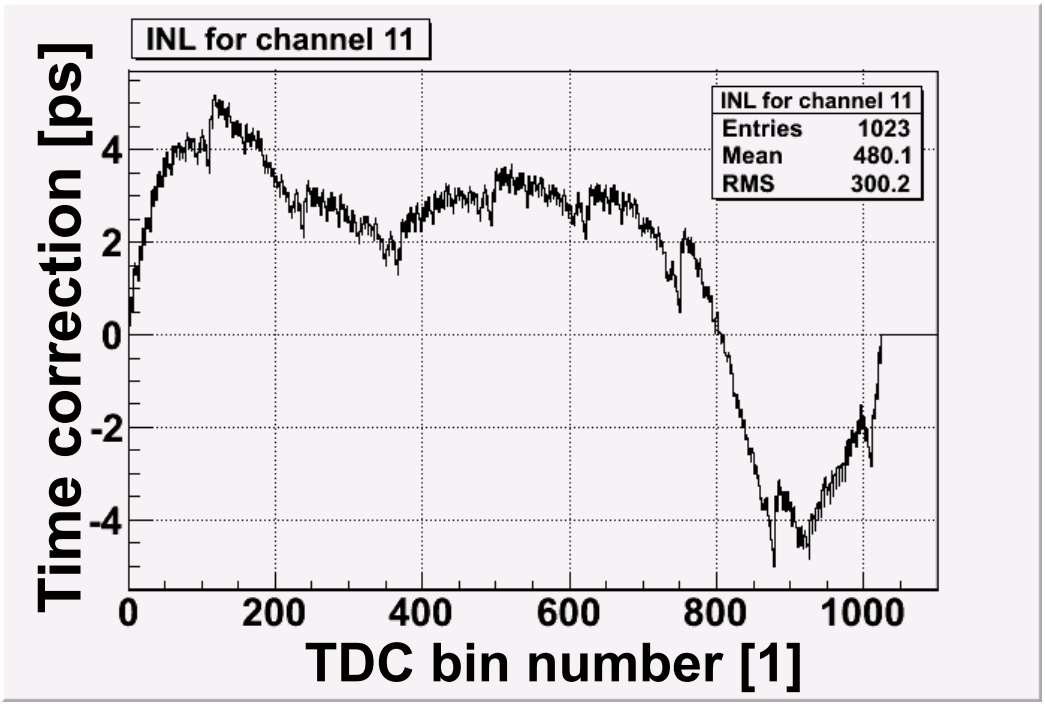

Figure 9.8: Time corrections in Very High resolution mode for one channel.

The main purpose of the TRBv2 is to serve as main readout board for the timing detectors and to be integrated with the HADES DAQ. Since all the other detector specific electronic readout boards were supposed to be exchanged, the idea of one platform was also implemented in area of the trigger, data and slow control transfer. There is also one common protocol for the data/control/trigger transport to connect all boards - TRBnet. The whole description of the TRBnet can be found in the J.Michael Ph.D thesis [96].

When describing the whole process of the event readout, it is necessary to start from the source of the triggers - the Central Trigger System(CTS). The whole process starts, when an appropriate layout of detector trigger signals (see chapter 9.8.2) forms a trigger for the whole HADES system. In such situation the reference time and the LVL1 trigger on the TRBnet side are sent separately. There is also a constant need to send special types

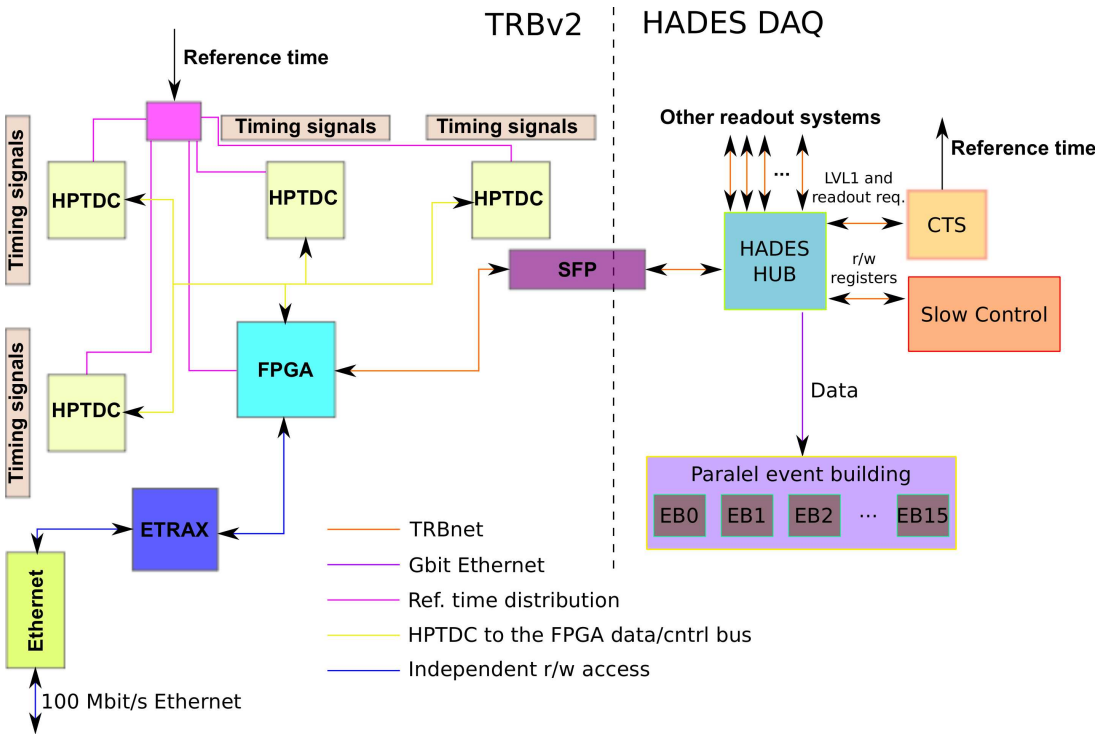

Figure 9.9: The TRBv2 in the HADES DAQ system. Different color lines indicates media or protocol types. Based on the incoming TOF/RPC multiplicity signals the CTS initiates the readout on all other readout boards. The data from the readout board is transported vi TRBnet to the HUB and next to the EBs vi Gbit Ethernet.

of triggers for a specific subsystem to perform suitable actions (see section 9.8.2). In this situation only LVL1 trigger (with special trigger type number) via the TRBnet protocol is transferred. The TRBnet packets are sent via optical links to specially designed HADES HUBs (section 9.9) and to the final destination - in the shown example to the TRBv2 (see Fig.9.9).

When the TRBv2 receives either the reference time or LVL1 TRBnet packet it starts the HPTDC readout. Then, it saves the event to its internal FIFO and transports it further to a TRBnet buffer (still inside the Virtex FPGA). When this process is finished the LVL1 busy release signal is sent to the CTS. All other readout boards are acting in the same manner and all these systems signalize on appropriate time to the CTS, that the first phase of the readout is finished. Next, the CTS can send either new LVL1 trigger (together with the reference time) or a readout request. After the readout request,

the collected event is sent to the HADES HUB (see chapter 9.9) and via Gbit Ethernet further to the event builders (EBs). As it can be seen the read/write access to the internal registers of the Virtex FPGA can be done by using the TRBnet protocol from the Slow Control board (the TRBv2 can be adopted to function as a source of the Slow Control requests). There is also an independent way for r/w operations - via $100M\ bit$ Ethernet and Etrax FS processor. This alternative route is useful particularly for the stand alone systems.

9.2 Front-end and Readout Electronics of RPC Detector

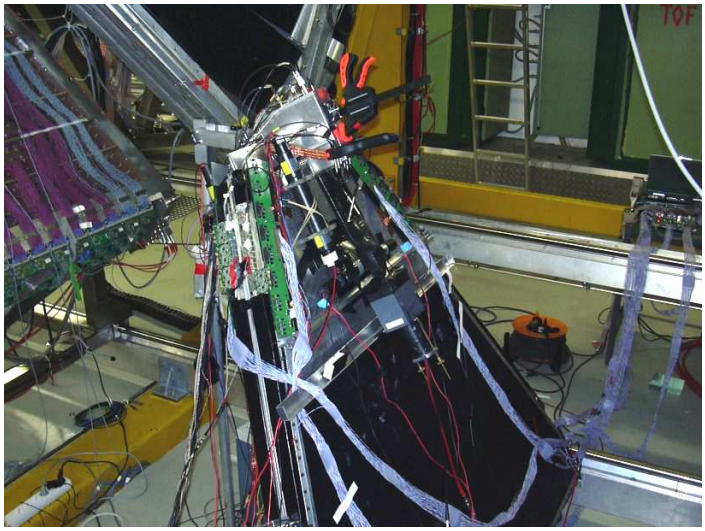

Figure 9.10: RPC detector test in 2005, with visible photomultiplier attached to it - a reference detector.

The development of the RPC detector took place in last few years. Finally, it is installed and integrated with the HADES detector [61]. To make possible such final to become a true and undoubtful success a few years of testing the prototypes and commissioning had to be in the background of such detector development. In parallel to the building of the detector also front-end and readout electronics was design and prepared. There were several significant steps during this process. To show how this whole process evolved in time, few of the steps will be highlighted. The first test under the beam conditions

were completed in 2005 year. In Fig. 9.10 there is a visible RPC detector with partially mounted on it front-end electronics.

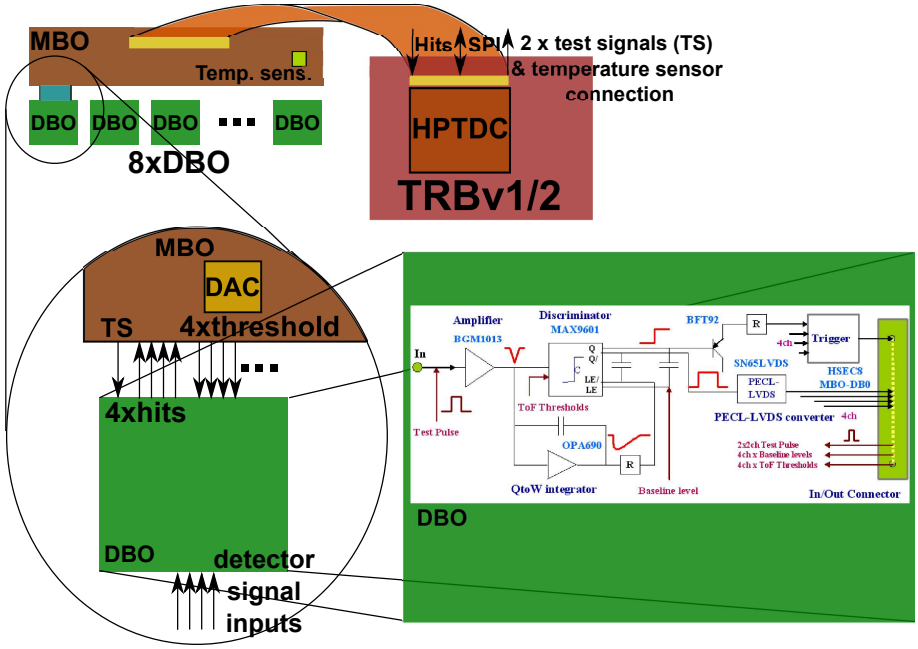

Figure 9.11: Architecture of the RPC detector front-end electronics connected to the TRBv1/2 board.

This electronics consist of a Mother Board (MBO), which serves as a distribution platform for the power and threshold settings for the attached to it Daughter Boards (DBO). On the DBO are placed operational amplifiers and discriminators. The thresholds on the DBO are set from the TRBv1/2 board via SPI (Serial Peripheral Interface [97], see Fig. 9.12).

At this point of time (TRBv1 was used) it was possible to achieve 86 *ps* of time resolution (detector plus all electronic boards). This scheme of the electronics chain design was kept in the next phases of the detector and its electronics development and commission time (Fig. 9.11).

In 2007 the TRBv2 was already existing and also one full sector of the RPC detector was equipped with the front-end electronics. The readout part was connected with currently existing trigger and data distribution system (see section 2.3).

The configuration in Fig.9.13 allowed to check the tracking performance with connection to the whole HADES system: 95% efficiency over selected large detector area and

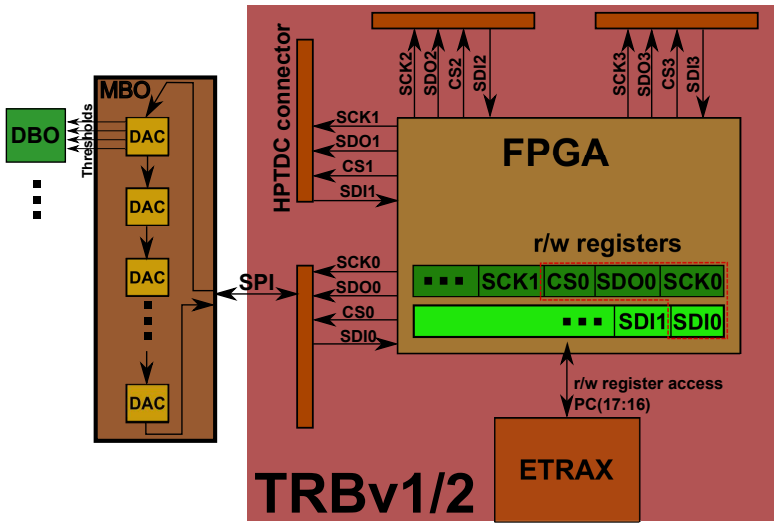

Figure 9.12: Thresholds programming by accessing the FPGA registers, which are linked with the SPI of a Digital to Analog Converter (DAC) chain (8 per MBO)

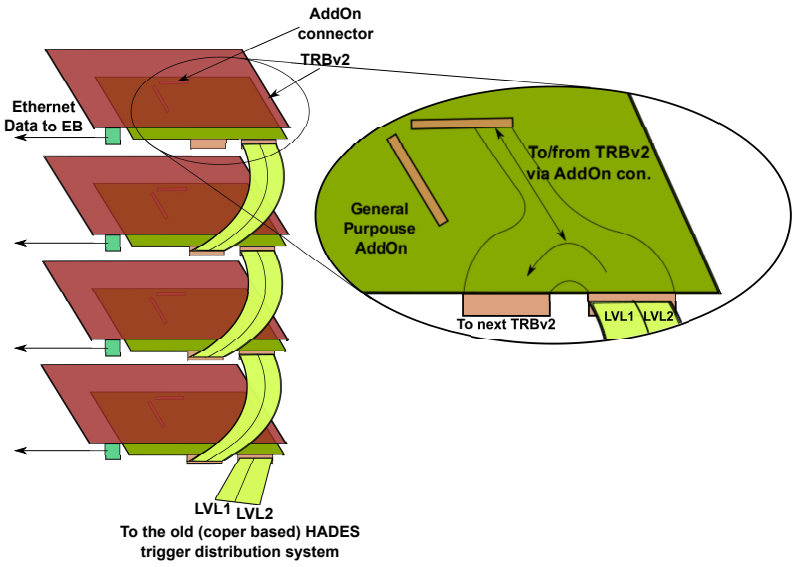

(a) RPC detector test in 2007, configuration of the readout setup.

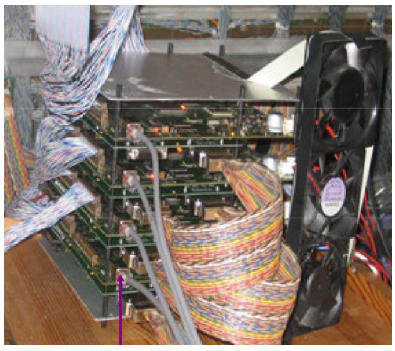

(b) Pictures taken during this test.

Figure 9.13: 2007 year test setup.

average time resolution of 81 *ps*. The obtained results were more than satisfying and at this point of time it was decided to go for the mass production of all 6 sectors. Built a stand alone readout system independent from the HADES DAQ made the detector test process much easier to perform. It was also prepared to connected two RPC sectors at the same time (see Fig.9.14). In this setup eight TRBv2 boards were used as readout

electronics. One TRBv2 connected with the GP AddOn was playing the role of the CTS and the newly built optical Test HUB AddOn was used as a trigger and busy signals distributor (optical connections).

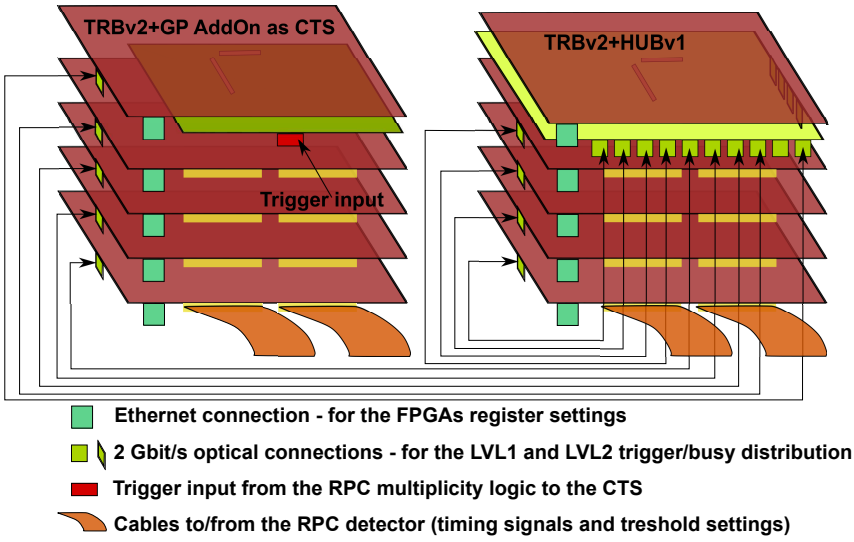

(a) The block diagram of the setup used for the final RPC tests.

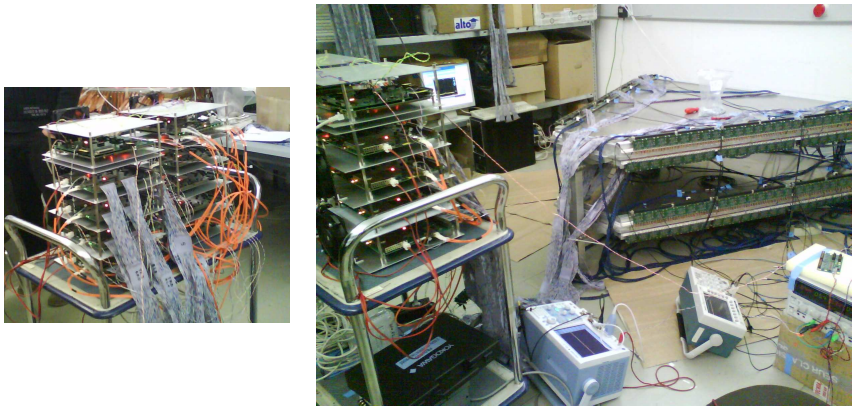

(b) The pictures taken during installation of this setup.

Figure 9.14: The 2008/2009 year test setup.

After all evaluation phases of the RPC detector, in 2010 it was fully integrated with the HADES system. After this significant effort, there were further test/commission beams. That allowed came to the following results (still with some place for the improvements) for all six RPC modules :

- average time resolution : 73 ps
- average position resolution : 8 mm

- average efficiency 94 %

9.3 Front-end and Readout Electronics of TOF and Forward Wall Detector

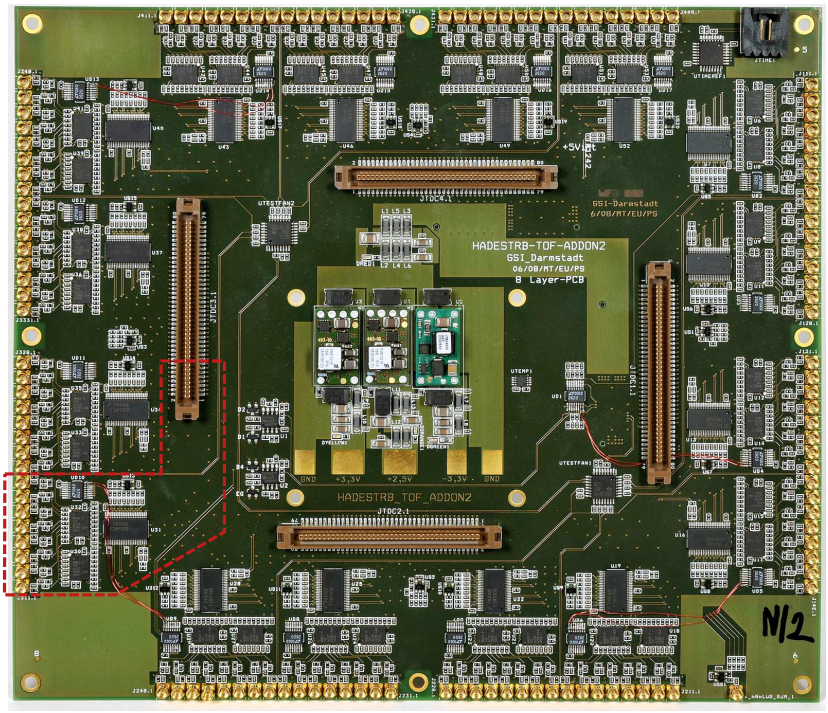

Figure 9.15: TOF AddOn. The marked area covers eight detector channel inputs - as it can bee seen the rest of the inputs are symmetrical to this region

For the Time of Flight and Forward Wall detectors it is necessary to use a specially designed AddOn board, called TOF AddOn. The TOF AddOn has 128 channels, which fully covers one sector of the TOF detector. The information attained from the Photo Multiplier Tube (PMT) signal is:

- arrival time - time of the particle crossing the detector,
- generated charge - energy deposited (energy loss) by the particle in the TOF/Forward Wall detector.

In order to perform measurements mentioned above the TOF AddOn is equipped with NINO [98] ASICs, which are designed at CERN for the ALICE TOF detector. The input

signal is split to two and fed into two individual inputs of the NINO chips (slow and fast NINO, Fig.9.16).

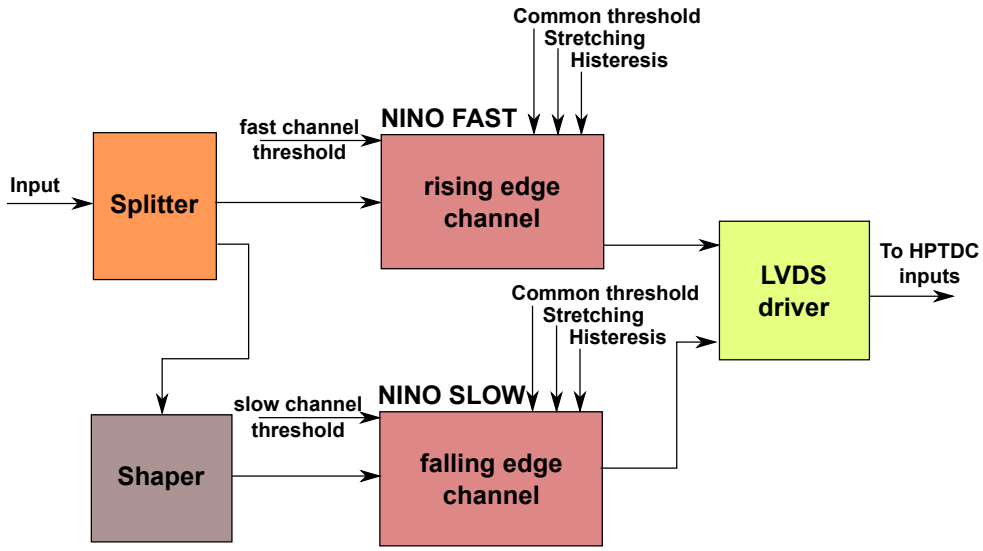

Figure 9.16: TOF AddOn channel block diagram.

On the first one the rising edge of the signal is discriminated (with thresholds set from ETRAX-FS fig.9.17). On the second the falling edge is created, but first the signal is shaped and discriminated in the way that the time distance between the rising and falling edge is proportional to the particle energy loss. The signal generated out of these two edges is sent to the HPTDC placed on the, attached with AddOn connector, TRBv2.

To do correct discrimination in the NINO ASIC, the chip itself provides several settings, which can be fixed with applying appropriate voltages:

- common threshold value (coarse)
- stretching of the output signal
- setting the hysteresis
- channel threshold value (fine)

First three parameters from the list can be applied individually for the fast and slow part of the measured signal. All these voltages are set from the ETRAX-FS, which has direct access to the DAC SPI lines via port E and the addon connector.

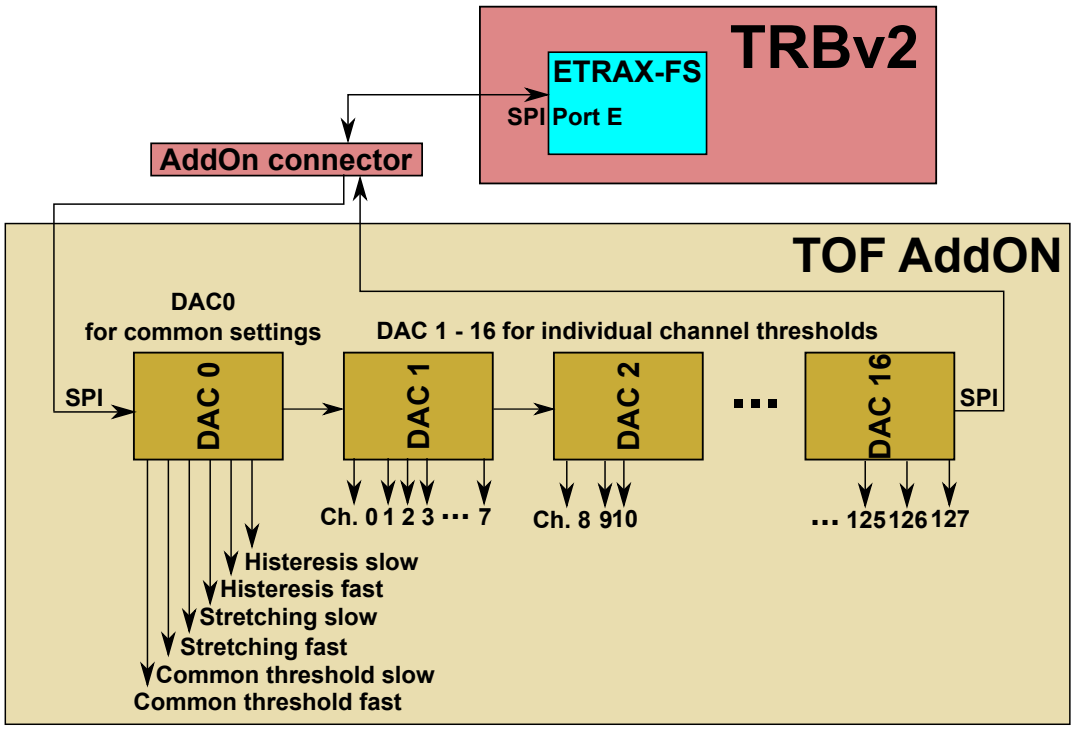

Figure 9.17: SPI chain for the thresholds programming on the TOF AddOn.

As it was mentioned before, one TOF AddOn is connected to all 128 channels of one TOF sector. This leaves no space for the measurement of the reference time, demanded for synchronization with other detectors. That's why every 32nd channel is logically OR-ed with the reference time to overcome this problem. Desired additional electronics is placed directly on the TRBv2 and its placed on the specially left open pads. In this situation, the signal coming from the hit and reference time has to be distinguished. This can be done easily by applying time window cuts on the measured times of the signals, which are suspected to be reference times (Fig. 9.18).

With such configuration of the hardware the TOF AddOn introduces 30 ps additional jitter to the signal. The power dissipation for the individual channel is on the level of 80 mW. The process of the integration of the TOF/Forward Wall electronics took place between 2010 and 2011 and was successfully commissioned and approved for the future HADES experiments.

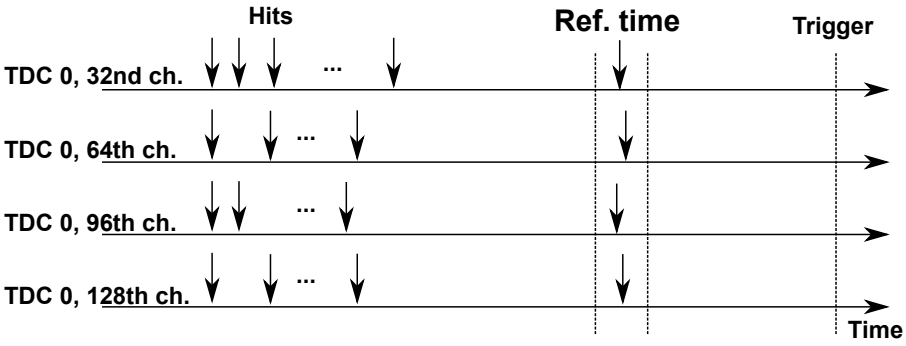

Figure 9.18: Classifying signals on the 32nd channel when the hit and reference time is on the same channel.

9.4 Front-end and Readout Electronics of START and VETO Detector

The board used for the readout of the START and VETO detectors is the TRBv2. Since there is only 8 channels to read from one detector and also the time resolution is an important factor in the process of different particles species separation, the HPTDCs are used in very high resolution mode. Just to remind - in this mode the time resolution is on the level of 20 *ps* and 8 channels per one HPTDC are producing the results of the measurements.

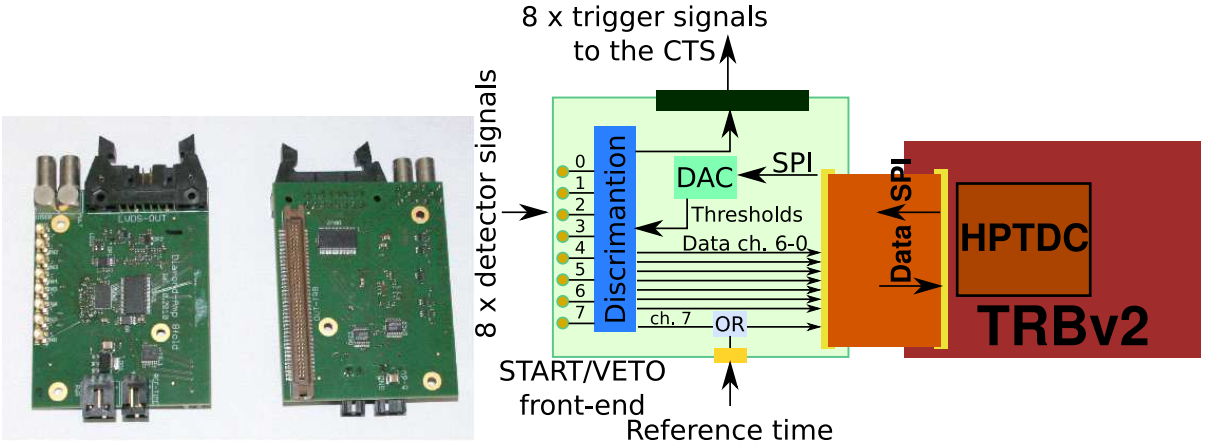

(a) Top and bottom view.

(b) START/VETO front-end electronics block diagram.

Figure 9.19: START and VETO front-end electronics.

As it can be seen in Fig. 9.19b the signals from the detector are coming directly to

the discriminator. The discrimination levels are linked directly with voltages set on the DAC chip. The values of these voltages, like in case of the RPC front-end electronics, are set via the SPI with the chain of Etrax FS and the Virtex FPGA registers. After the discrimination the signals are split into two groups: one group is transported to the central trigger system board (CTS) and the second one is linked with the HPTDC inputs. One signal out of this eight is treated in a different way. The reference time, which is essential for different systems synchronization is logically OR-ed exactly with the $7th$ signal. The obtained results from the 2010 test and commissioning beam time time regarding the RMS time resolution was $\sigma = 32\ ps$ - detector, front-end electronics and measurement all together. This was possible after the corrections of measurements nonlinearities, signal walk corrections and cross talk rejection.

9.5 Readout Electronics of Shower Detector

The development of the Shower readout electronics can be divided into two phases. In the first phase the Shower readout prototype was built providing a test platform used for given hardware configuration:

- Variable Gain Amplifiers (VGA) to gain the signals coming from the Shower detector Front End Boards (FEB, [99]),
- 8-channel 10-bit analog to digital converters (ADC, AD9212) (in total 96 channels on the board),
- Lattice LFE2-70E-5F900C FPGA chip,
- three DACs for the VGA gain setting (one chip per one Shower detector plane).

In this first step the TRBv2 was used for the readout. The data was transported through the AddOn connector to the TRBv2 Virtex FPGA and further to the Etrax FS and with User Datagram Protocol (User Datagram Protocol) packets to the Event Builder (EB). This first stage confirmed that the proposed board architecture concept is adequate to the needs and then the final board was built (Fig. 9.20).

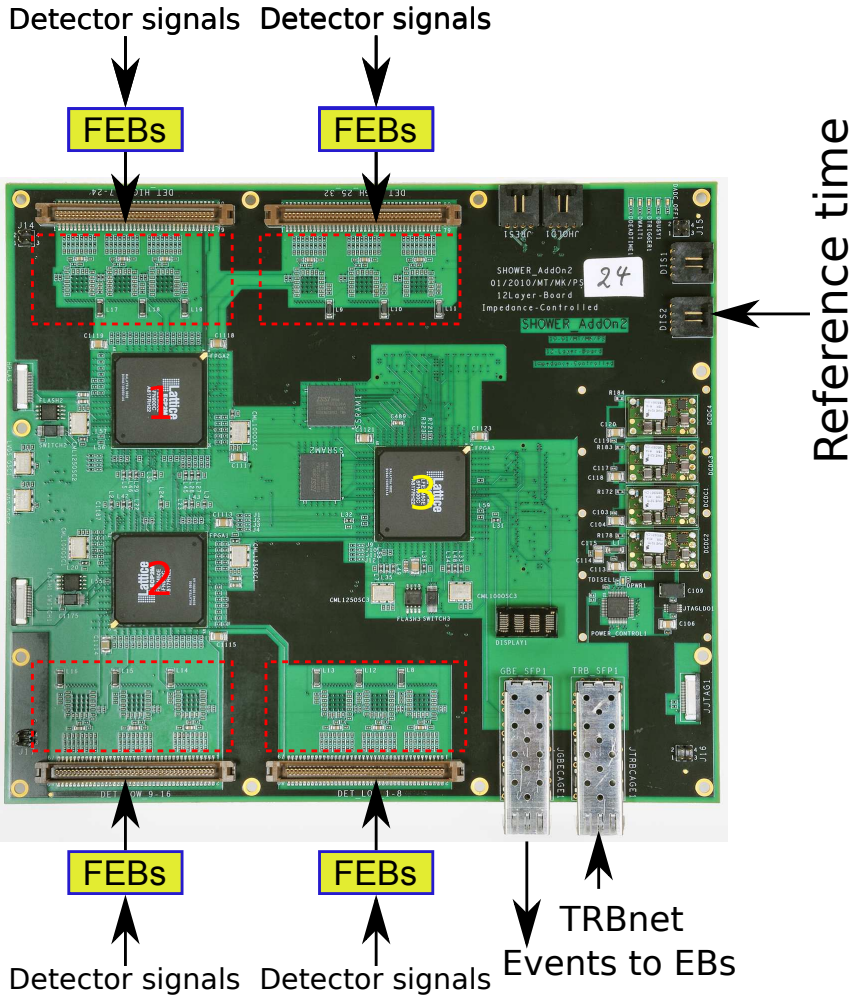

Figure 9.20: The Shower readout board.

The Shower AddOn readout board placed in the HADES DAQ system operates in three different modes:

- data taking,
- calibration,
- maintenance.

In the data taking mode, the Shower AddOn after receiving the LVL1 trigger (or the reference time) starts the readout process. It forwards the trigger to the FEBs. The FEBs constantly convert a charge coming from the detector to the electric signal, which amplitude is proportional to the charge value. These analog values are saved in the local

capacitor C_R. After receiving the forwarded trigger the outputs of FEBs are multiplexed to the Shower AddOn DACs, digitized and read out by the FPGAs (Fig. 9.20 - first and second FPGA marked on the picture). After this readout sequence all C_R are discharged. Acquired values are compared with previously set thresholds (maintenance mode, accessing FPGAs via TRBnet). The thresholds allow to reject noise coming from the detector. Next, the data is transferred to the third FPGA, where it is combined and sent further via Gbit Ethernet to the Event Builders (EBs).

When the board operates in the calibration mode (after receiving a Shower calibration trigger via TRBnet from the CTS), the Shower AddOn starts the process of injecting a defined charge (the charge alternates 10 pC with 0 pC) to the channels of the FEBs. In the next step, the readout process take place. Base on the collected data the detector can be calibrated.

9.6 Readout Electronics of MDC Detector

The MDC readout electronics upgrade can also be divided into two phases. In the first phase like in the case of the Shower AddOn, a MDC readout prototype was built and it served as a platform to check the possibility of replacing the old MDC readout chain. Again the TRBv2 (like in the Shower AddOn upgrade process) was used as a support for the data readout. In this first stage all connections were electrical and this type of connection was proven to be a source of noise. This was the reason of changing the media for the data transfer from the electrical to the optical links. Taking into consideration a limited space in the detector area (400 readout boards) the Plastic Optical Fiber (POF) [100] links and Fiber Optical Transceivers (FOT, FDL300T from Firecomms) were determined as a best candidates to perform the data transmission. The chosen POF technology is cheaper and easier to handle than glass fibers.

Based on all experiences gained during the previous system usage and the first phase of the development of the MDC readout electronics it was decided to:

- keep the daughter boards responsible for the detector signal gain and discrimination,
- continue to use mother boards, on which the time measurement is performed (TDCs

are placed there, Fig. 9.21a),

- replace the whole readout chain with two types of boards:
  - Optical End Point Board (OEPB),
  - MDC HUB.

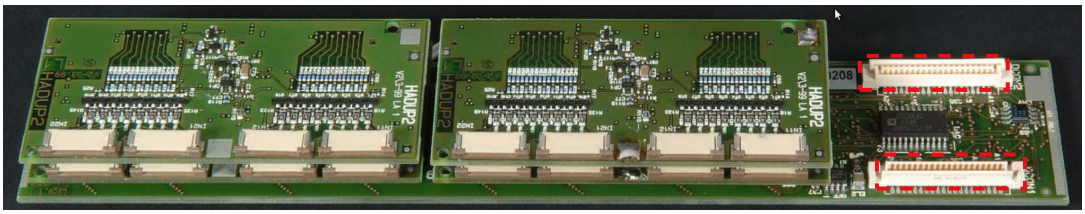

(a) MDC mother board with attached to it daughter boards.

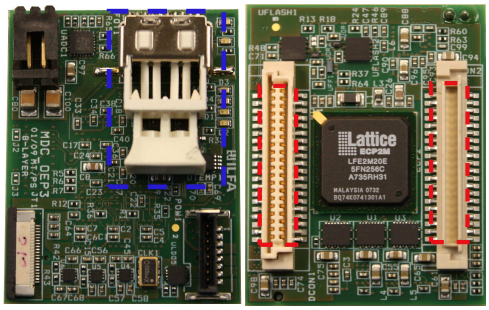

(b) Optical End Point Board.

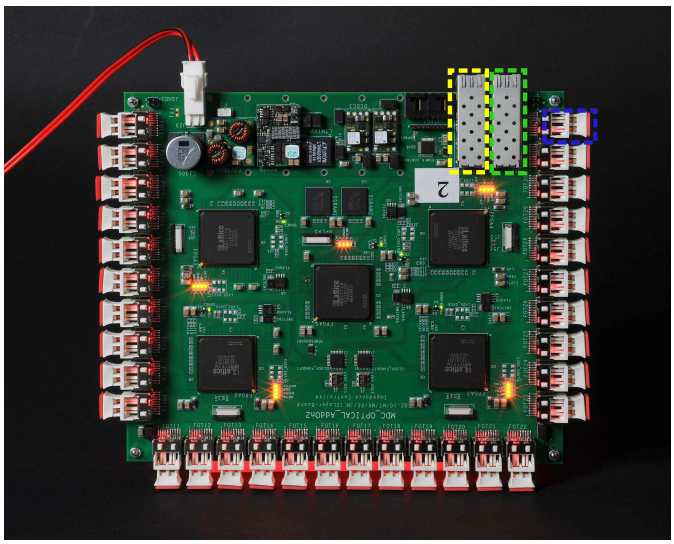

(c) MDC HUB.

Figure 9.21: MDC detector electronic hardware.

Measurements done by the TDCs are acquired by the Lattice ECP2M20 placed on the OEPB (via the connectors marked with the red dashed line, Fig. 9.21a and Fig. 9.21b). Afterward, the collected event is transmitted with 250 $Mbit/s$ speed to the MDC HUB via Plastic Optical Fiber (blue dashed line, Fig. 9.21b and fig. 9.21c). The data is received by the MDC HUB, which is equipped with 32 optical transceivers. To cope with such amount of connections and data, this board is equipped with five Lattice ECP2M100 FPGAs. Four of this FPGAs are used for all data transfer to/from group of 8 OEPBs. The fifth one is used to collect all the data and send it via Gbit Ethernet (fig. 9.21c yellow dashed line)

to the EBs. The TRBnet entity is implemented in all above mentioned FPGAs (OEPB and MDC HUB) and besides the data transfer it manages also the transfer of the LVL1 trigger, data readout request and slow control data. All transmissions are done on the same optical connections.

To prove the stability of such big system an irradiation test has been performed at GSI. During HADES p+Nb production beam time at $3.5GeV$ of kinetic energy, the OEPB was placed near the beam dump. The purpose of such test was to see the reaction to the exposition to different reaction products (pions, protons, and heavier fragments). By using dedicated Single Even Detection (SED) component, available in the Lattice FPGA, it was possible to observe an average of 2 errors per hour at a particle rate of 10^6 $\frac{particles}{scm^2)}$. Though, changing the position of the electronics to the comparable of the final OEPB location caused absence of the errors induced by the radiation [101].

9.7 Front-end and Readout Electronics of RICH Detector

In case of the RICH detector, in the phase of the HADES DAQ upgrade, both the front-end electronics and digital readout were redesigned and rebuilt. The overview of the system is presented in Fig. 9.22c.

The detector signals are linked with the analog front-end card APV ASIC inputs. The APV ASIC has 128 input channels, which amplify shape and save the incoming signals to the internal analog memory. After the arrival of the LVL1 trigger, the Analog to Digital Converter Module (ADCM) initiates the readout of the APV (by two 12 $bit, 40$ MHz ADCs), digitizes the data, forms the data event and sends it with TRBnet protocol, via the optical links to the HADES HUB (section 9.9).

In order to offer the described functionality ADCM module contains the following components:

- the optical connection to the whole HADES DAQ system (SFP),
- the Lattice FPGA ECP2M100 for the ADC control, online calculations, data compression and TRBnet functionality,

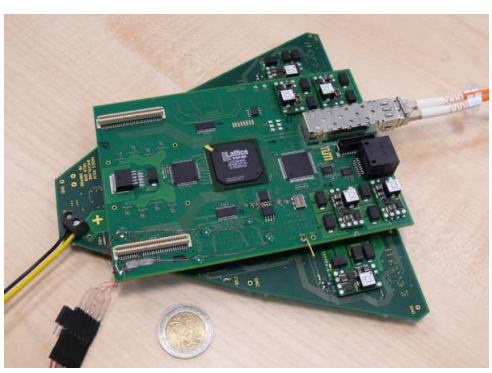

(a) ADC module.

(b) APV front-end.

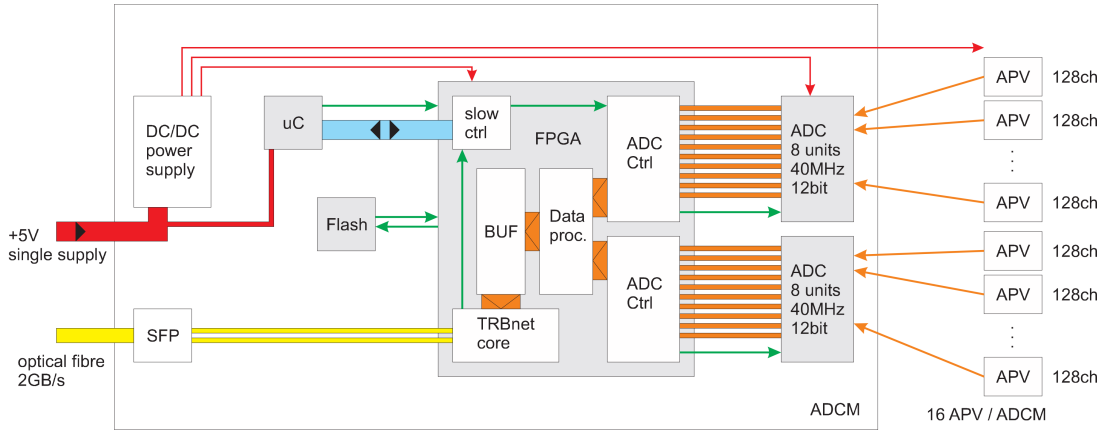

(c) Block diagram of the RICH readout and front-end electronics.

Figure 9.22: New RICH detector electronics.

- RISC micro-controller for slow control and power supply quality constant check,
- SPI flash for the automatic hardware boot procedure after the power cycle.

9.8 HADES Trigger System

9.8.1 HADES Detector Trigger Signals

To start, described in previous subsections, the detector electronic readouts a defined pattern of detector trigger signals is used. This signals arrangement indicates, that interesting physics appeared during the ion, proton or pion collisions. Based on this the LVL1 trigger and reference time is sent from the CTS. In the HADES spectrometer the main trigger detector sources are:

- RPC,
- TOF,
- START and VETO.

The TOF hardware for these signals, produced and sent to the CTS, is located directly on the TOF AddOn. It consists of three levels of the summing modules. In the first level eight signals are grouped and summed. Four results of the sum are again summed and then out of this four the final signal is created (fig 9.23). The components are picked in the way, that a whole range of operational amplifiers (in the summing part) is used. The output signal is a linear function of the active inputs - 20 mV per one channel. One has to bear in mind, that one hit in the TOF detector creates two signals on the TOF AddOn (left and right side of PMT) and the corresponding signal is 40 mV high.

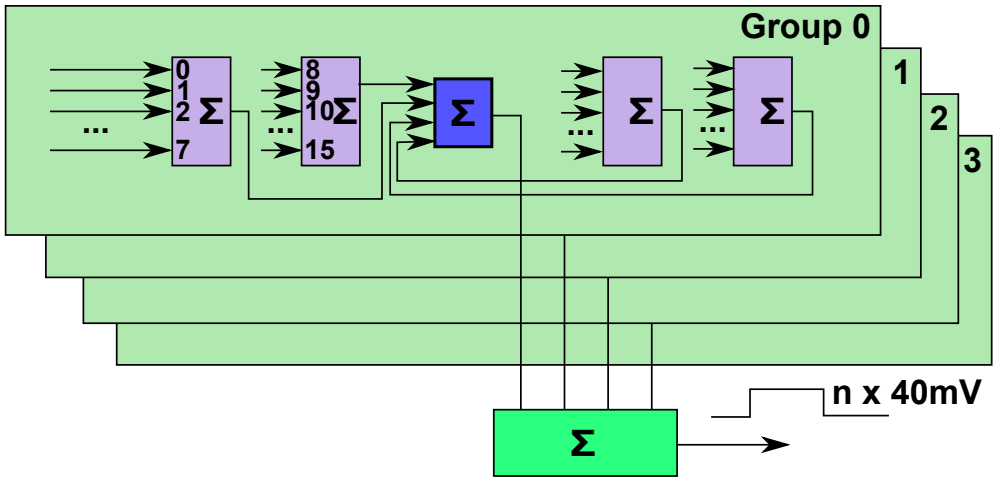

Figure 9.23: Creation of the TOF multiplicity signal.

For the RPC multiplicity trigger signal production a special board had to be created (see Fig. 9.24).

The multiplicity signals are initially created directly on the DBO from the sum of the four detector signals. After this, these eight signals are summed on the MBO (just to remind - eight DBO is attached to one MBO) and transported to the noticeable LEMO connectors. There are two visible LEMO connectors, which are placed in perpendicular way to the board. Left one is used to send final multiplicity trigger signal (a sum of all incoming signals) to the central trigger system board. On the second one it is possible to

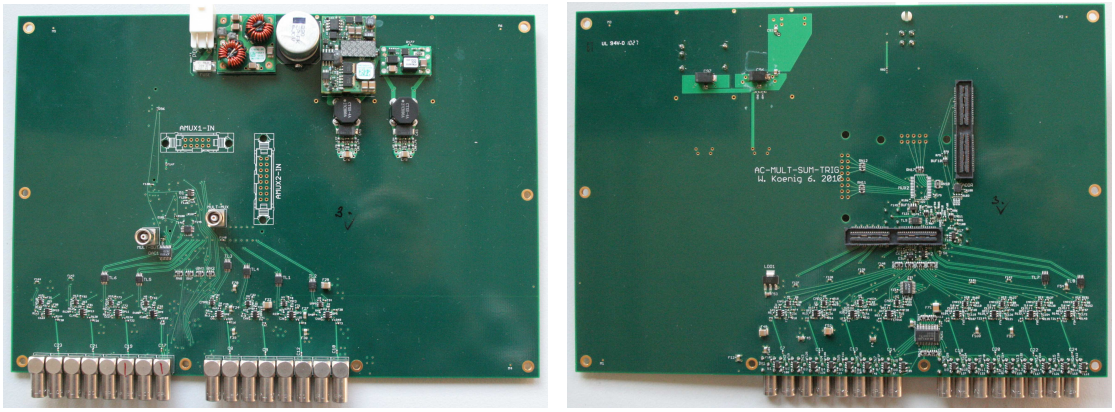

(a) Top view.

(b) Bottom view with visible AddOn connector.

Figure 9.24: Trigger multiplicity board for the RPC detector.

observe input signals. The selecting of the incoming signal is done via SPI by programming a multiplexer. The multiplicity board is attached via AddOn connector (fig. 9.24b) to the TRBv2. This allows to adjust remotely the thresholds (the DAC voltages) to discriminate the RPC detector signals. The access to the DAC and multiplexer chain is through the Etrax FS processor - like in the TOF AddOn (fig. 9.17). All arriving RPC trigger signals are going to the TRBv2 and are counted in the Virtex FPGA. Then the counter values are transported with a special trigger type (0xE) along with collected data to the event builder. This allows to check the performance and behavior of the specific RPC detector areas. It is also possible to send a test signals from the individual TRBv2 to check, if a related RPC part detector and electronics function in a proper way.

The trigger signals created in the TOF and the RPC detectors (timing wall signals) are summed together on the board, which is the same as RPC multiplicity board (the same length of the trigger signal cables is assured for this two systems). With such difference that to this board only a small addon is attached (instead of the TRBv2). The connectors which are marked in Fig. 9.25 provide:

1. the RPC and TOF trigger multiplicity signals from the individual sectors linked with the CTS,

2. three different multiplicity signals of the whole timing wall (the TOF and RPC detector together) - the multiplicity value corresponds to the particular threshold settings,

3. SPI (programming from the TRBv2) for the thresholds regulation - individual inputs and aggregated timing wall multiplicity signal discrimination,

4. SPI for selection, which input can be observed on the dedicated LEMO output (bottom side of the board)

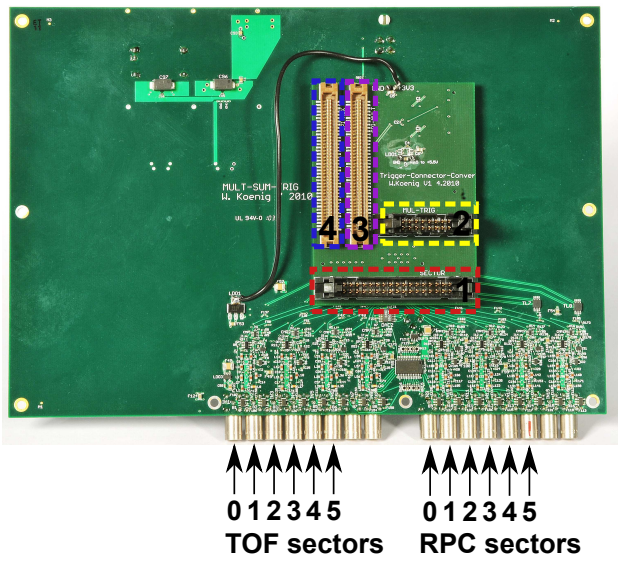

Figure 9.25: Central multiplicity unit.

In case of the START and VETO detectors the trigger signals are linked directly from the front-end electronic boards to the CTS (fig. 9.19b). The other important function, which the central multiplicity unit is responsible for, is compensation of the base line (ground level) shift in different parts of the detector. Otherwise, it would be not possible to relay on the input signals voltage levels especially when the lowest one is 40 mV.

9.8.2 Central Trigger System - CTS

The backbone of the new DAQ architecture are the fast optical connections. In this circumstances also the CTS along the other readout systems required rebuilding and a new board has been designed and constructed (Fig. 9.26).

The essential thing, which the CTS has to accomplish as piece of hardware, is to accept signals incoming from the selected detectors: TOF (6 inputs), RPC (6), START (8), VETO (8) and other physical triggers PT (8) and adjust them, such it is possible to

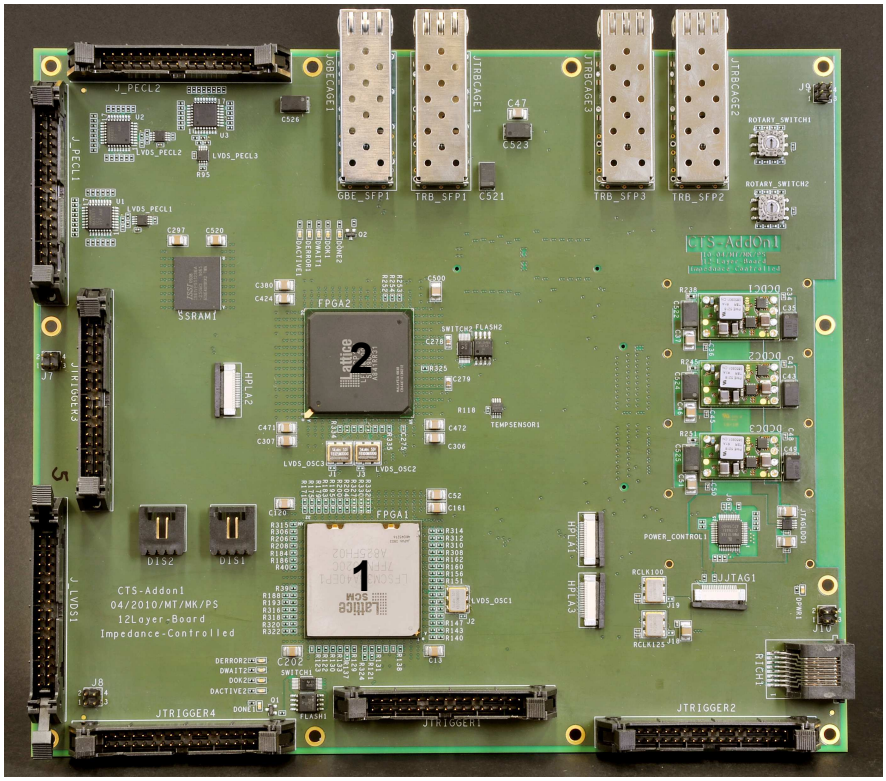

Figure 9.26: CTS board top view.

create the first level trigger signals (the LVL1 and reference time). The architecture of the algorithms running on the CTS has to take into account different conditions for the particular beam times (heavy ion or pion induced beams). This is assured by applying adjustable VHDL components inside one of the FPGA designs (Lattice SCM (marked as 1 in Fig.9.26) mounted on the board. Exactly this FPGA, is used to make all the operations on the incoming detector signals. The second one (Fig.9.26 - 2) is adopted for the standard HADES DAQ operations (via two optical connections) with the TRBnet protocol:

- slow control channel - accessing the CTS read/write registers,
- sending the LVL1 trigger and readout requests to the HADES detector DAQ systems (formed in the first FPGA),
- transmitting data from the CTS to the event builders.

Since the TRBnet protocol is implemented only on the second FPGA, to transfer data

from/to the first FPGA, a specially dedicated protocol is implemented between these two chips. Once all the detector specific trigger signals are created and sent to the Lattice SCM FPGA placed on the CTS, a basic manipulations on the incoming signals are started. The first logical input component is used to create out of the rising edge of incoming signal a pulse. This is due to the fact that this information is sufficient for forming the final LVL1 trigger signal (and the reference time along it). It is also easier to perform all later manipulations on this kind of the signal. The accuracy of the edge detection is on the level of 1.25 ns. This is accomplished by using the DDR architectural elements available in this FPGA, where the input signals are sampled with 800 MHz. Since the internal logic runs with 200 MHz clock the signal, which is created after DDR component is a 4 bit vector (see Fig.9.27). Value of this vector represents the sub-clock precision. Consequently in later steps, actions taken on the signals can be done with 1.25 ns precision and one has to remember that all these operations are done on the 4 bit vectors (if not mentioned otherwise).

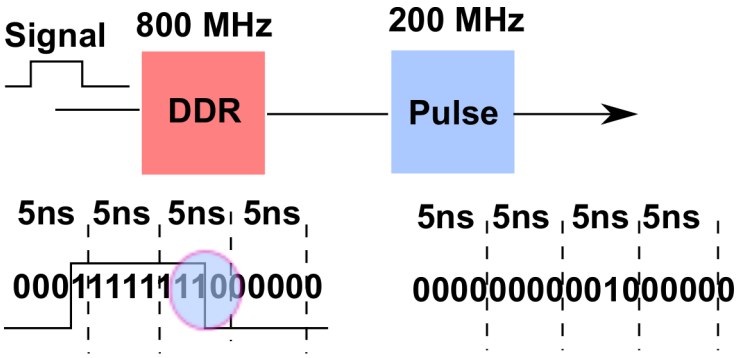

Figure 9.27: Creation of the pulse signal.

After the pulse creation the signal can be delayed. This is required in the case when from the different detector systems the detector trigger signal travel different distances. This it true for example for the TOF/RPC signals and the START detector signals. There are two types of delay components in the FPGA. One group is used to delay the signal with 1.25 ns precision. As it can be seen in Fig. 9.28 first the signal is rewritten to the new 12 bit vector - in the position defined by the delay value (in the shown example the delay equals to 5×1.25 ns). In the next steps this vector is saved to the temporary vectors A1, B2, C3 each after every clock cycle (5 ns). The final signal is created out of this three

vector signals by the OR operation.

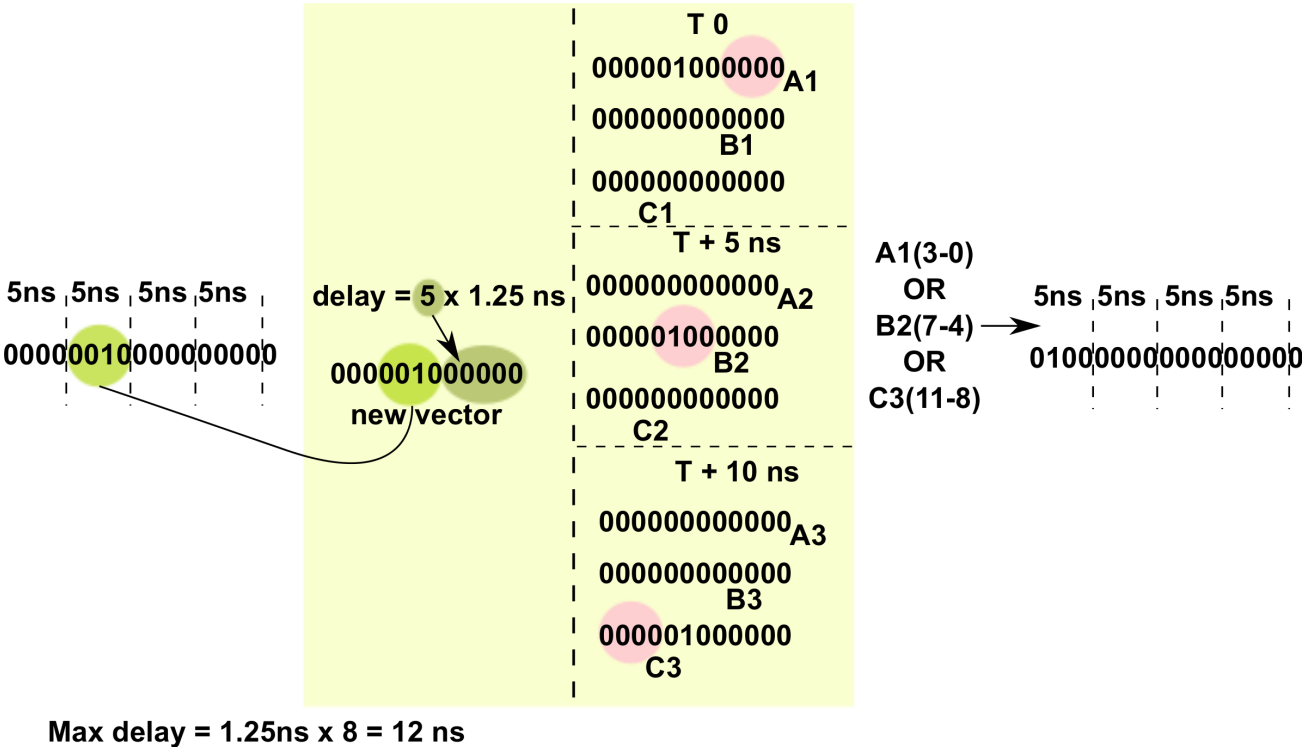

Figure 9.28: Delaying the signal with 1.25 ns precision.

Unfortunately such precision can not be used when it is necessary to delay signals by larger times (up to 1.3 μs). This would take too much hardware resources of the FPGA. Therefore, the second group of the delay components has granularity of 5 ns and allows to delay up to 8 signals in parallel. To make this possible, together with the low usage of the resources of the FPGA, the architectural component - the FIFO is used (see Fig. 9.29).

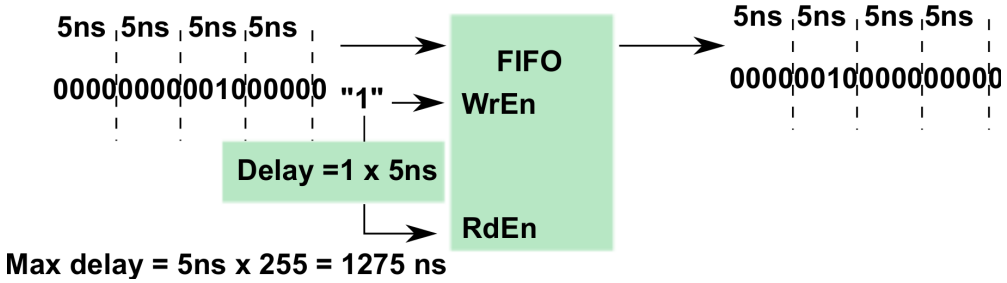

Figure 9.29: Delaying the signal with 5 ns precision.

Sometimes it is desired to suppress one of the types of the incoming trigger. In such

circumstances it is possible to downscale a given trigger signal and transport only each $2^{downscale\,value}th$ rising edge of this signal (see Fig. 9.30).

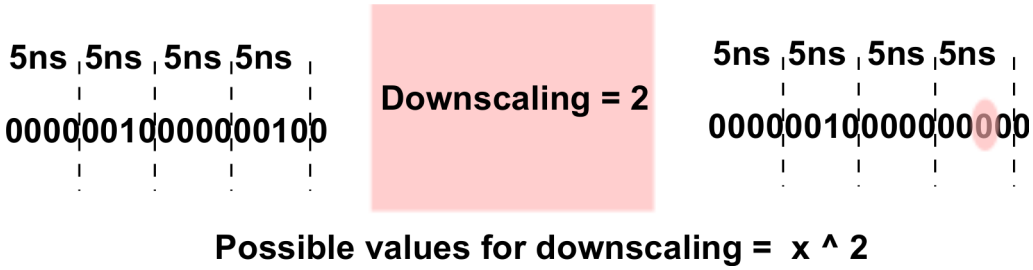

Figure 9.30: Downscaling the incoming trigger signal.

When the signals are aligned to each other (after applying a correct delay values), the next logical step is to widen the signals. This is done in order to get an overlap between the interesting signals. Again, like in the delay components out of the same reasons there are two types of this components. With the first type it is only possible to enlarge the signal with multiplication of 5 ns. The mechanism of this algorithm is quite simple. When width value is larger than 0 then according to the position of the input rising edge the corresponding output rising and falling edges are created - a Look Up Table is used for this purpose (LUT). Accordingly the output signal is created from these two edges and in between $(w-1)0 \times F$ vector signals are inserted (see Fig. 9.31).

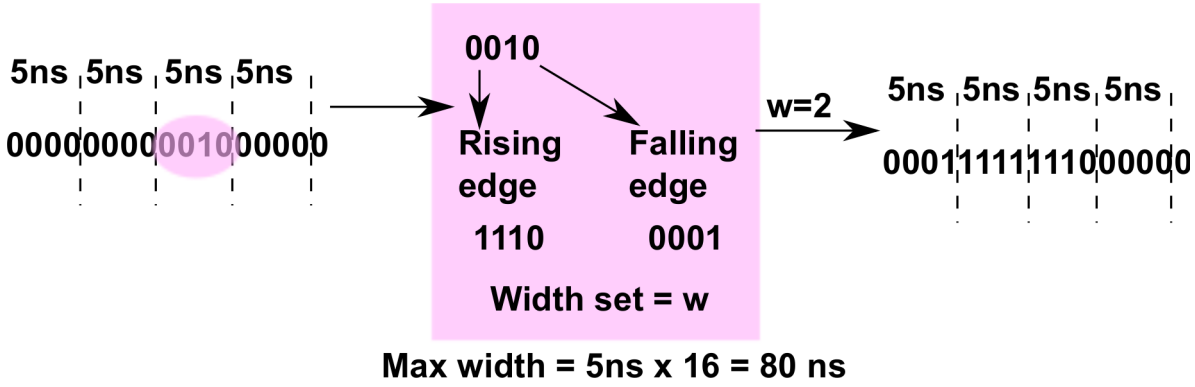

Figure 9.31: Setting the width with 5 ns resolution.

If the frequency of the signals, which are used in the process of finding the coincidence is large the 5 ns granularity of the width enlargement is not enough. This is the case when START and VETO signals are used for the final trigger creation. In this situation

a special component is used, which can enlarge the signal with a 1.25 ns step. This component consists of ROM which is working as a LUT and based on input signal creates immediately the output vector (see Fig. 9.32).

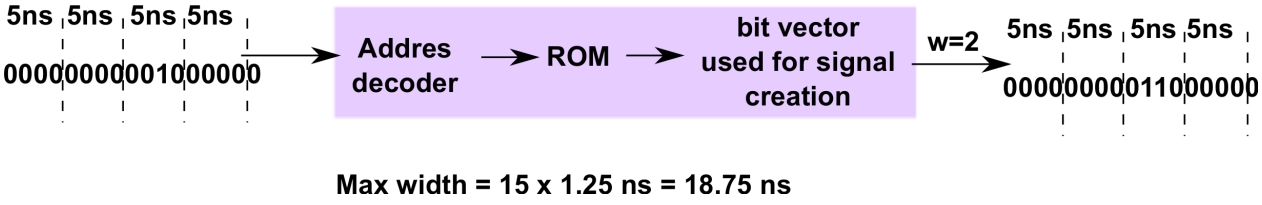

Figure 9.32: Setting the width with 1.25 ns resolution.

It is necessary to underline, that for the sake of description simplicity of the above components, this document does not cover some special cases of the incoming signal configurations and how these signals are handled.

Besides the mentioned functionalities (see Fig. 9.33 - full CTS trigger logic block diagram) the trigger logic can perform:

- enable/disable inputs and outputs,
- RPC/TOF sector-wise coincidences,
- enable anti-coincidence logic between the START and VETO signals,
- realize correlations between the START and VETO signals with all other trigger signals.

During the system operation it is mandatory to have a possibility to observe all signals, which are undergoing all manipulations mentioned above. This allows to properly set parameters like delays and widths to make a proper coincidence between a different signals.

This is assured by using two multiplexers, each one forwards selected signal to the output connector wired with the oscilloscope. In total there are 110 internal FPGA signals which can be observed:

- after the edge detection,
- after the delay,

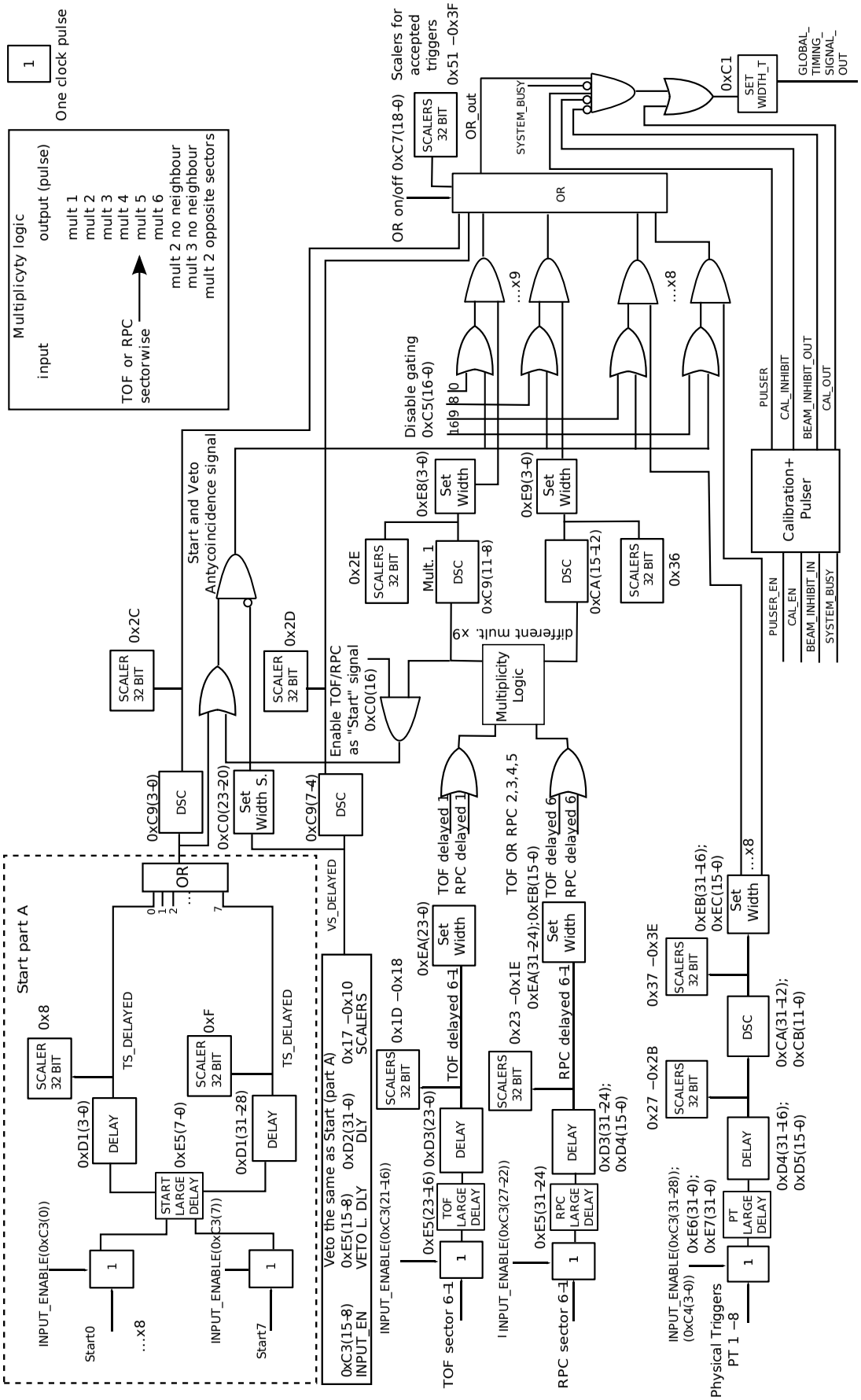

Figure 9.33: CTS trigger logic.

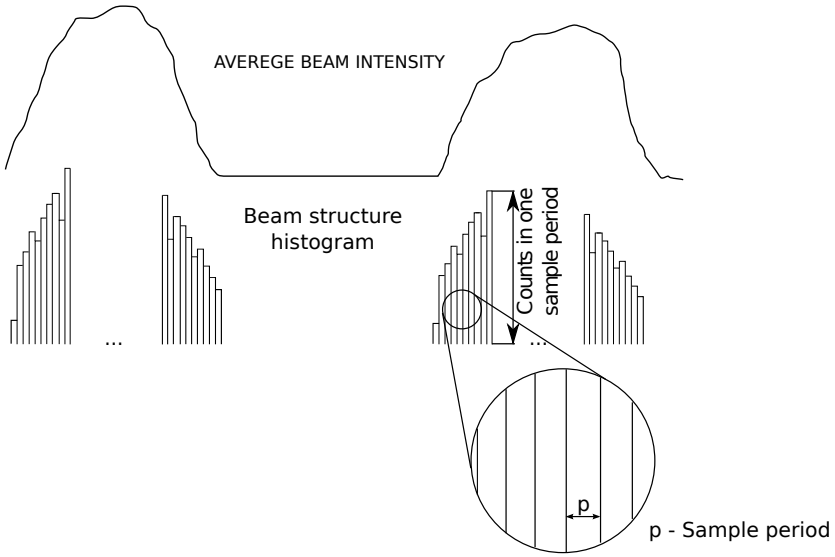

Figure 9.34: Example of the histogram created inside the Lattice SCM FPGA.

- after the width enlargement,
- START and VETO signals used for the coincidence signal creation.

To see these signals in appropriate way the internal 4 bit vectors are changed back with output DDR components to the LVDS signal.

Other important feature that CTS grants is a convenient judgment of the beam quality settings. The CTS creates from the START, VETO, RPC or TOF trigger signals ten different histograms (see Fig. 9.34). Each histogram has 500 samples and each sample corresponds to the number of hits in a given adjustable time. An example of usage of this histograms can be a correct beam focusing on the target. When the beam axis is moving during one spill it is visible on the acquired histograms from individual START detector channels. It is noticeable that maximum number of counts moves from one side of the detector (channel) to the other.

9.8.3 Trigger Distribution

In the previous subsection, the means how to create the LVL1 trigger, are in detailed manner presented. Aim of this section is to clarify how the CTS cooperates and is connected with other detector readout systems.

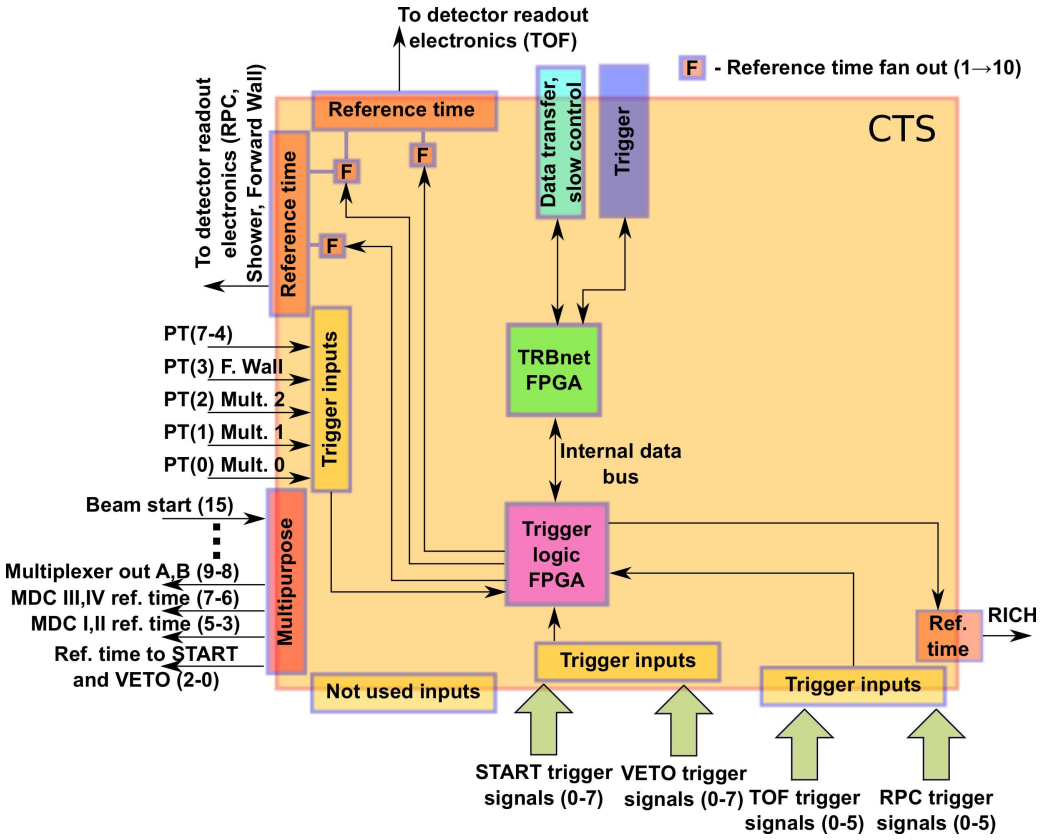

Figure 9.35: CTS - block diagram.

The CTS when accepting the given configuration of trigger coincidence signal has to take into account the busy (e.g. readout electronics is during the process of retrieving the data from the front-end) of the whole system. If all subsystems are ready to take a new event, then in such situation the LVL1 trigger can be sent via TRBnet protocol to the readout electronics. Inside the trigger data packet, transported via the optical links, there is a trigger number and trigger type. The trigger number allows to detect if any mismatch of the events collected on the tapes occurred. The trigger type informs what kind of action should be taken by the readout electronics:

- type 0x1 - normal data readout,
- 0x9 - MDC calibration, if enabled the CTS is sending this type of trigger,
- 0xA - Shower calibration, sent from the CTS on user request,
- 0xB - Shower pedestals, if enabled the CTS is sending this type of the trigger, when

there is a spill brake,

- 0xC - RICH calibration, sent from the CTS on the user request,
- 0xE - status information, sent each second, the subsystems should send actual status of its internal state machines, registers etc.

In parallel to the LVL1 digital trigger the CTS forms an analog reference time trigger. This trigger is sent with copper cables as PECL/LVDS 100 ns signal. This signal allows to synchronize data from the different detectors.

After each trigger the CTS waits for response from all subsystems which tells that full event was collected inside internal memories of readout electronics. After this it can sent the next LVL1 trigger and in parallel to it asks with readout request to send the data to the Event Builders. In the readout request packet the CTS inserts the EB number (corresponds to defined before IP address), to which the hardware responsible for forming the final event (HADES HUB, Shower AddOn, MDC HUB, RICH readout electronics) should send current event. In the new HADES DAQ system it is possible to have up to 16 EB and events are sent with round robin algorithm to these computers. How many events and which EB is used is defined just by writing the corresponding values to the CTS registers.

9.9 HADES HUB

To connect all subsystems into one optical network the HADES HUB board was prepared (see Fig.9.36). The main purpose of this board is to transport all of the internal HADES DAQ system data such as:

- LVL1 trigger,
- readout request,
- read/write access to the registers from/to different subsystems (slow control),
- collect incoming detector data and send it to the EBs via the Gbit Ethernet.

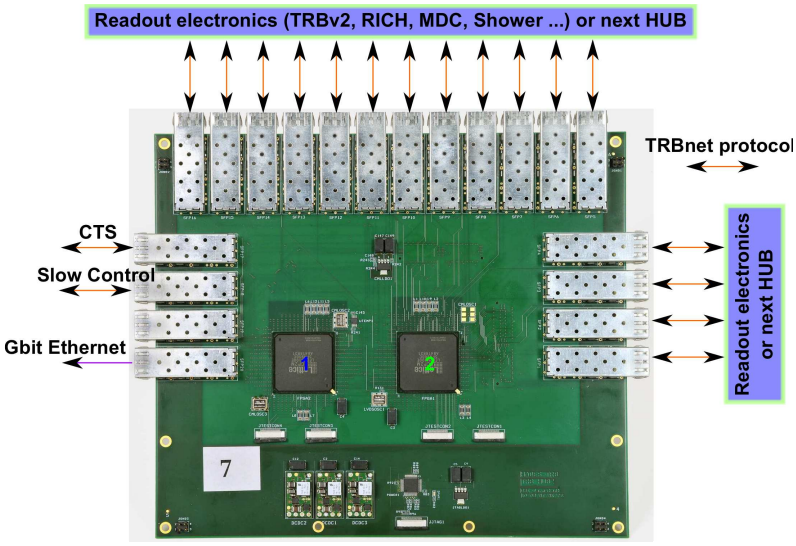

Figure 9.36: HADES HUB.

To cope with such amount of the data the board is equipped with 20×2.5 $Gbit/s$ optical connections controlled by two Lattice ECP2M100 FPGAs. In both FPGAs the TRBnet components are located and in the first one, to send the data to EBs, the Gbit Ethernet controller is implemented.

9.10 HADES DAQ Summary

During the HADES tests and commission beam times in the late 2010 the whole updated system was able to take for example in $U+U$ collisions at $1.2GeV$ a 500 MB/s with a 55 kHz of accepted triggers. How big transformation it is one can see when comparing with the old system performance - only ~ 2 kHz for Ca+Ca system. The whole overview of the HADES DAQ structure can be seen in Fig. 9.37. The multiplicity signals, created by the detectors as the result of the beam target reaction, are sent to the CTS (shown as dark blue lines). The CTS logic makes correlations among these signals with the predefined settings (via TRBnet - orange lines) and generates the LVL1 trigger transferred via TRBnet. In parallel the reference time is sent from the CTS to all readout boards (green lines). When the readout electronics receive the reference time, they start to acquire data from the front-ends or like in the case of the TRBv2 from the HPTDCs.

When all events are collected in the internal memories of readout boards and busy

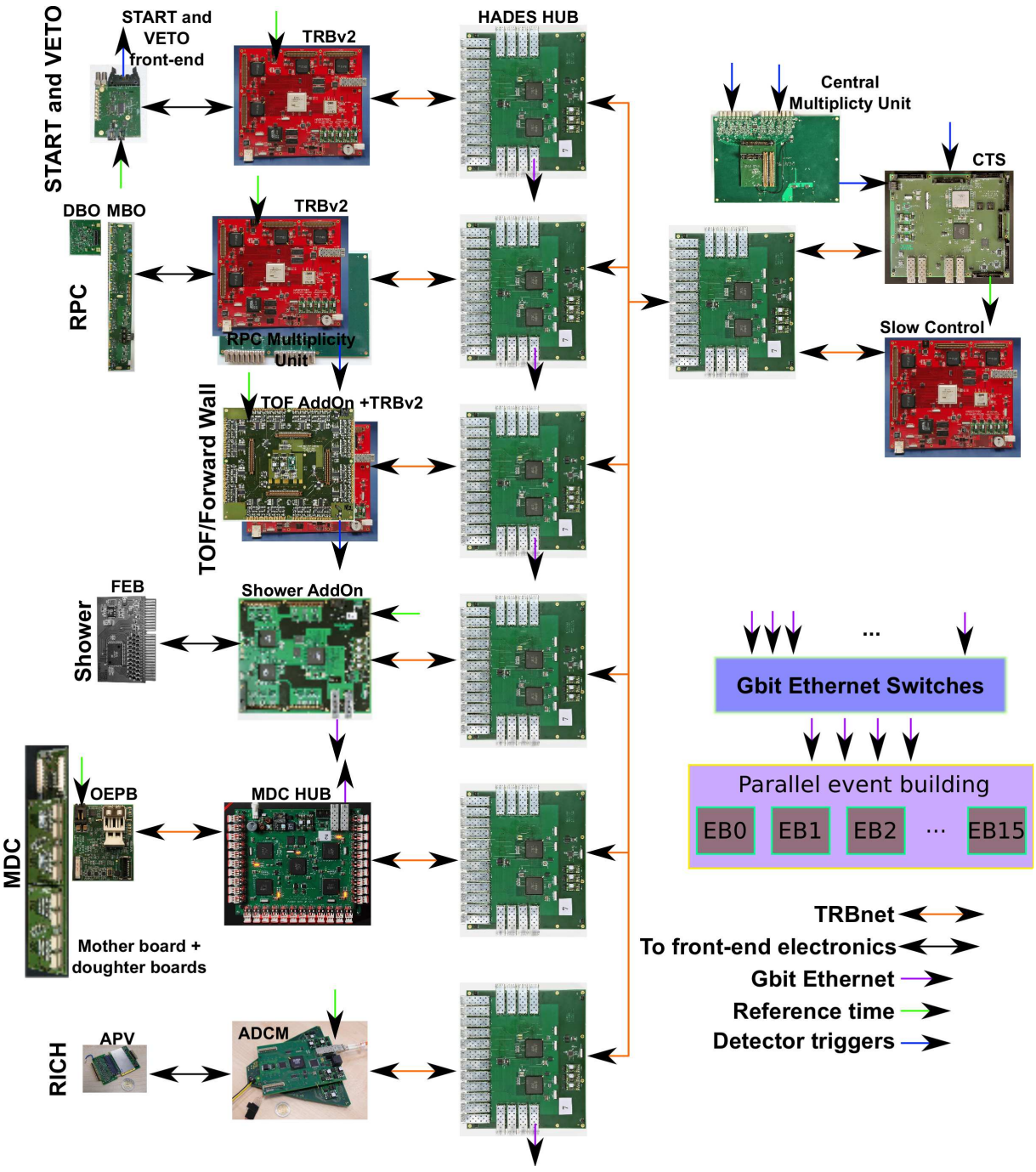

Figure 9.37: Structure of the HADES DAQ system. There are several types of connections for proper system operation. The designed system is able to accept LVL1/readout requests at $\sim 55\ kHz$ for heavy ion beam and up to 100 kHz for light particle reactions.

release signals are sent from all subsystems to the CTS, the CTS transfers a readout request or the next LVL1 trigger (together with the reference time). When the readout

request reaches to the readout electronics the data is transferred directly to the Event Builders (EBs, violet lines). If there is no direct connection to the Gbit Ethernet the data is transferred via TRBnet to the HUBs and then further to the EBs.

Chapter 10

Forward Wall Readout Electronics

As the Forward Wall was newly build detector therefore it was also needed to build electronics for the data acquisition. For this purpose a TRBv1 (Trigger Readout Board version 1) was used.

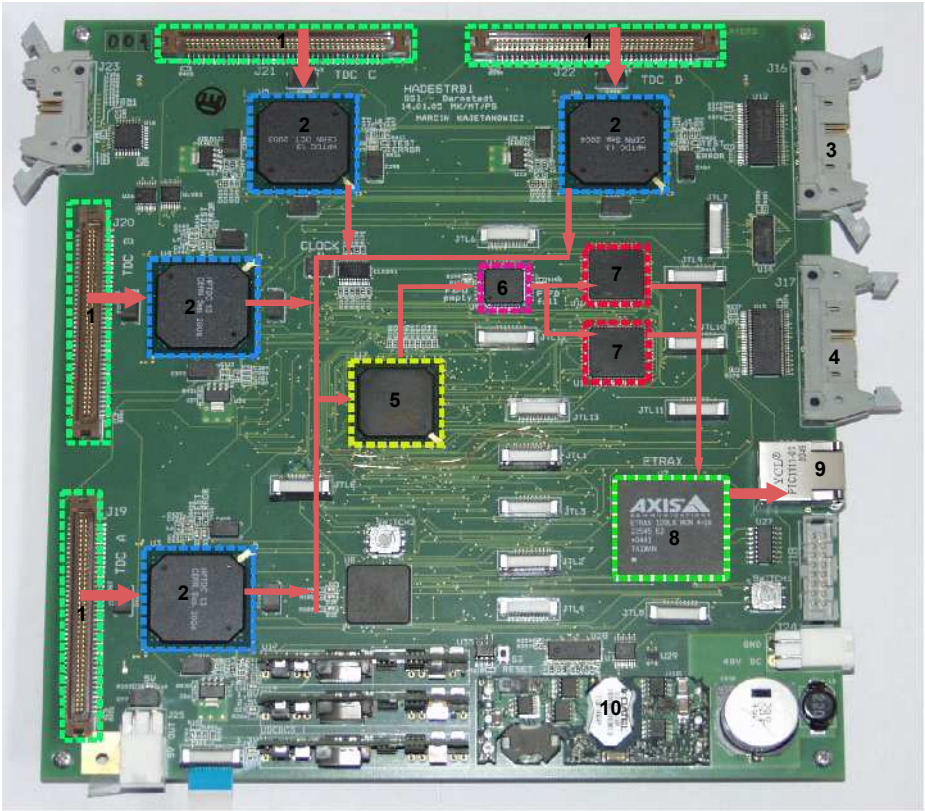

Figure 10.1: The data flow on TRBv1.

The TRBv1 has 4 input connectors (Fig. 10.1,1) (80 pins), which application is to

provide 31 LVDS timing input signals (LVDS - Low-Voltage Differential Signaling) and also special signals(described in the next part of this section). It has four 32 channel High Performance TDCs ASICs [89](HPTDC,fig. 10.1,2) . Each 32nd channel is connected to the externally generated (see 2.3.1) reference time signal. This is necessary to synchronize the data with all other subsystems. The HPTDC ASIC is flexible such it allows to measure the arrival time of the rising or the falling edge (or both), arrange different HPTDC bin widths (from 780ps to 25ps), disable/enable individual channels and prepare set of parameters like (see fig. 10.2):

- trigger latency - fixing the point in the past from which measurement data should be accepted (it is advised by the HPTDC manual not to exceed 25 μs),
- matching window - time period from which data is saved,
- reject latency - time after which the data is discarded to prevent overflows in the internal buffers of the HPTDCs.

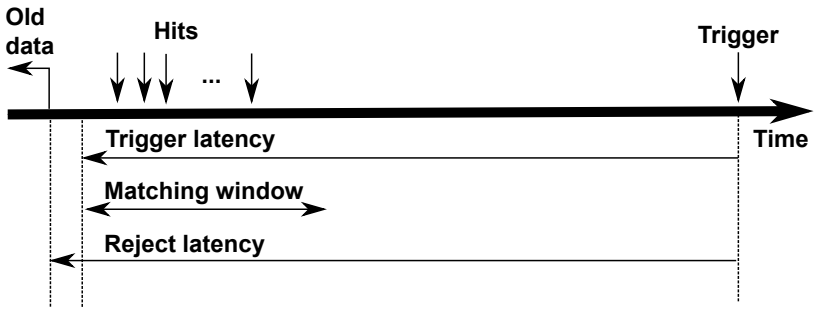

Figure 10.2: Windows settings for HPTDC chip.

All these settings are set via individual JTAG (Joint Test Action Group) interface. First of all this configuration data has to be prepared. This was done in several steps:

- modifying the requested HPTDC parameters in ahead prepared standard setup file with all default settings,
- running the previously written C++ program to create the configuration files in Standard Test and Programming Language (STAPL [90]),

- starting the Jam Player [90] adopted to the on-board Etrax MCM computer chip [91] with Linux running on it. The running Jam Player interpreter drives Etrax port pins, which are corresponding to the standard JTAG lines - TDI,TDO,TCLK,TCK,TMS.

The same interface is used to program the Spartan 2E FPGA(5) (Field Programmable Gate Array). This chip is used as a central entity for the data flow management and it is connected to the LVL1(fig. 10.2,3) and LVL2(4) data buses, FIFO(6), two memories(7), Etrax MCM(8), and HPTDCs.

When the LVL1 trigger and the reference time signal arrives, first the data is selected and saved in the HPTDCs. Next, the FPGA begin the readout by sending the token to the TDC chain. The HPTDCs, one after the other, send the data to the FPGA.

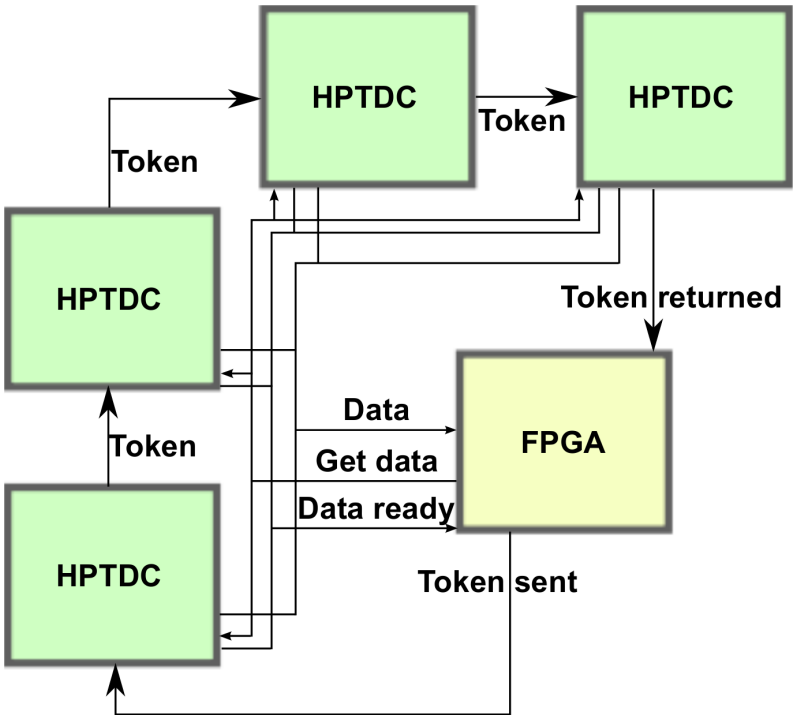

Figure 10.3: Scheme of the HPTDCs readout on TRBv1. The same type of signals are on the same buses - it is allowed, because when the HPTDC has no token the outputs are tristated.

After this stage the FPGA builds an event, which is sent further to the FIFO. The stored events wait for the second level trigger decision arrival to the FPGA. If the decision

is positive they are transported to the memories, if not it is readout from the FIFO without saving them. Afterwards, the FPGA signalizes to the Etrax, that it can start the readout of the collected events. Then, the data is encapsulated by the Etrax with the standard HADES header and fetch via User Datagram Protocol (UDP), over $100MBit$ Ethernet(fig. 10.2,9), to the event builder (EB).

With this scheme it was possible to run with 80kHz accepted LVL1 triggers and 20kHz LVL2 triggers (for fourteen 32 bit data words per event), which corresponds to $1.2MB/s$ of the data transfer.

It is aslo important to mention, that the TRBv1 uses a galvanicly isolated 48V power supply(fig. 10.2,10), which makes much more simple power distribution. This avoids ground loops and gives the possibility to mount the TRBv1 directly on the detector frame.

Bibliography

[1] P. Koch, Z. Pchys. C57 (1993) 283.

[2] S. Leupold, V. Metag, U. Mosel, Hadrons in strongly interacting matter, Int.J.Mod.Phys.E19, 147 (2010).

[3] Y. Nambu and G. Jona-Lasinio, Dynamical Model of Elementary Particles Based on an Analogy with Superconductivity. II, Phys. Rev. 124, 246 (1961).

[4] Nambu And Jona-Lasinio Model, Phys.Lett. B249 (1990), 386-390.

[5] NA60 Collaboration, (R. Arnaldi et al.). May 2006. 5pp., Phys.Rev.Lett.96:162302,2006.

[6] M Kaskulov, E Hernandez and E Oset, Eur. Phys. J. A31, 245 (2007).

[7] P Mühlich and U Mosel, Nucl. Phys. A773, 156 (2006).

[8] T Ishikawa et al, Phys. Lett. B608, 215 (2005).

[9] Dielectron production in Ar+KCl collisions at 1.76A GeV., By HADES Collaboration (G. Agakishiev et al.). Mar 2011. 16pp, Phys. Rev. C 84, 014902 (2011).

[10] M. Abdel-Bary et al. (COSY-TOF Collab.), Phys. Lett. B 647, 351 (2007).

[11] 47, 21 (2011). S. Wheaton and J. Cleymans, Comput. Phys. Commun. 180, 84 (2009). A. I. Titov, B. K¨mpfer, and B. L. Reznik, Phys. Rev. C.

[12] *http://pdg.lbl.gov/.*

[13] M. Gell-Mann, "The Eightfold Way: A Theory of Strong Interaction Symmetry," California Institute of Technology Synchrotron Laboratory Report CTSL-20 (1961), unpublished.; S. Okubo, Note on Unitary Symmetry in Strong Interactions, Prog. Theor. Phys. 27 (1962).

[14] C. Caso et al., Rev of Particle Properties Eur. Phys. J.C 3 (1998) 1.

[15] Particle Data Group, Phys. Rev. D54 (1996) 25.

[16] Y. Nambu and J.Sakurai, Phys. Rev. Lett. 8 (1962) 79.

[17] S. Okubo, Phys. Lett. B5 (1965) 165; I.Iizuka, Prog. Theor. Phys. Suppl 21 (1966) 37; G. Zweig, Cern report no. 8419/th 412 (1996); S. Okubo Phys. Rev. D16 (1977) 2336.

[18] H.J. Lipkin, Phys. Lett. 60B (1976) 371.

[19] Davies D. et al. Phys. Rev. D. 1970. V. 2. P. 506.

[20] Danburg J. et al. Phys. Rev. D. 1970. V. 2. P. 2564.

[21] Abolins M. et al. Phys. Rev. Lett. 1963. V. 11. P. 381.

[22] Ayres D. et al. Phys. Rev. Lett. 1974. V. 32. P. 1463.

[23] Cohen D. et al. Phys. Rev. Lett. 1977. V. 38. P. 269.

[24] Baldi R. et al. Phys. Lett. B. 1977. V. 68. P. 381.

[25] Woodworth P. et al. Phys. Lett. B. 1976. V. 65. P. 89.

[26] Dorofeev V. et al. (Lepton-F Collaboration) Proc. NAN'95 Conf., Moscow, 1995.

[27] Aguilar-Benitez M. et al. (LEBC-EHS Collaboration) Z. Phys. C. 1989. V. 44. P. 531.

[28] Blobel V. et al. Phys. Lett. B. 1975. V. 59. P. 88.

[29] Golovkin S. et al. (SPHINX Collaboration) Proc. NAN'95 Conf., Moscow, 1995.

[30] Aguilar-Benitez M. et al. (LEBC-EHS Collaboration) Z. Phys. C. 1991. V. 50. P. 405.

[31] Cooper A. et al. Nucl. Phys. B. 1978. V. 146. P. 1.

[32] Donald R. et al. Phys. Lett. B. 1976. V. 61. P. 210.

[33] Chen C. et al. Nucl. Phys. B. 1977. V. 130. P. 269.

[34] V. P. Nomokonov, M. G. Sapozhnikov Experimental tests of the Okubo Zweig Iizuka rule in hadron interactions, Phys.Part.Nucl. 34 (2003) 94-123; Fiz.Elem.Chast.Atom.Yadra 34 (2003) 189-238.

[35] Bertin A. et al. (OBELIX Collaboration) Phys. Lett. B. 1996. V. 388. P. 450.

[36] Ellis J. et al. Phys. Lett. B. 1995. V. 353. P. 319.

[37] Ulf-G. Meißner et al., Phys. Lett. B 408, 381 (1997).

[38] M. P. Locher and Yang Lu, Z. Phys. A 351, 83 (1994) ;D. Buzatu and F. M. Lev, Phys. Rev. C 51, R2893 O. Gortchakov et al., Z. Phys. A 353, 447 (1996).

[39] L.G. Landsberg, Phys. Usp. 37, 1043 (1994).

[40] L.G. Landsberg, Phys. Rep. 320, 223 (1999).

[41] A. Sibirtsev, Nucl. Phys. A604, 455 (1996).

[42] M. Hartmann et al., Nucl. Phys. A 755, 459 (2005).

[43] F. Balestra et al., Phys. Rev. Lett. 81, 4572 (1998); F. Balestra et al., Phys. Rev. C 63, 024004 (2001).

[44] V. Blobel et al., Nucl. Phys. B 69, 237 (1974).

[45] M.W. Arenton et al., Phys. Rev. D 25, 2241 (1982).

[46] S.V. Golovkin et al., Z. Phys. A 359, 435 (1997).

[47] Landolt-Bornstein, New Series, Springer, I/12 (1998).

[48] A. Sibirtsev, J. Haidenbauer and U. -G. Meißner, Aspects of ϕ-meson production in proton-proton collisions, Volume 27, Number 3, 263-268, DOI: 10.1140/epja/i2005-10269-9.

[49] "http:www.gsi.de/beschleuniger/Beschleuniger_e.html"

[50] Alvarez, L. et al. Berkeley Proton Linear Accelerator, UCRL-236(rev.); OSTI ID: 4375045, October 13, 1953.

[51] G. Agakichiev et al., "The High-Acceptance Dielectron Spectrometer HADES", Eur.Phys.J. A41:243-277, 2009

[52] F.M. Newcomer, IEEE Trans. Nucl. Sci. 40(4) (1993) 630.

[53] L. Landau , On the Energy Loss of Fast Particles by Ionization, J. Phys. USSR 8 (1944) 201

[54] J. Markert , A. Schmah , C. Müntz , J. Stroth, Energy loss measurement with the HADES drift chambers using the Time-over-Threshold method.

[55] Thomas Bretz. Magnetfeldeigenschaften des Spektrometers HADES. Master thesis, Technische Universität München, 1999.

[56] Cherenkov, Pavel A. (1934). Visible emission of clean liquids by action of γ radiation. Doklady Akademii Nauk SSSR 2: 451. Reprinted in Selected Papers of Soviet Physicists, Usp. Fiz. Nauk 93 (1967) 385.

[57] Böhmer, M.: Das Auslesesystem für den Ringabbildenden Cherenkovdetektor im HADES Spektrometer. Diplomarbeit, Physik-Department der Technischen Universität München, Institut E12, 1999

[58] E.Berdermann et al., Nucl. Phys. (Proc. Suppl.) B 78, 533-539 (1999).

[59] W.Koenig et al., Diamonds as timing detectors for MIPS: The HADES proton-beam monitor and start detectors, INTRUMENTS-METHODS-02, GSI Scientific Report 2008.

[60] R. Santonico, R. Cardarelli, Nucl. Instr. and Meth. A 187 (1981) 377.

[61] A.Blanco: RPC HADES-TOF wall cosmic ray test performance, Nucl. Instr. and Meth. A (2010), doi:10.1016/j.nima.2010.08.068

[62] D. Belve, et. al., Performances of the Front-End Electronics for the HADES RPC TOF wall on a 12C beam.

[63] M. Traxler, Real-Time Dilepton Selection for the HADES Spectrometer Inaugural-Dissertation zur Erlangung des Doktorgrades der Naturwissenschaften der Justus-Liebig-Universität Gießen, 2001.

[64] Petri, M.: Entwicklung eines kombinierten Auslese- und Triggersystems zum Nachweis von Elektron/Positronen-Signaturen in einem elektro-magnetischen Schauerdetektor, PhD. thesis, Universität Gießen, 2001.

[65] Lehnert, J.: Echtzeit-Mustererkennung zum Elektronennachweis mit einem RICH-Detektor in relativistischen Schwerionenkollisionen, PhD thesis, Universität Gießen, 2000.

[66] M. Sanchez, Momentum reconstruction and pion production analysis in the HADES spectrometer at GSI, Ph.D. thesis, University of Santiago de Compostela, 2003.

[67] R. Brun and F. Rademakers, ROOT, an object-oriented data analysis framework, Nucl. Instr. Meth. A389 (1997) 81.

[68] W.Przygoda *http://hades-wiki.gsi.de/cgi-bin/view/Homepages/PAT.*

[69] *http://www-hades.gsi.de/computing/pluto/html/PlutoIndex.html.*

[70] *http://web-docs.gsi.de/ holzmann/hadsimul.html;http://wwwasdoc.web.cern.ch/wwwasdoc/gean*

[71] K. Teilab, The production of η and ω mesons in 3.5 GeV p+p interaction in HADES, Ph.D. thesis.

[72] J. Markert, Untersuchung zum Ansprechverhalten der VieldrahtDriftkammern niedriger Massenbelegung des HADES Experiments, Ph.D. thesis.

[73] H. Wind, Nucl. Instr. Method 115(1974) 431.

[74] W.H. Press, Numerical Recipes, 3rd Edition, Cambridge University Press(2007)

[75] *http://hades-wiki.gsi.de/cgi-bin/view/SimAna/Apr07GlobVertexPos.*

[76] DISTO Coll. (F. Balestra et. al), Phys. Rev. C 63, 024004 (2001).

[77] A. Rustamov *http://hades-wiki.gsi.de/cgi-bin/view/SimAna/Apr07Normalization.*

[78] R. C. Kammerud et al. Large angle proton proton elastic scattering at intermediate momenta. Phys. Rev., D4:1309–1324, 1971.

[79] A. Rustamov. Exclusive η meson reconstruction in a proton-proton collisions at 2.2 gev with the hades spectrometer and high resolution tracking. Disseration. Technische Universitat Darmstadt, 2006. 41, 45, 81.

[80] Irakli Keshelashvili Ph.D. thesis Kaon Pair Production in pp Collisions at the ANKE Spectrometer.

[81] TOF Collaboration: S. Abd El-Samad et al., Phys. Lett. B 522, 16 (2001).

[82] F. Hibou et al., Phys. Rev. Lett. 83, 492 (1999).

[83] A. Baldini et al., in Numerical Data and Functional Relationships in Science and Technology, Total Cross–Sections for Reactions of High Energy Particles, New Series, Group 1, Vol. 12 (Springer–Verlag, Berlin, Heidelberg, 1998).

[84] R. Baldi et al., Phys. Lett. B 68, 381 (1977).

[85] V. Blobel et al., Phys. Lett. B 59, 88 (1975).

[86] *http://www.gsi.de/portrait/fair.html.*

[87] M. Palka et al., The New Data Acquisition System for the HADES Experiment, Nuclear Science Symposium Conference Record, 2008, NSS 08, IEEE, p. 1398-1404.

[88] I. Fröhlich et al., A General Purpose Trigger and Readout Board for HADES and FAIR-Experiments. IEEE Trans.Nucl.Sci. 55 (2008) 59-66.

[89] HPTDC, Jorgen Christiansen, Digital Microelectronics Group, CERN

[90] Altera, *http://www.altera.com/support/devices/tools/jam/tls-jam.html.*

[91] ETRAX, AXIS Communications, Sweden

[92] *http://focus.ti.com/docs/prod/folders/print/tlk2501.html.*

[93] *http://www.analog.com/en/*

[94] R.Trebacz : Investigation of dielectron production in quasi-free p − n scattering at 1.25 GeV with HADES, PhD. thesis, Jagiellonian University, 2011

[95] *http://focus.ti.com/docs/prod/folders/print/cdclvd110.html?CMP=AFC-conv_SF_SEP*

[96] J.Michael PhD thesis in progress, Johann Wolfgang Goethe-University, Frankfurt, 2011

[97] *http://en.wikipedia.org/wiki/Serial_Peripheral_Interface_Bus*

[98] F. Anghinolfi, P. Jarron, F. Krummenacher, E. Usenko and M. C. S. Williams, "NINO: An ultrafast low-power front-end amplifier discriminator for the time-of-flight detector in the ALICE experiment," IEEE Trans. Nucl. Sci. **51**, 1974 (2004).

[99] A. Balanda *et al.*, "Development of a fast pad readout system for the HADES shower detector," Nucl. Instrum. Meth. A **417**, 360 (1998).

[100] *http://www.firecomms.com/products-optolock.html.*

[101] A. Tarantola et al., The Upgrade of the Multiwire Drift Chamber Readout of the HADES Experiment at GSI. Nuclear Science Symposium Conference Record, 2008, NSS 08, IEEE, p. 2146-2149.

[102] M.Raymond *et al.*, "The CMS Tracker APV25 0.25 μm CMOS Readout Chip,", *Proceedings of the 6th workshop on electroics for LHC experiments,* CERN/LHCC/2000-041, 130-134.